Title
Chiral Vortices in Ferroelectric Heterostructures

Author
Hsu, Shang-Lin

Publication Date
2019

Peer reviewed|Thesis/dissertation

Chiral Vortices in Ferroelectric Heterostructures

by

Shang-Lin Hsu

A dissertation submitted in partial satisfaction of the

requirements for the degree of

Doctor of Philosophy

in

Engineering- Materials Science and Engineering

in the

Graduate Division

of the

University of California, Berkeley

Committee in charge:

Professor Ramamoorthy Ramesh, Chair

Professor Andrew Minor

Professor Sayeef Salahuddin

Spring 2019

Chiral Vortices in Ferroelectric Heterostructures

Abstract

Chiral Vortices in Ferroelectric Heterostructures

by

Shang-Lin Hsu

Doctor of Philosophy in Materials Science and Engineering

University of California, Berkeley

Professor Ramamoorthy Ramesh, Chair

Topological structures in condensed matter are fascinating for fundamental research and applications due to their phase transitions with unique properties. Notably, the topological structures in ferroic materials can facilitate the miniaturization of electronic devices and could create future novel functional devices. Ferroelectricity and magnetism are two intriguing properties of ferroic materials. The switchable spontaneous properties of ferroic materials also play important roles in the topological structures. Ferromagnetic topological structures have been studied in-depth decades ago, and today the magnetic skyrmions have potential for racetrack memory in the future. As for the ferroelectrics, although two-dimensional topological structures such as domain walls are well investigated, scientists successfully predicted the three-dimensional topological structure in low-dimensional ferroelectrics a decade ago. This finding attracted significant attention and stimulated demand for more studies. Until recently, the manipulation of charge and lattice degrees of freedom in atomically precise and low-dimensional ferroelectric superlattices can stabilize exotic polar structures. For example, in $PbTiO_3/SrTiO_3$ superlattices, emergent polar toroidal phases such as the vortex phase can be produced; these phases exhibit phase competition and emergent chirality.

This dissertation studies the phase transition and intrinsic properties of polar vortices in artificial ferroelectric heterostructures and understand mechanisms underlying the property. In Chapter 1, the basic knowledge of ferromagnetic and ferroelectric topological structures is introduced and how domain structures are formed. In general, the multi-domains separated by domain walls would arrange the homogeneous polarization distribution in ferroic materials. Tuning the boundary conditions such as the mechanical and electrical boundary conditions, the inhomogeneous polarization distribution can be generated in low-dimensional ferroelectrics.

Recently, the discovery of polar vortices in $PbTiO_3/SrTiO_3$ superlattices as well as their phase coexistence and chirality indicate the challenges of the emergence, phase transition, and property of the inhomogeneous phase. However, the role of interfaces in evolving the vortex phase in these superlattices, the associated electrostatic and elastic boundary conditions they produce, and the chiral domains with different handedness in the ferroelectrics have remained unclear. Therefore, the dissertation investigates a toroidal phase in a $SrTiO_3/PbTiO_3/SrTiO_3$ trilayer along with its phase transition and different chiral properties.

Chapter 2 describes the experimental methods used in this work. The trilayer heterostructure fabrication is achieved with pulsed laser deposition. Transmission electron microscopy and synchrotron X-rays are used as structural characterizations. Piezoresponse force microscopy is used to probe the polar structure. The chirality measurement is achieved with second harmonic generation in circular dichroism. The polarization distribution and mechanism are simulated with phase-field modeling.

Chapters 3 and 4 explains how the toroidal phase, which is arranged in arrays of alternating clockwise and counterclockwise polar vortices, arises from the effects of depolarization fields and tensile strain. The chapter observes how varying the thickness of the confined $PbTiO_3$ layer results in the vortex phase emerging from the ferroelectric phase. Intriguingly, the origin of the vortex state only emerges at the head-to-head domain boundaries in ferroelectric a_1/a_2 twin structures. Further, by varying the total number of confined $PbTiO_3$ layers that are moving from trilayers to superlattices, it is possible to manipulate long-range interactions among multiple confined $PbTiO_3$ layers. This manipulation also has an impact on the stabilization of the vortex state and is key to the important role that elastic energy plays in mediating the formation of these structures. This approach offers a new understanding of how the different energies work together to produce this exciting new state of matter and contribute to the design of novel states and potential memory applications.

Chiral materials possess extraordinary right-or-left-handedness that can be chosen as the active object with different responses for broad applications in science. In ferroic materials, topological defects such as magnetic skyrmions that have chirality can be controlled by the electric field for future spintronic and memory applications. However, chiral domains with different handedness in the ferroelectrics have never been observed. Chapters 5 and 6 discuss how polar vortices as three-dimensional (3D) polarization textures exhibit collective behaviors of chiral domains in the confined ferroelectrics. The polar vortices are identified to possess antiparallel axial polarizations that perform microscopic helical rotation of electric polarization by probing the atomic displacement using atomic-resolution scanning transmission electron microscopy (STEM). Mirror symmetries are used to verify the handedness. As a result, left-and-right-handed chiral vortices and the achiral region are found as the gradient chirality. The competition between left-and-right-handed vortices arises at the achiral region, which forms the possible precursor of the skyrmions-type structure. Strikingly, this thesis uses circular dichroism measurement with second harmonic generation to confirm the left-and-right-handedness of helicity and achiral regions macroscopically. These multi-states that are under handedness manipulation by the electric field can open an energy-efficient route and have significant potential for information processing.

Dedication

To my beloved and inspiring Hsu family
For their love and support

Table of Content

List of figures

Acknowledgments

I want to express my gratitude to all the people who helped me to make my research successful. First and foremost, I express my sincere thanks to my esteemed advisor, Prof. Ramamoorthy Ramesh, for giving me the chance to conduct cutting-edge research at Berkeley. Sir Isaac Newton once said, "If I have seen further, it is by standing upon the shoulders of giants." I am highly indebted for Ramesh's guidance, suggestions, and encouragement, which helped me to see further and resolve the problems of the research. Also, I would like to thank my qualifying committee members, including Prof. Andrew Minor, Prof. Lane Martin, Prof. Alex Zettl, and Prof. Mark Asta for their helpful advice and comments on this dissertation.

I express my deepest gratitude to my mentor, Dr. Christopher T. Nelson, for his help in teaching me basic to advanced skills of transmission electron microscopy. I wish to thank Dr. Julia Munday for her insightful suggestions on various projects. Also, I would like to thank Margaret McCarter for providing high-quality thin films for me to study. I had a great time engaging on multiple projects at the National Center for Electron Microscopy at Lawrence Berkeley National Laboratory. I would thank the following people for their help in the experiments: Director Prof. Andrew Minor, Dr. Colin Ophus, Dr. Jim Ciston, Dr. Peter Ercius, Dr. Karen Bustillo, Prof. Mary Scott, Chengyu Song, John Turner, Dr. Roberto dos Reis, Dr, Rohan Dhall, and Marissa Libbee.

I want to thank the current and former lab-mates in Berkeley for their support and help on various projects: Dr. Ajay Yadav, Dr. Yen-Lin Huang, Dr. Yun-Long Tang, Dr. Bhagwati Prasad, Xiaoxi Huang, Dr. Arnoud Everhardt, Dr. Vishal Thakare, Dr. Sujit Das, Dr.Weichuan Huang, Prof. Jian Liu, Dr. Di Yi, Dr. Claudy Serrao, Prof. Zhiqi Liu, Dr. Nikita Gaur, Dr. Jeremy Turcaud, Suraj Cheema, Dr. Lei Zhang, Dr. Anirban Ghosh, Jieun Kim, Dr. Shishir Pandya, Dr. Joshua Agar, Dr. Ruijuan Xu, Ran Gao, Sahar Saremi, and Liv Dedon. Also, I would like to thank my collaborators for their contributions to this dissertation: Cheng Dai, Dr. Zijian Hong, and Prof. Long-Qing Chen from Penn State; Prof. Javier Junquera from University of Cantabria; and Ms. Molly May and Prof. Markus Raschke from the University of Colorado.

Finally, I would like to acknowledge my beloved parents, my brother and sister, my wife, and my daughter for their full support and company.

Chapter 1: Introduction

In this chapter, the necessary knowledge and previous work on the superlattices are presented. Novel topologies with non-trivial properties have been studied due to their potential applications to electronic devices for which ferroic materials are the best candidate to investigate. The targeted structure in this work is the ferroelectric topology having an inhomogeneous, vortex-like polarization distribution, which was first predicted a decade ago. This chapter will explain the mechanism by which the inhomogeneous polarization distribution forms from the traditional homogeneous polarization in ferroelectric materials. Later, our previous study on the first direct observation of the polar vortices in ferroelectric superlattices is presented. Most importantly, the polar vortices coexist with traditional ferroelectric domains in the superlattices and possess chirality.

1.1 Topological structures in ferroic materials

The complex interplay of spin, orbital, charge, and lattice degrees of freedom and related interactions in complex oxide heterostructures give rise to exciting emergent phenomena and exotic physical properties [29–31] such as multiferroicity [32–36], colossal magnetoresistance [37,38], and superconductivity [39]. Among the fascinating topics in condensed matter, topological structures or defects attract significant attention due to their phase transitions with unique properties. This is especially the case in ferroic systems, due to their functionalities. A topological structure is a particle-like structure that refers to a particular field configuration [40] which can be moved by a perturbation without transforming to other arrangements with different topological numbers. In 1962, Tony Skyrme invented the concept of skyrmions, which are a type of critical topological defect [41], while magnetic bubble memories were the popular technology and research topic [42] of the 1970s. As a result of technological development, magnetic skyrmions can now be created, annihilated, and manipulated by an electric field and potentially be used in racetrack memory applications [43].

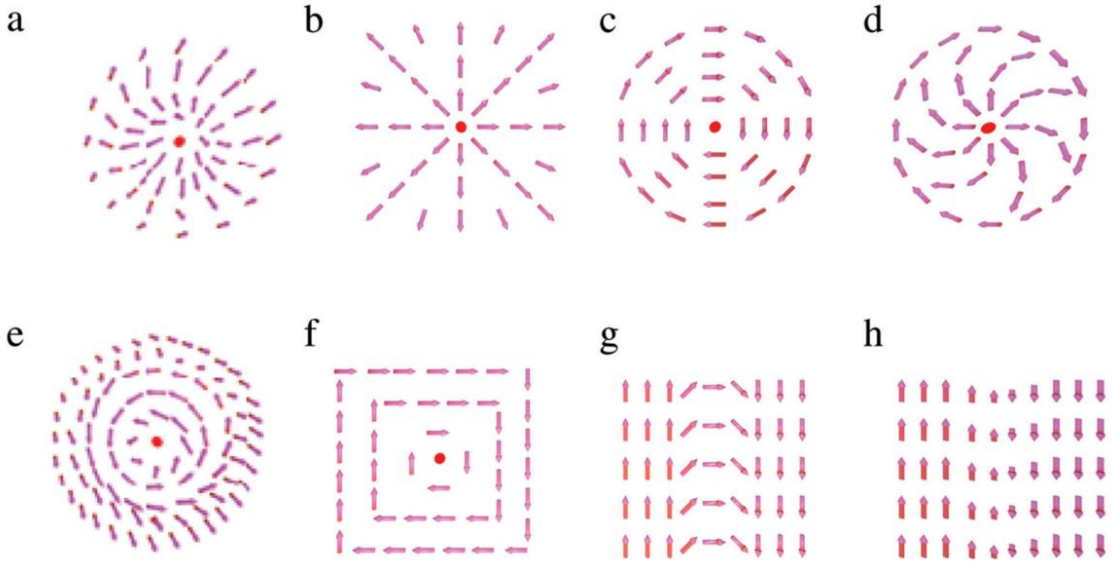

Figure 1.1 Schematic graph of topological structures in different orderings. (a) Radial skyrmion, (b)(c)(d) different configurations of vortex structure, (e) chiral skyrmion, (f) four-quadrant closure structure, (g) domain wall with a freely rotating order parameter, (h) and domain wall with a steadily decreasing in magnitude vector. Adapted from [1].

In ferroic materials, the characteristics and controllability of these spontaneous properties (*e.g.*, ferroelectricity and magnetism) and switchable physical structures (*e.g.*, domains or skyrmions) with their phase transitions are important research topics. Researching these topics can create exciting opportunities to design and facilitate the miniaturization of future electronic devices such as nano non-volatile memories [34]. Ferromagnetism and ferroelectricity are two crucial properties with useful technological applications such as data storage, motors (ferromagnetic), sensors, information technology, and actuators (ferroelectric). Additionally, the properties associated with

the phases are strongly temperature dependent. In the 1940s, Kittel proposed a scaling law of ferromagnetic domains to demonstrate how flux-closure structures without a net magnetization form are due to the demagnetization fields at the surfaces [44,45], which has been further confirmed by several experimental observations [46–49]. The stable states can be characterized by regions with a single polarization orientation (domains), which are separated by domain walls as the two-dimensional (2D) topological defects that are depicted in Figure 1.1 (f); the different types of domain walls are depicted in Figure 1.1 (g)-(h). The domain size will become small if anisotropy energy is high. Other than domain walls, geometry plays a vital role in topological defects with different configurations. The stable domain configurations can be varied in arrangements with different boundary conditions such as the exchange interactions and crystallographic anisotropy – for example, Figure 1.1 (d)-(e) [50,51] depicts the vortex structure [26,52–54] forming with the low anisotropy energy. Experiments have also demonstrated that the vortex structures can be moved [55–57] and switched [58–62] using an electric or magnetic field to explore their dynamics.

As depicted in Figure 1.1 (a)(e), the 2D configurations of magnetic skyrmions indicate the continuous rotation of magnetization and have been observed [27,63]. When viewed from the 3D configurations with a line cut as depicted in Figure 1.2, one type of skyrmion is composed of a Bloch-type domain wall where the spins rotate perpendicular to radial directions. The other type is composed of a Neel-type domain wall where the spins rotate along the radial direction. The 3D-Bloch type skyrmion also has a vortex-like structure and is also called a vortex skyrmion. There are several mechanisms to excite the formation of skyrmion structures, including the Dzyaloshinskii-Moriya (D-M) interaction, long-range dipole interactions, frustrated exchange interactions, and four-spin exchange interactions [64]. One of the crucial mechanisms is the D-M interaction, which favors canting of the neighboring spins and stabilizes the constant winding of the magnetization without aligning to an ordered structure [65,66]. Further, the applications of skyrmions to memory devices and the electric control of skyrmions have been studied [64,67]. Hence, knowledge of the inherent structure-property relationships and the formation mechanisms of topological defects associated with the defects' properties can be applied to device applications.

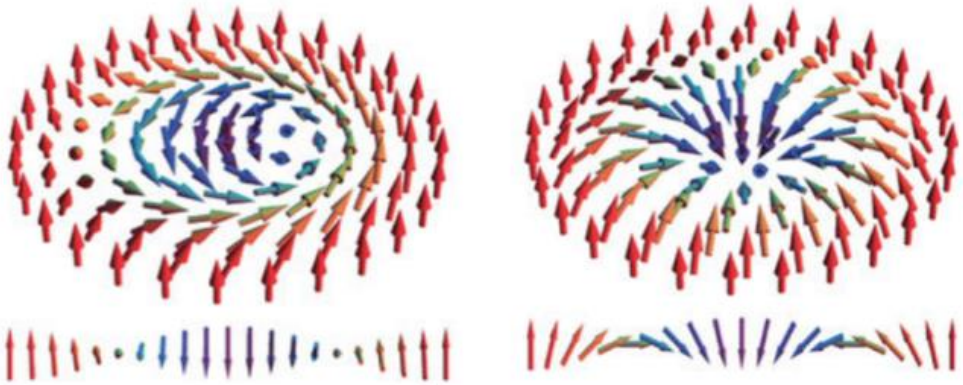

Figure 1.2 Schematic graph of different types of magnetic skyrmions. Adapted from [2].

Characterizations of the domain walls of topological defects in ferroelectric materials have been studied in-depth. The domain wall configurations and properties of the ferroelectric domain walls indicate unusual phenomena, such as the conduction of ferroelectric domain walls in multiferroic $BiFeO_3$ that is depicted in Figure 1.3. Due to the change of the crystal structure, charged domain walls form at certain domain boundaries and are found to have different transport properties from the domain [68,69]. These findings have the potential for functionalities such as non-volatile memory and electroresistive memory devices [70].

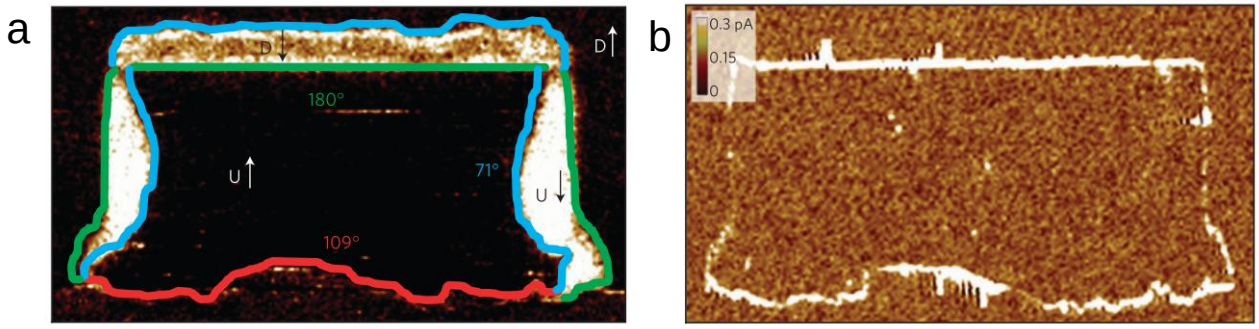

Figure 1.3 Three types of domain walls in rhombohedral $BiFeO_3$. Imaged using in-plane piezoelectric force microscopy (PFM). (a) Written domain pattern in mono-domain $BiFeO_3$ (110) thin film. (b) Conductive atomic force microscope imaging showing conduction at 109° and 180° domain walls. Adapted from [3].

1.2 Ferroelectric Domain Structures

1.2.1 Homogeneous Distribution of Polarization

Ferroelectric materials have spontaneous electric dipole polarization – polarized states without an applied electric field – and can be switched reversibly with an electric field. These features can be revealed in the hysteresis loop, which demonstrates how the polarization changes with an applied electric field. Ferroelectric materials above the Curie temperature have a high symmetry crystal structure and are paraelectric. Ferroelectric materials below the Curie temperature undergo a phase transition to a lower symmetry state, which results in the formation of spontaneous polarization. For example, $PbTiO_3$ (PTO) has the perovskite ABO_3 crystal structure that is depicted in Figure 1.4. The structure indicates that A-site ions (Pb) are located on the corners of the cubic unit cell and the B-site ion (Ti) is situated in the center of the unit cell. The B-site ion combines with the oxygen anions in the center of each cubic face to form the oxygen octahedra.

Below the Curie temperature of 490°C, the crystal structure of PTO changes from cubic to tetragonal and has ferroelectric distortion in a unit cell where the oxygen and titanium atoms displace relative to one another in the out-of-plane direction. The displacements of the titanium ions can be used to determine the polarization. Above the Curie temperature, the paraelectric state has cubic symmetry with no polarization. The origin of the ferroelectricity is the lowering of the geometrical symmetry, which leads to orbital mixing of a non-degenerate ground state with a low-lying excited state. For example, in $BaTiO_3$, the noncentrosymmetric distortion is the off-centering of the B-site cation that is stabilized through d^0 mixing with oxygen *p* atomic orbitals. In $BiFeO_3$, the stereochemical activity of Bi^{3+} lone-pair electrons forms localized lobe-like electrostatic repulsion, breaking the inversion symmetry in $BiFeO_3$. This is known as the second-order Jahn-Teller effect [71–73].

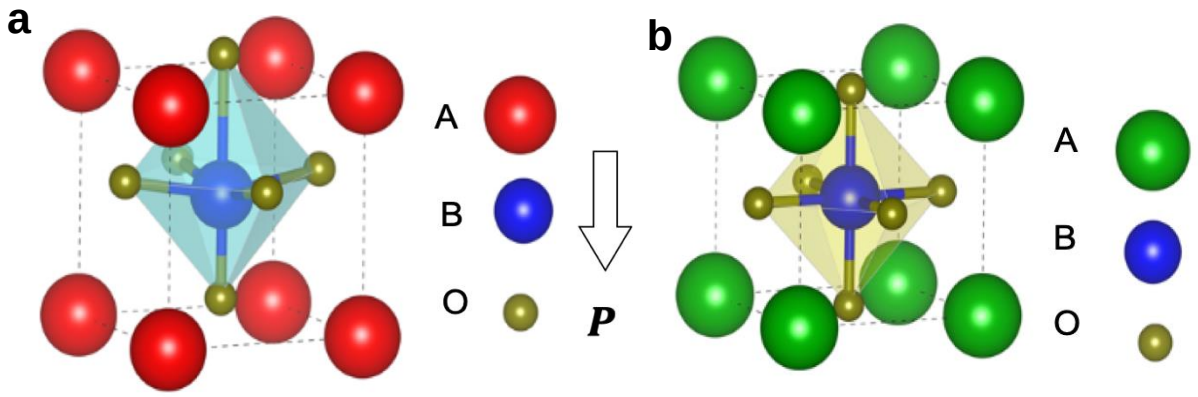

Figure 1.4 Perovskite ABO_3 structure demonstrates the (a) ferroelectric distortions below the Curie temperature and (b) the paraelectric phase above the Curie temperature.

Homogeneous distribution of polar structure happens below the Curie temperature. Macroscopic domains are formed, each with a single polarization direction, and the different domains are separated by domain walls. Sometimes, the domain walls can have very different properties from the domains: conducting domain walls can separate insulating domains, for example [3].

In general, there are two types of domain walls that separate the two polarized domains in tetragonal ferroelectric materials. These types can be differentiated by angle, as in Figure 1.5 (a) and (b). One type is the ferroelectric 180° domain wall, which is formed due to the purely electrical boundary conditions. The other type is the ferroelastic 90° domain wall, which is formed due to the mechanical boundary conditions. In a real material system, both domain walls separate the multi-domains and are easily found. Inside the domain walls, the polarization configuration is not uniform in one direction, and the domain walls therefore have higher gradient energy than the zero in the domains. This gradient energy is affected by the change of the dipole orientation and the magnitude of the polarization distribution. Therefore, a ferroelectric system can have several aspects that stabilize the polarization distribution, which is associated with the balance of energies including the electrostatic energy, elastic energy, and gradient energy.

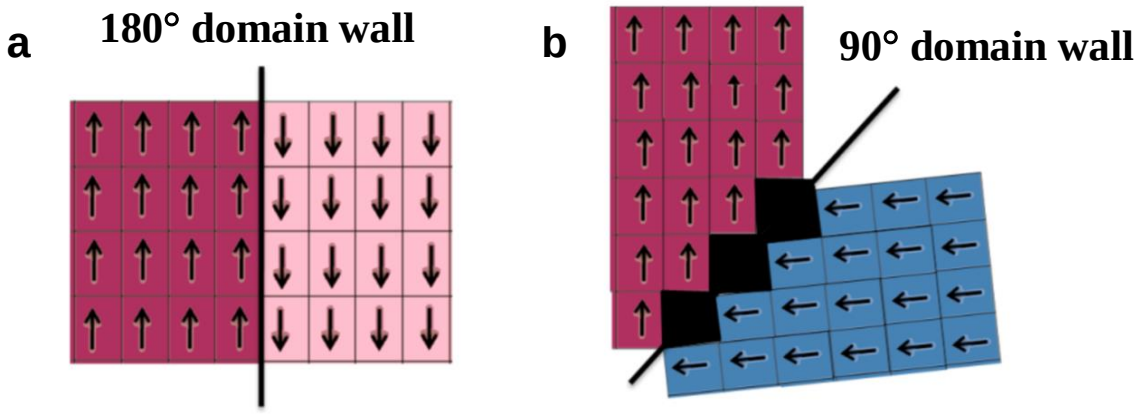

Figure 1.5 Schematic graph of traditional tetragonal ferroelectric (a) 180° domain wall and (b) 90° domain wall. Adapted from [4]

Domain characterization in ferroelectrics plays a vital role in studying the properties of ferroelectrics. The boundary conditions are the main factors to influence the ferroelectric domain structures. When a bulk material is reduced to a thin film, these boundary conditions become more sensitive due to the finite thickness and the substrate effect. When the temperature is lowered from a high temperature to below the Curie temperature, the spontaneous polarization of the ferroelectric film triggers the bound charge to accumulate on both sides of the thin film surface, as depicted in Figure 1.6 (a). If these bound charges cannot be screened out, they lead to the depolarization field E_{dep}, which works to reduce the spontaneous polarization. Therefore, many conditions can prevent the onset of the depolarization field. Figure 1.6 (b) indicates how the polarization configuration of the film may self-organize into 180° domains with an antiparallel polarization arrangement or a flux-closure domain arrangement (with 90° domain walls) that makes the charge neutral. Other ways to avoid the depolarization field include using metallic electrodes on both sides of the thin film, atmospheric adsorbents, or mobile charges inside the film with semiconductor property, as depicted in Figure 1.6 (c).

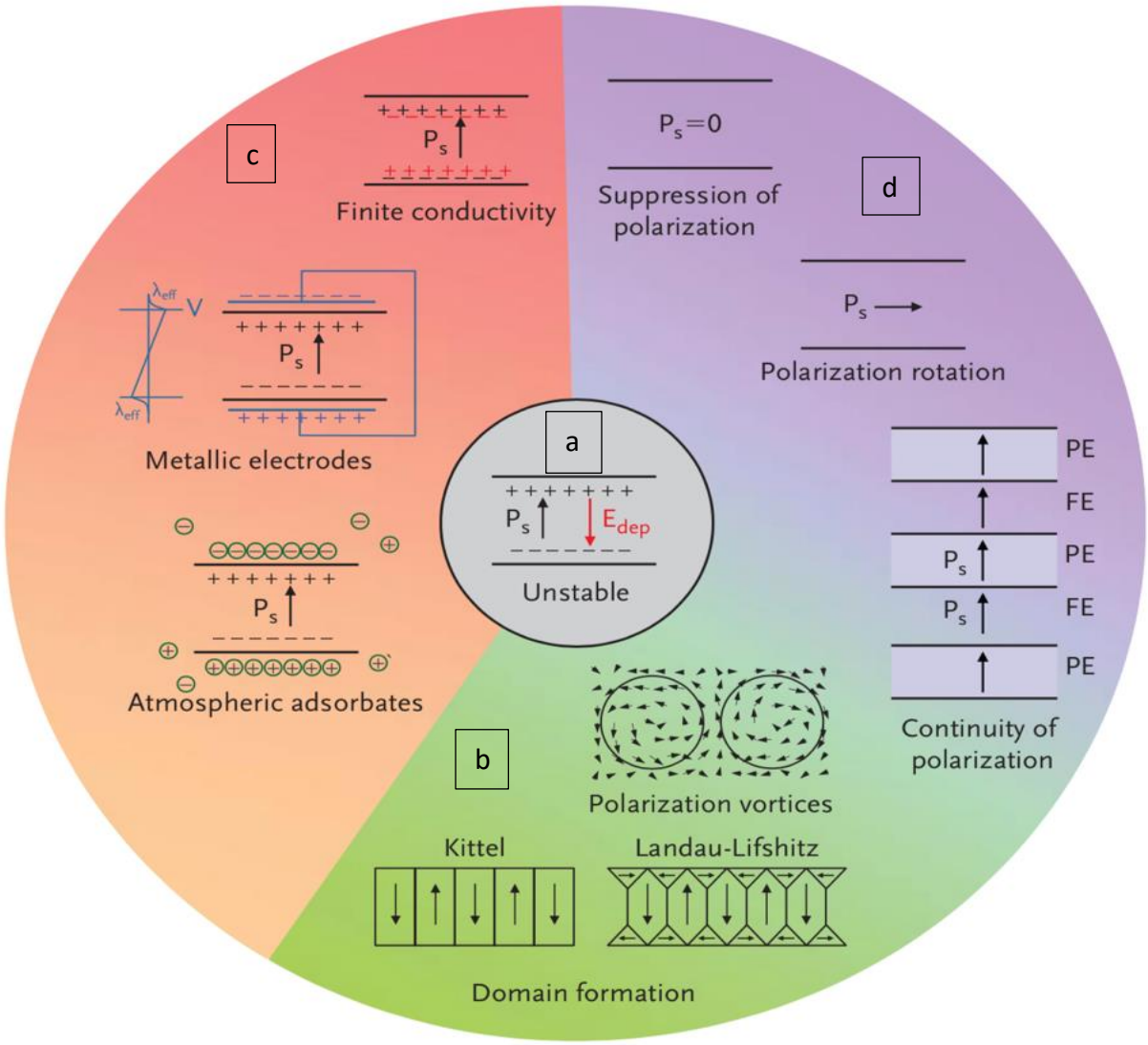

Figure 1.6 The depolarization effect on the ferroelectric thin film to influence the polarization configurations. Figure adapted from [5].

Figure 1.6 (d) illustrates how once mechanical strain is introduced into the ferroelectric system to stabilize with the depolarization field, the domain configuration can suppress the spontaneous polarization to zero. Also, strain conditions can tune the polarization directions to point fully in-plane, which is known as polarization rotation. Other situations can polarize the paraelectric layers to achieve continuity of polarization in the nanoscale ferroelectric or paraelectric superlattices or to stabilize the polarization distribution with a continuous rotation of vortex-like polarization that generates toroidal order. Hence, to overcome the depolarization effect, polarization rotation can change the polarization direction, which gives rise to the possible stability of the vortex-like state in ferroelectric materials. This is the essential concept of this research.

The system tends to minimize the elastic energy by developing 90° domain walls in tetragonal ferroelectrics, which is similar in concept to the ferroelectric 180° domain wall. Here, strain engineering provides a playground for scientists who use the clamping of the substrate on epitaxial ferroelectrics to tune the domain configurations and their properties. In general, ultrathin films tend to maintain the strain condition, but thick films tend to relax to form misfit dislocations.

Additionally, thin films with large epitaxial compressive strains from the [001] direction of substrate favor out-of-plane polarization distribution of ferroelectric c-domains. If there are large tensile strains, the system favors the in-plane polarization distribution of a-domains. Figure 1.7 indicates how several perovskite substrates with a broad range of in-plane lattice constants can be used to introduce tensile or compressive strain to a film. For example, in-plane ferroelectricity was found in $SrTiO_3$ at room temperature, with +1% tensile strain introduced by the $DyScO_3$ substrate [74], although $SrTiO_3$ is initially paraelectric in bulk at room temperature. Using single-crystal $DyScO_3$ and $GdScO_3$ substrates can tremendously enhance the ferroelectricity in epitaxial $BaTiO_3$ thin films [75]. Thus, the strain from the substrate strongly influences the ferroelectric thin film and its domain configurations and properties. In this research, the mechanical boundary condition is crucial for tuning the polarization distribution of the ferroelectric topological structure.

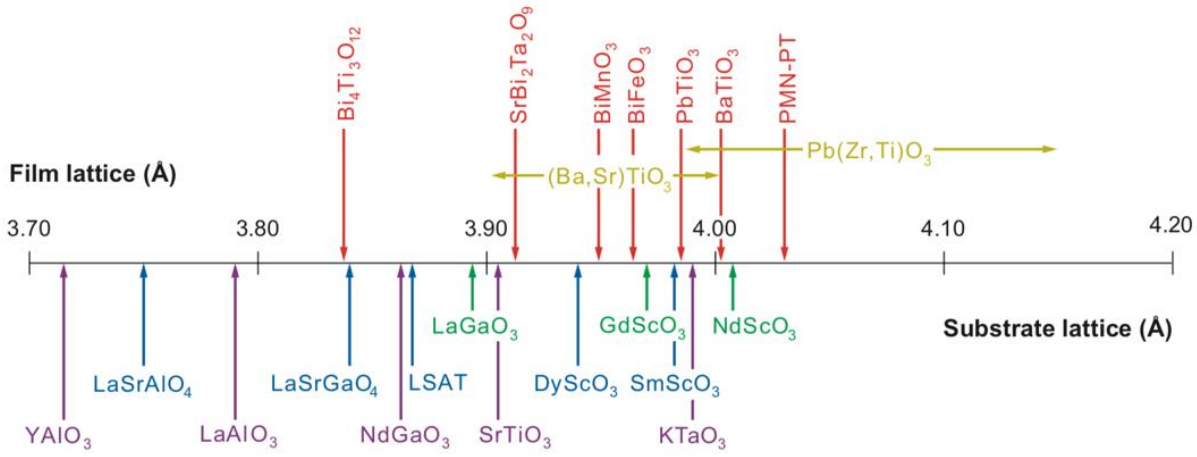

Figure 1.7 Lattice constants of the materials' pseudo-cubic or pseudo-tetragonal a-axis as depicted on the top, and perovskite-related commercial substrates on the bottom for strain engineering. Adapted from [6].

1.2.2 Inhomogeneous Distribution of Polarization

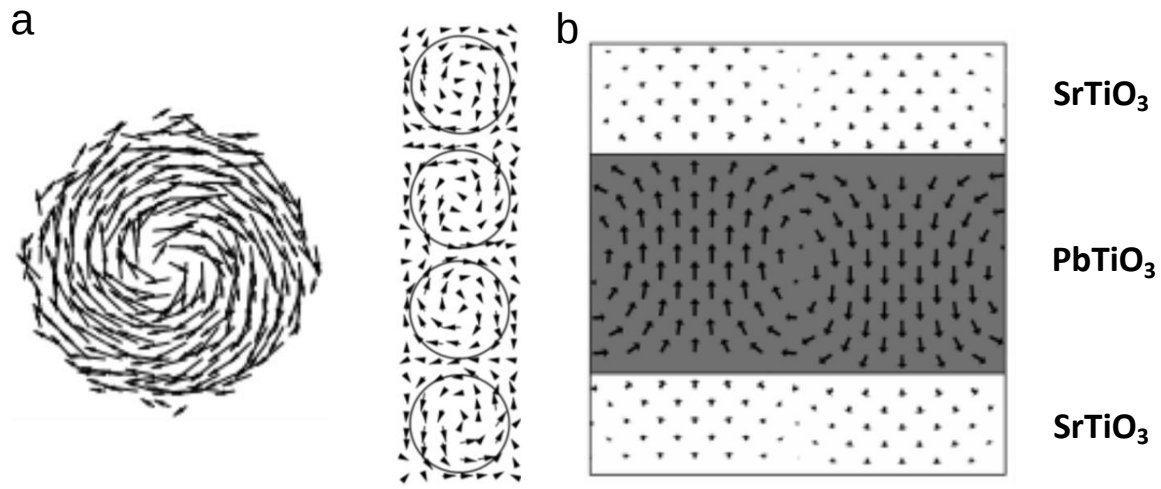

Figure 1.8 Simulated inhomogeneous distribution of polarization vector fields in (a) free-standing ferroelectric nanodisks and nanorods (adapted from [7]) and (b) in $PbTiO_3/SrTiO_3$ superlattices (adapted from [8]) from *ab initio* simulations.

Ferroelectric materials are cousins of ferromagnetic materials and therefore usually form similar domain configurations with uniform polarization distribution, depending on the electrical and mechanical boundary conditions. In 2004, first-principles calculations predicted an inhomogeneous ferroelectric vortex structure in the $Pb(Zr_{0.5}Ti_{0.5})O_3$ ferroelectric nanodisks and nanorods [7] in Figure 1.8 (a). This structure is different from the traditional uniform ferroelectric domain. The continuous rotating distribution of the polarization vortex structure demonstrates that the free-standing nanodisk has unique boundary conditions compared to typical ferroelectric bulk materials. Due to the low dimensions of the nanodisks, the depolarization field is strong enough to suppress the spontaneous polarization at the interface, which rotates the polarization vector parallel to the surface and causes the rotating distribution inside the nanodisks. The new order parameter from the simulation that is called toroid moment *G* can be used to describe the inhomogeneous polarization distribution. Toroid moment *G* would be zero above the transition temperature, and the transition temperature would be marked by the spontaneous formation of a non-zero *G* which is defined in equation 1-1:

$$G = \frac{1}{2N}\sum_i R_i \times p_i \tag{1-1}$$

Where "*N*" is the number of cells, "R_i" is the position vector of the i^{th} unit cell, and "p_i" is the local dipole of cell *i* that is located at R_i. These predictions opened the door to more studies on the inhomogeneous polarization rotation of vortex structures in a low-dimensional ferroelectric

system [76,77]. For example, the coupling of the depolarization field at the $PbTiO_3/SrTiO_3$ interface and the $SrTiO_3$ substrate effect can generate the inhomogeneous distribution in the $PbTiO_3/SrTiO_3$ superlattices depicted in Figure 1.8 (b) [78]. Additionally, an electric field can control the switching of the vortex structure [79,80]. The ferroelectric skyrmion-like structures are also predicted to be stabilized in the form of the nanocomposite of $BaTiO_3$ that is embedded in $SrTiO_3$ [81].

On the experimental side, although $PbTiO_3/SrTiO_3$ superlattices were demonstrated as far back as 1999 [82], the polarization distribution was hard to probe in the low-dimensional system and superlattices. Later, there was a glimpse of the vortex-like structure. The spontaneous vortex-like nanodomains were found at the interface between a $BiFeO_3$ film and $TbScO_3$ substrate [83]. Additionally, the depolarization field can give rise to the formation of inhomogeneous polarization and the possibility of polarization rotation. Both phenomena were found in Pb(Zr, Ti)O_3 [84] and the $PbTiO_3/SrTiO_3$ structure [8]. Therefore, the $PbTiO_3/SrTiO_3$ superlattices system seemed likely to form the inhomogeneous polarization distribution by combing the two different materials to stabilize the novel phenomenon. The size effect was found to play an important role in influencing polarization distribution dramatically in the ultra-thin film instead of the bulk form.

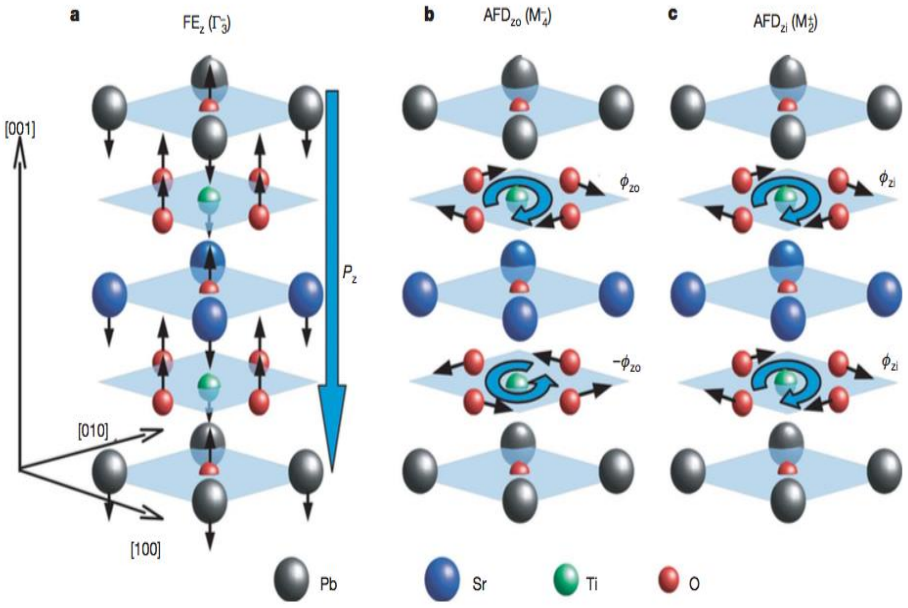

Figure 1.9 Improper ferroelectricity in ultra-thin layers of $(PbTiO_3)_n/(SrTiO_3)_n$ superlattices(n =1) from *ab initio* simulations. Adapted from [9]

The functional properties of PTO/STO superlattices can be tuned as a function of periodicity, especially with the PTO volume fraction as the crucial factor [85]. These functional properties are also found to be tremendously influenced by the interface effects [86]. When the PTO volume ratio of the superlattices is continuously decreased, the polarization drops to the paraelectric limit. Density functional theory calculations predict unusual ferroelectric behavior for $(PTO)_n/(STO)_n$

superlattices that have ultra-thin layers of PTO and STO such as n = 1, as depicted in Figure 1.9. One example is the general ferroelectric distortion that indicates out-of-plane polarization in the left image, but the other two states (out-of-phase and in-phase rotations in the middle and right side of the figure, respectively) demonstrate the emergence of improper ferroelectricity that uses structural distortion as the primary ordering parameter. The main reason for this improper ferroelectricity is the oxygen octahedral rotations at the interfaces of the ground state, anti-ferrodistortive structure of the STO layer.

However, when PTO/STO superlattices have thick PTO layers such as 36 nm on the $GdScO_3$ substrate depicted in Figure 1.10, the polarization distribution of the PTO forms a classical c/a flux-closure type of domain structure [10] with 180° and 90° domain walls. This indicates that the large scale of ferroelectric superlattices will form the homogeneous polarization distribution with c/a flux closure domains, which are usually observed in the bulk-like ferroelectrics [87]. Hence, it is possible to explore the interplay of the size effect between the large and small scale of PTO/STO superlattices to search for inhomogeneous polarization distributions.

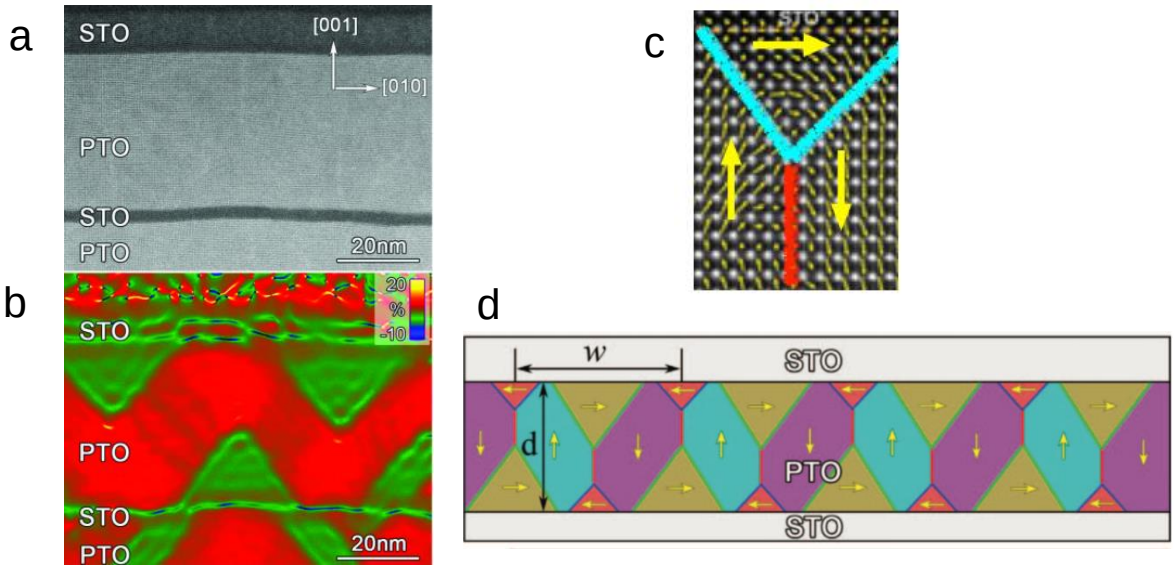

Figure 1.10 Flux-closure polarization distribution in the large scale of $PbTiO_3/SrTiO_3$ superlattices. (a) HR-STEM imaging (b) GPA analysis of the STEM data indicating out-of-plane strain (red) in the c-domains and in-plane strain (green) in the a-domains. (c) Atomic displacement mapping indicating two types of domain walls and (d) schematics of polarization distribution. Adapted from [10].

Between the ultra-thin and large periodicity of PTO/STO superlattices, an exciting discovery in the intermediate scale of $(PTO)_n/(STO)_n$ (n = 10-16) superlattices on the $DyScO_3$ (DSO) substrate took the form of the first observation of inhomogeneous polarization distribution of nanoscale vortex arrays. This novel state was probed by high-resolution scanning transmission electron microscopy (HR-STEM) imaging with atomic displacement mapping in the cross-

sectional view: see Figure 1.11 (a). The non-uniform polarization distribution exhibits a long-range array of continuous rotation of clockwise (CW) and counterclockwise (CCW) vortex pairs, only in the PTO layer with lateral periodicity in a spacing of ~10 nm. Hence, the lattice distortion represents the noncentrosymmetry of the PTO layer, resulting in the arrays of polar vortices.

In the combination of HR-STEM, DF-TEM, and phase-field modeling studies depicted in Figure 1.11 (b), the integrated data demonstrates the 3D polarization concept of vortex arrays. The cross-sectional TEM in the bottom left indicates the continuous rotations of polar vortices in the PTO layers, and the image on the top view of the superlattices observed by DF-TEM indicates that a striped pattern forms with a spacing of ~10 nm. The spacing of stripes matches the size and the direction of the vortex array observed in the cross-sectional TEM. The calculations of phase-field modeling on the right match with the experimental observation that 3D polarization mapping of tube-like CW and CCW vortices on the DSO substrate and the opposite signs of vorticity of the CW and CCW vortices.

The phase-field modeling also indicates the formation of a vortex structure through competition between the Landau, elastic, electrostatic, and gradient energies. The Landau energy represents the primary ferroelectric double-well energy. The elastic energy refers to PTO layers under tensile strain from the DSO substrate and prefers the mixed domain structures of out-of-plane c-domains and in-plane a-domains. Furthermore, the electrostatic energy contributes at the PTO/STO interface when there is a polar discontinuity that gives rise to bound charges, which results in a non-zero gradient of polarization. Finally, the gradient energy represents the rotation of the polarization, including the changes of the magnitude and direction of the polarization. The non-uniform polarization distribution can be tuned by the boundary conditions of the superlattices and compensated for the gradient energy; the distribution can be identified by the first experimental observation with predicted simulations as a novel topological state.

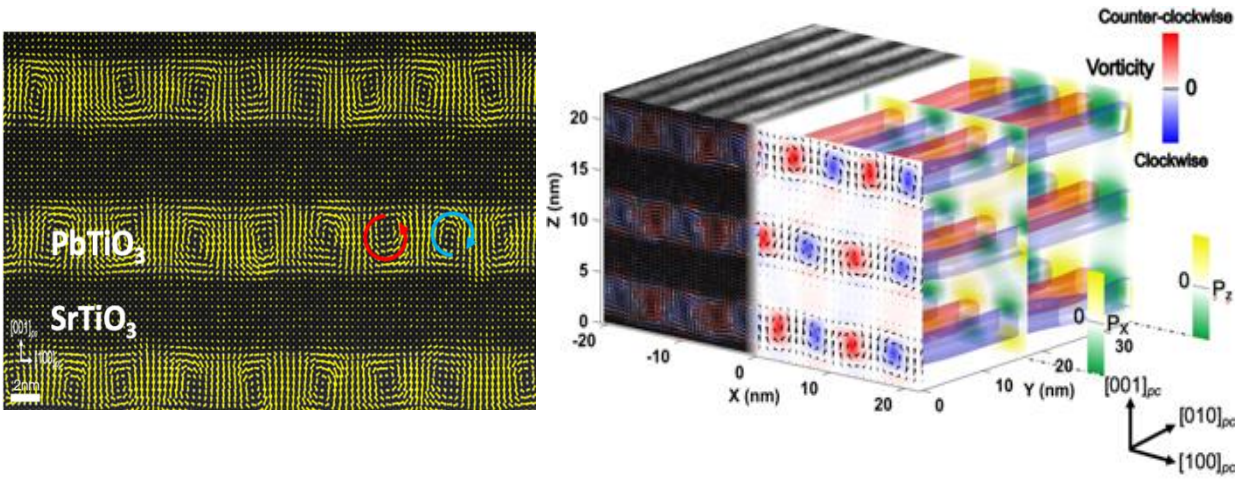

Figure 1.11 Polar vortices in the intermediate scale (n ~12-to-20-unit cells) of $(PTO)_n/(STO)_n$ superlattices. (a) Atomic displacement mapping extracted from HR-STEM imaging. (b) Integrated experimental and theoretical data in three dimensions, including a cross-sectional view of polarization vector P ordered into CW (blue) and CCW (red) rotation directions. On the left,

planar-view dark field TEM imaging indicates tube-like vortices, and phase-field modeling predicts tube-like CW/CCW vortices, depicted on the right. Adapted from [11].

1.3 Phase coexistence and properties of polar vortices

1.3.1 Phase coexistence of traditional ferroelectric domains and ferroelectric vortices

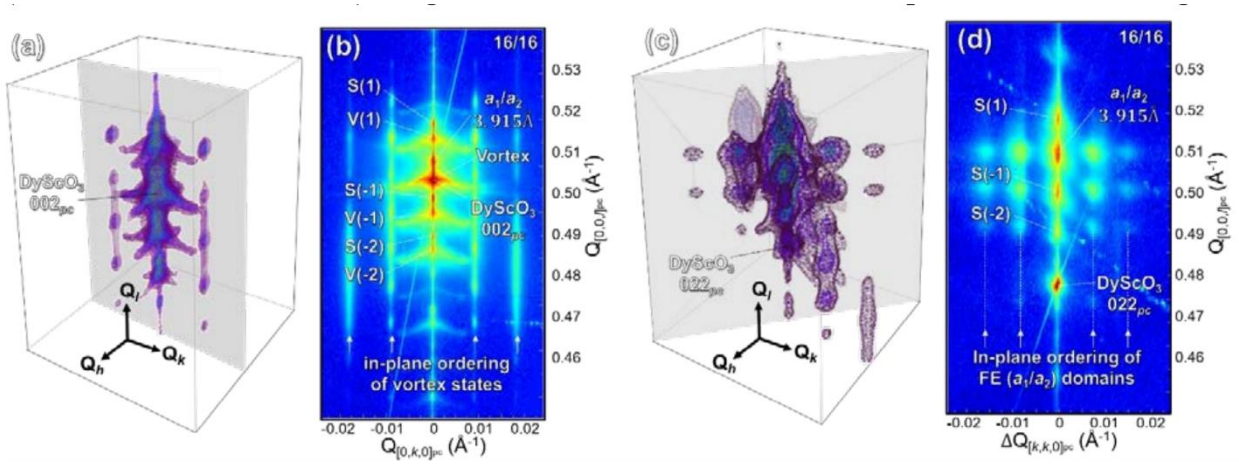

Figure 1.12 3D-RSMs indicate (a) 002_{pc} diffraction condition of the DSO substrate, (b) out-of-plane cut of the 3D-RSM indicating the in-plane ordering of vortex state, (c) off-axis 022_{pc} diffraction condition of the DSO substrate, and (d) 45° cut of the 3D-RSM indicating the in-plane ordering of ferroelectric domains. Adapted from [12].

The observation of the novel vortex state predicted by phase-field modeling extends further investigations on the phase competition and how the vortex phase evolves in the $(PTO)_n/(STO)_n$ superlattices as a function of periodicity [12]. In the range of small periodicity (n = 4-10), the system only forms the in-plane ferroelectric polarized a_1/a_2 domain structures with the 45° domain walls along the $[110]_{pc}$ (where "*pc*" denotes pseudocubic). The ferroelectric polarized a_1/a_2 domain is observed by synchrotron-based 3D reciprocal space maps (RSMs) and piezoresponse force microscopy (PFM) that corresponds to the predictions of phase-field modeling. The polar structure in the superlattices becomes more complicated to analyze due to the formation of vortices.

In the range of the intermediate scale of superlattices (n = 12-18), the phase coexistence of the ferroelectric and vortex state is observed and identified in the $(PTO)_n/(STO)_n$ superlattices (n = 16). As depicted in Figure 1.12 (a) and (b), the out-of-plane cut of 002_{pc} 3D-RSMs on $(PTO)_n/(STO)_n$ superlattices (n = 16) exhibits the presence of in-plane ordering in a spacing of ~11

nm that corresponds to the size and orientation of the vortex pairs. This in-plane ordering demonstrates a periodic modulation of the out-of-plane component of polarization as part of the vortex polarization that is also observed in DF-TEM studies [11].

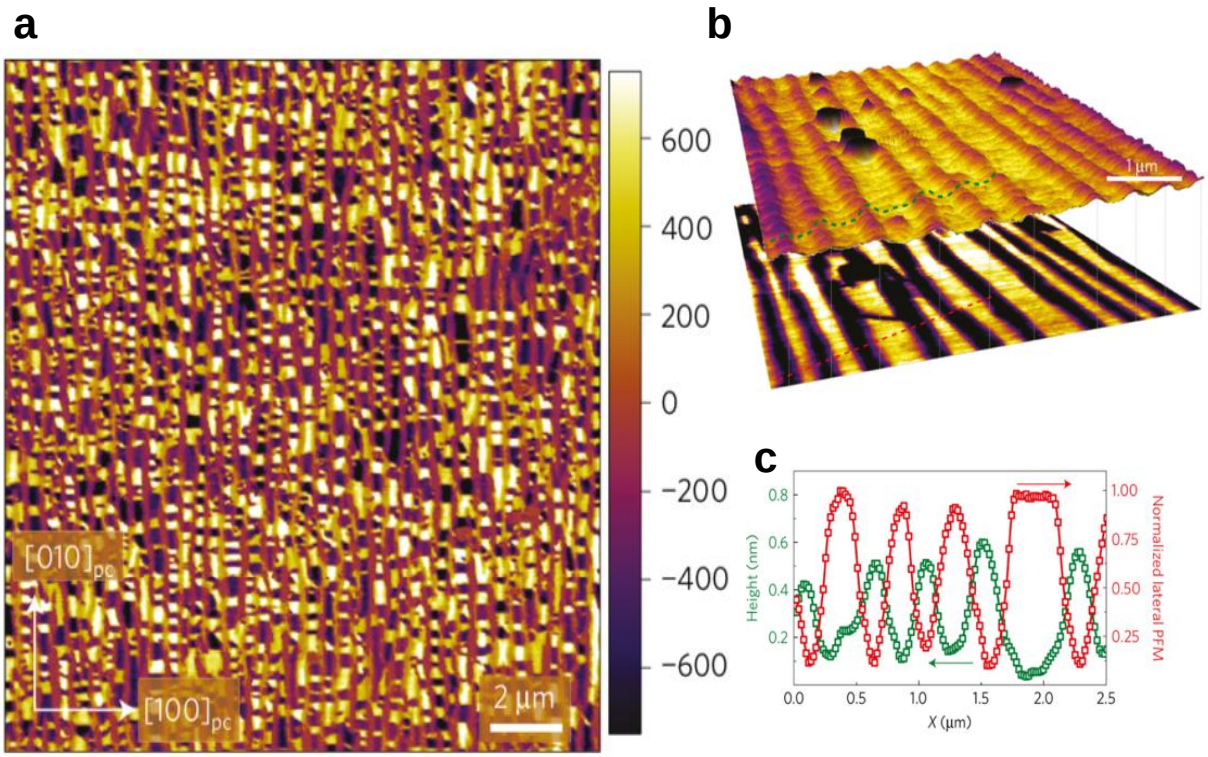

Figure 1.13 Identification of the polar state measured on $(PTO)_n/(STO)_n$ superlattices (n = 16) using PFM. (a) Large scale of alternating stripes of ~ 300 nm. (b) Regions of high and low surface height (top) correspond to low and high piezoresponse (bottom), which uniquely identify the ferroelectric and vortex state. (c) Line profile from the green dashed line in (b). Adapted from [12].

In the 45° cut of the off-axis 022_{pc} 3D RSMs, in-plane ordering occurs in a spacing of ~13 nm that corresponds to the ferroelectric a_1/a_2 domain structures, as depicted in Figure 1.12 (c) and (d). On the other hand, if the vector PFM is used to visualize the polar structures such as the complex super domains [88,89], the hierarchical structure forms a large-scale of ordered stripes with alternating checked black and white for a higher piezoresponse and brown for low response in a spacing of ~300 nm along the in-plane $[100]_{pc;}$ see Figure 1.13(a). The ferroelectric a_1/a_2 domain structures can be identified due to their higher in-plane response in lateral PFM. The same concept applies to the vortex state, which can be identified due to the lower in-plane response depicted in Figure 1.13 (c) and non-uniform polarization distribution compared to ferroelectric *a*-domains. Thus, the discovery of the phase coexistence of ferroelectric and vortex states are assembled to the hierarchical super-domains that correspond to the prediction of phase-field modeling, and the two phases can be switched reversibly by electric fields that provide the possibilities for device

applications. Further, as mentioned in equation 1-1, the toroidal moments of the vortex structure have been predicted to form in the low-dimensional ferroelectric state and give rise to the possibility of 3D polarization texture and chirality.

1.4.2 Emergent chirality of polar vortices in the superlattices

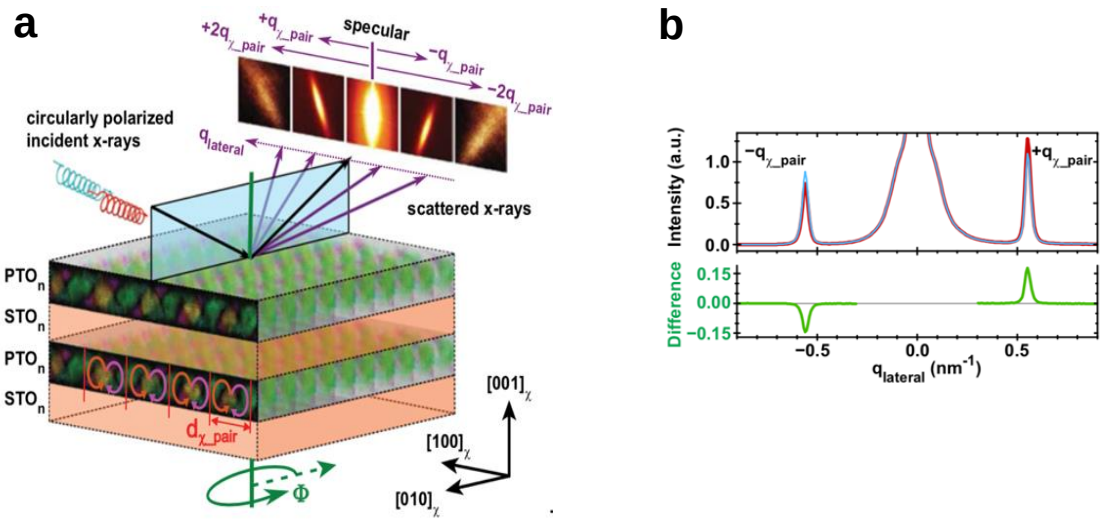

Figure 1.14 Schematic of the resonant X-ray diffraction (RSXD) measurement on $(PTO)_n/(STO)_n$ superlattices (n = 16), which reveal a diffraction pattern that corresponds to the array of polar vortices. (a) Specular beam with diffraction satellites of the polar vortices. (b) The top panel indicates a line cut of scatted intensity versus lateral momentum transfer using right and left circularly polarized X-rays. The lower panel demonstrates the difference of intensity (*i.e.*, the circular dichroism), which is indicative of chirality. The same signal is observed in chiral magnetic materials. Adapted from [13].

Chiral structures – just like left and right hands – are structures whose mirror images cannot be transformed for superimposition onto the original object. This particular geometrical property (named the handedness or chirality of the object) is widespread and occurs in common structures such as screws or sugar molecules. After the discovery of the phase coexistence of polar vortices and a ferroelectric phase, such a toroidal phase can possibly possess axial polarizations and demonstrate 3-D chirality, which is similar to the magnetic skyrmions [90–92] having topological spin whirls. This kind of spin whirl uses the unique spin-spin interaction called the D-M interaction [93–95] to stabilize a particular handedness with the lowest energy. The chiral signals found in the chiral magnets can also be detected on the polar vortices [13]. Using RSXD experiments to study chiral properties in reciprocal space as depicted in Figure 1.14 (a), the incoming X-ray was aligned along $[1\text{-}10]_o$, which is parallel to the preferred orientation of polar vortices in the superlattices.

According to the similar concept of out-of-plane ordering having ~10 nm spacings of polar vortices in the RSM study, the specular spot with satellite peaks was found by tuning the energy to the Ti $L_{3,2}$ edge, whose energy corresponds to the electronic transition from 2*p* to 3*d* orbitals. Probing the vortices with this energy is crucial for studying the chiral polarization structure because of the crucial role that the *d* orbitals play in ferroelectric distortions. The resonant X-ray circular dichroism that uses left-circular and right-circular polarized light can be found in Figure 1.14 (b), meaning that the diffraction intensity for left- and right-circular polarized light is different, which is indicative of the geometric lattice distortion with chiral properties. The detected intensity difference between the left and right circularly polarized light also indicates that the dichroism signal is asymmetric because the *q* vector changes from positive to negative, which is another indication of the chiral structure corresponding to the lattice distortion of the polar vortices. Hence, the emergent chirality of polar vortices is found. The next important questions to ask are whether it is possible to observe the chiral domains that indicate the different handedness, and whether it is possible to electrically control the chirality for optical devices.

.

1.5 Organization of Dissertation

This section presents the organization of the dissertation. Chapter 1 presents the basic knowledge of ferroelectrics and the scientific development of the vortex phase. Chapter 2 introduces the overview of experimental methods from this research, including pulsed laser deposition (PLD), transmission electron microscopy (TEM), x-ray diffraction (XRD), piezoresponse force microscopy (PFM), second harmonic generation circular dichroism (SHG-CD), and phase-field modeling. Chapter 3 employs a trilayer heterostructure to understand the vortex phase better and then engages to identify the toroidal phase in the combination studies of dark field TEM (DF-TEM), atomic resolution STEM, and phase-field modeling.

Chapter 4 studies the systematic work on phase stability, and the mechanism of vortex evolution is studied in PTO/STO trilayer heterostructures as a function of periodicity. This chapter also discusses another route to excite the vortex phase, which is the change of the number of confined $PbTiO_3$ layers in the ferroelectric heterostructures. Chapter 5 uses the zone axis techniques of electron diffraction and HR-STEM imaging with atomic displacement mapping to probe the antiparallel axial polarizations of the vortex phase, which are essential to the 3D chirality of the toroidal phase. Chapter 6 identifies and probes chiral vortex domains with different handedness from microscopic to macroscopic views, which have potential for high-density and multi-state memory device applications. Finally, Chapter 7 summarizes the results and discusses future directions for research.

Chapter 2
Experimental methods

This dissertation used experimental approaches to characterize the ferroelectric heterostructures. Pulsed laser deposition was used to fabricate the epitaxial heterostructures, courtesy of Margaret McCarter for high-quality of ferroelectric heterostructure. The primary structural characterization techniques were TEM and synchrotron-based RSM; these techniques were used to discover the emergence of the polar vortex phase and three-dimensional polar structures microscopically, courtesy of Margaret McCarter for RSM characterization. The macroscopic polarization distribution was probed by PFM, and further chirality was examined by the SHG-CD, courtesy of Molly May for chirality measurement. Finally, the simulations calculated by phase-field modeling were confirmed with the polar structures and the physics behind them, courtesy of Cheng Dai and Zijian Hong for the simulations.

2.1 Pulsed laser deposition

Pulsed laser deposition is one type of physical vapor deposition and an efficient ablation tool to make thin films of many different materials, including complex oxides [96], nitrides [97], and semiconductors [98]. In PLD, a high-intensity laser is focused onto a target of the material to be deposited. The vaporization of the target material creates a plume of plasma directed towards the substrate. With the proper growth conditions (temperature, pressure, *etc.*), the transfer of the material from target to substrate is nearly stoichiometric. In 1987, a high-quality $YBa_2Cu_3O_7$ thin film was successfully synthesized and kept the composition of the multicomponent target [99] [100]. The advantages of PLD include fast growth; lower cost than molecular beam epitaxy and chemical vapor deposition; and versatility in the use of various gases, which allows the researcher to have many opportunities to study complex oxides and achieve high-quality crystalline films.

.

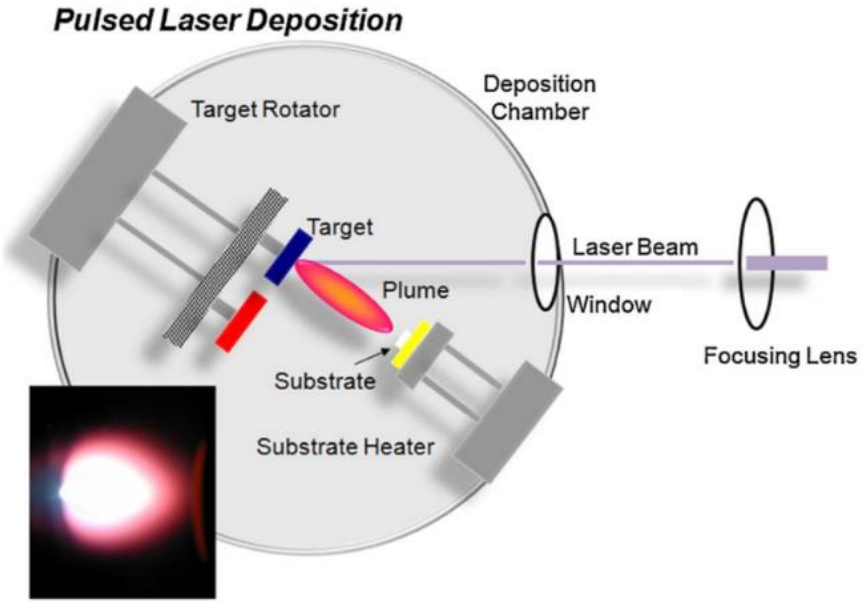

Figure 2.1 Schematic of the standard PLD system. Real plume imaging is inserted. Adapted from [14]

Figure 2.1 depicts the schematic mechanism of the standard PLD system. The high-powered pulsed laser beam is focused on the stoichiometric target. The energy from the laser beam ablates the target material, and the constituent atoms immediately undergo thermal evaporation and ionization. A high-energy plasma plume that includes ions, electrons, and neutrals is created and directed onto the heated substrate, as depicted in the inserted figure in Figure 2.1. Then, the materials start to deposit in the processes of nucleation, diffusion, and growth to form high-quality atomic films. The parameters that influence the deposition process are the laser energy density, background oxygen pressure, growing temperature, annealing time, substrate surface, and intrinsic

properties of the substrate (*e.g.*, lattice parameter/strain). These properties can be tuned to enable the growth of uniform and stoichiometric thin films.

During the growth, RHEED is used as the in-situ monitoring tool to ensure that the film is deposited layer-by-layer to achieve high-quality atomic scale epitaxial thin films. Using RHEED at a grazing angle on the sample surface results in only the top two or three atomic layers being probed. The diffracted beam is detected by fluorescence on a phosphorus screen that indicates the structural information from the surface of the thin film in Figure 2.2. Although the mechanism of the RHEED pattern is not the same as electron diffraction, it can be explained by k'- $k = G_{hkl}$: the Ewald sphere intersects the reciprocal lattice and forms the RHEED pattern on the screen and is the same concept as the diffraction in TEM and XRD. Actual growth conditions on the surface are not always ideal as on a flat surface. The RHEED patterns can be identified as specific growth conditions such as the spots that correspond to the perfectly smooth surface, streaks that correspond to the high density of atomic steps on a single crystal, stepped surfaces that correspond to the modulated streaks, or transmission spots that correspond to the growth of the 3D island in Figure 2.3.

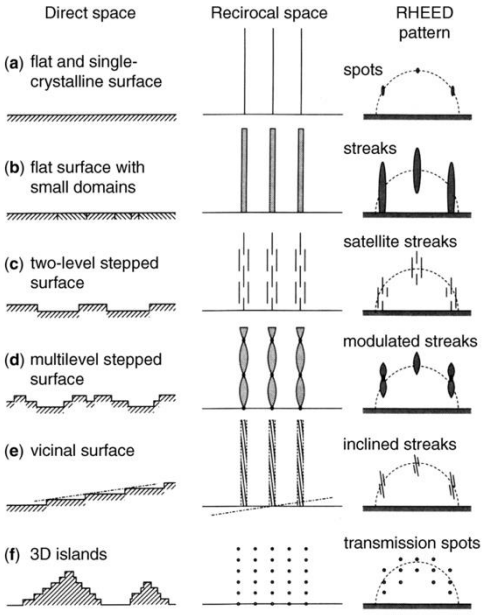

Figure 2.2 Schematic reflection high-energy electron diffraction (RHEED) diagram is on the top, and the growth mode with the intensity signal versus time is on the bottom. Adapted from [15].

The RHEED intensity oscillations can be used to monitor different stages of the layer-by-layer growth. Figure 2.2 (a)(b)(c) are typical examples of thin film growth. The island growth that is named the Volmer-Weber growth without RHEED oscillations has a strong interaction between atoms with low surface mobility in (a). The layer (2D) to island (3D) growth that is named the Stranski-Krastanov mode with high surface mobility and RHEED intensity oscillations has a damping issue for the amplitude in (b). The layer-by-layer growth that is named the Frank-Van der Merwe growth with high surface mobility is depicted in (c). Intensity oscillations come from

the repetition of the formation and coalescence of the 2D nuclei. When the 2D nuclei form, the number of diffuse scattered electrons from the surface increases, and the RHEED intensity decreases. The coalescence of the 2D nuclei transforms to a flat surface and increases the RHEED intensity. Typically, one intensity oscillation represents the deposition of one atomic layer (Figure 2.2 [c1] [c2] [c3]). The competition between Figure 2.2 (d) and (e) relates to the surface mobility and substrate terrace width. The higher surface mobility allows the atomic terrace growth and makes the interference diffraction. The low surface mobility represents longer diffusion length, and this can cause nucleation favorably on the surface step. After the growth of the first layer, it will reach a limit and stay at a constant RHEED intensity.

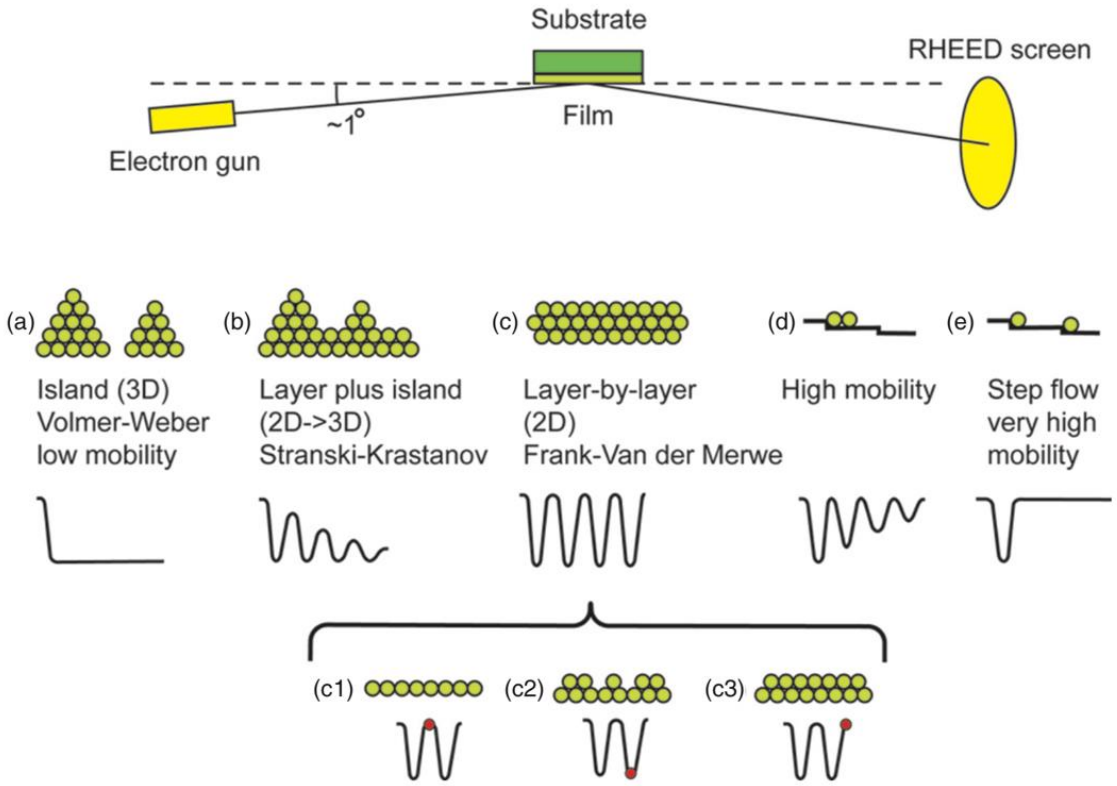

Figure 2.3 Schematic of different surface conditions via reciprocal space that corresponds to the RHEED patterns. Adapted from [16].

Figure 2.4 depicts one successful example in the superlattice experiment that indicates the layer-by-layer growth condition of $(PTO)_6/(STO)_6$ superlattices on the DSO substrate, using RHEED intensity oscillations verse times. Note that the PTO target has 20% excess Pb due to the high volatility of the PbO. The initial growth of PTO and STO can be monitored and counted in six layers respectively; see Figure 2.4 (a). If a stoichiometric target with 0% excess Pb is used, there is no intensity oscillation, and the 3D growth occurs; see Figure 2.4 (b).

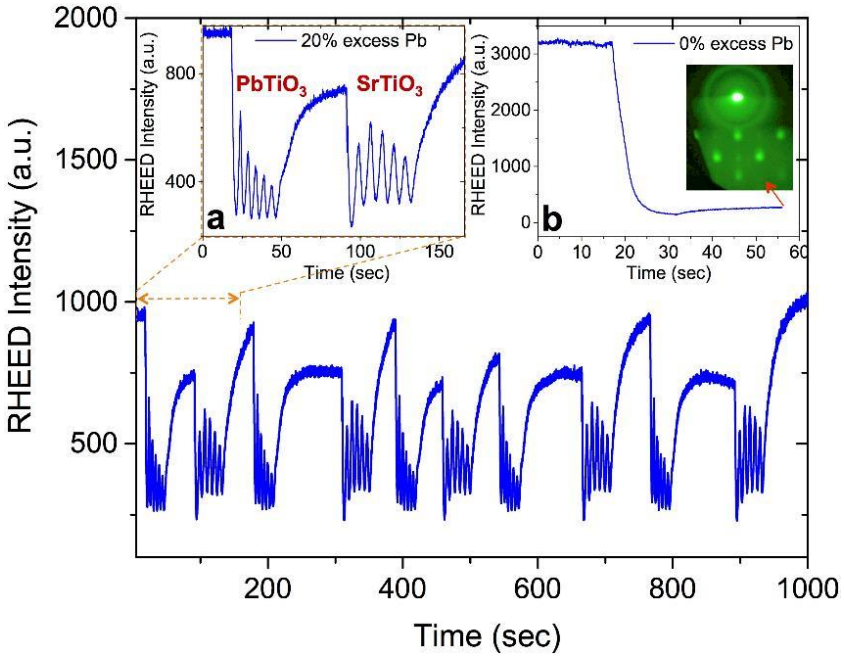

Fig. 2.4 RHEED intensity oscillations example: the controlled growth of $(PTO)_6/(STO)_6$ superlattices on a $DyScO_3$ $(110)_o$ substrate. Inset (a) depicts the intensity oscillations of the first period of growth of both six unit-cells of PTO and STO using 20% excess Pb of PTO target; (b) depicts RHEED intensity without oscillations indicating the 3D growth mode using 0% excess Pb of stoichiometric PTO target. Adapted from [11].

In this research, the confined ferroelectric heterostructures of symmetric $(PTO)_n/(STO)_n$ were synthesized by reflection high-energy electron diffraction-assisted PLD that used a KrF excimer laser. A buffer layer of ~5 nm of $SrRuO_3$ was deposited on the $DyScO_3$ $(110)_o$ substrates at a temperature of 700°C and an oxygen pressure of 50 mTorr. The bottom STO layer was deposited under the same conditions as $SrRuO_3$. Subsequent layers of PTO and STO were deposited at 620°C and 100 mTorr of oxygen pressure. For all materials, the laser fluence was ~1.5 J/cm^2, and the laser repetition rate was 10 Hz. After the deposition, ferroelectric heterostructures were cooled to room temperature in 50 Torr of oxygen. The films were grown from a single crystalline STO target and polycrystalline $SrRuO_3$ and $Pb_{1.2}TiO_3$ targets.

The main ferroelectric material is PTO. Other materials are the paraelectric material (STO), the buffer-layer and electrode material (SRO), and the substrate dysprosium scandate (DSO). The goal of this research is to utilize the high-quality synthesis to build up a dielectric/ferroelectric heterostructure and to observe the polarization distribution. In the bulk, PTO has the spontaneous polarization at room temperature along $[001]_{pc}$ under the phase transition temperature (490°C). The lattice constant of PTO [101] is a = 3.904 Å and c = 4.178 Å and it forms the tetragonal structure with space group *P*4*mm*. Strontium titanate is a paraelectric band insulator at room temperature with a cubic structure that has a lattice constant of a = 3.905 Å and space group *Pm*-

3*m*. The metallic ferromagnet SRO has an orthorhombic structure with the space group of *Pbnm* and bulk lattice parameter [102] of a = 5.567 Å, b = 5.530 Å, and c = 7.845 Å. The substrate DSO has an orthorhombic structure with the space group of *Pbnm* and bulk lattice parameter [103] of a = 5.440 Å, b = 5.717 Å, and c = 7.903 Å.

2.2 Transmission electron microscopy

The microstructure of the ferroelectric heterostructures was probed using conventional TEM and HR-STEM techniques at the National Center for Electron Microscopy (NCEM) at the Lawrence Berkeley National Laboratory (LBNL). The structure-property relationships in all dimensions were investigated using the cross-sectional and planar view TEM characterization, and the perfect TEM samples were needed.

2.2.1 TEM specimen preparation

- **Cross-sectional TEM Specimen**

Effective TEM imaging requires a perfect TEM thin specimen for characterization of its microstructure. The sample needs to be thin enough for the electrons to avoid multiple scattering, which creates artifacts in the diffraction and inelastic scattering and also provides a broad interest of view for statistical analysis. In our experiment, the thickness of the TEM specimen is usually below 50 nm to be electron-transparent without multiple scattering.

The steps to accomplish a cross-sectional TEM sample are as follows. First, the specimen is glued to the sacrificial silicon piece with Mbond 610 on the hot plate of 180°C for at least 3 hours; either that or the specimen is maintained at room temperature for 24 hours for hard bonding. Then, the specimen is cut into ~1.5mm slices with the diamond cutting saw and glued with crystal wax on the fixture for polishing. The silicon side is close to the edge for sacrifice. Mechanical polishing with Multiprep is employed to thin down the specimen using a series of diamond papers under the water flow from 30 um to 3 um and under lubricant from 1 um to 0.5 um for the first side. The surface of the specimen should be similar to a mirror without any scratches. Then, the TEM specimen is flipped and remounted with crystal wax.

On the second side, flat polishing is changed to the wedge polishing for about a quarter of a degree when the diamond paper is below 6 um. When the sacrificial silicon turns yellow and starts to disappear without polishing the substrate, the thinning process is about to end, and diamond paper of 1 um and 0.5 um is used to polish the surface without scratches. Finally, a molybdenum ring is glued on the specimen with Mbond 610 on the hot plate at 180°C in 3 hours or dried at room temperature for 24 hours. After that, the molybdenum ring with the specimen is soaked with acetone until both of them are detached from the fixture. Argon ion milling using a Gatan precision ion polishing system (PIPS) is engaged to thin down the TEM specimen below 50 nm, starting from the milling angle ± 4° with 4 keV and ending with 200 eV for surface cleaning. After milling

out the silicon layer and observing the dark color fringes of the local substrate, the cross-sectional TEM specimen is accomplished.

- **Planar view TEM specimen**

In contrast to the cross-sectional TEM specimen, planar view one does not require a sacrificial silicon layer. Most of the steps are the same, other than some differences which will be explained next. First, the specimen is cut within the size of the molybdenum ring and glued on the fixture for mechanical polishing to thin down the substrate side. A series of diamond papers is used from 30 um to 6 um for a flat polishing, and then the polishing angle changes to half a degree to make the wedge TEM sample. During observation of the disappearing of the specimen using diamond paper in 3 um, the final polishing can be processed using 1 um and 0.5 um without any scratches. In the argon ion milling part, the specimen is glued film-side down with wax, and all guns are top-oriented to thin down the substrate side. Finally, during observation of the color fringes of the holes or edges, final polishing can be used to clean the sample.

2.2.2 Conventional transmission electron microscopy (CTEM)

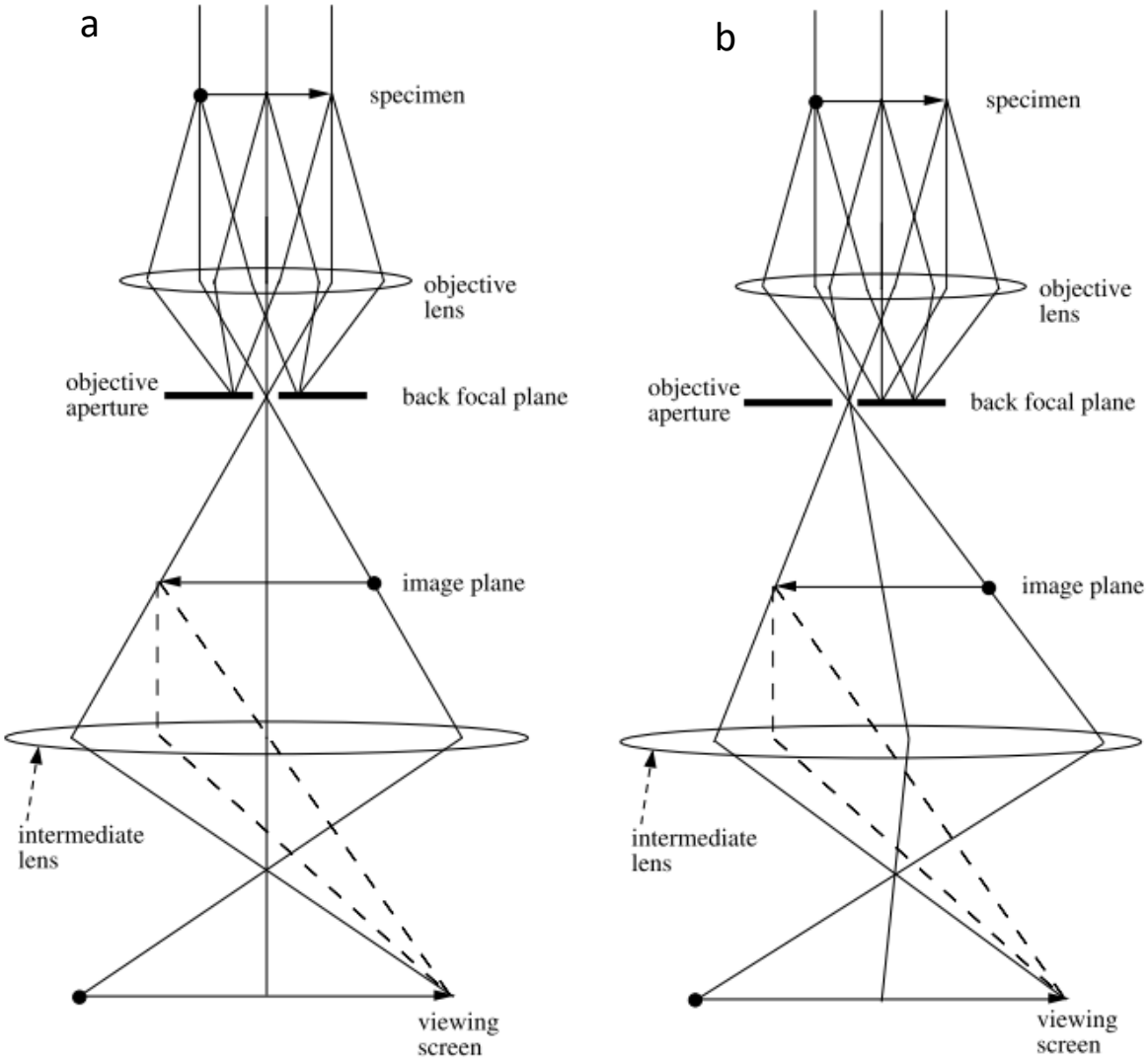

Figure 2.5 Ray diagrams in the conventional TEM mode. (a) Bright field mode. (b) "Dirty" dark field mode. Adapted from [17].

Currently, transmission electron microscopy (TEM) is a powerful imaging tool for zooming in on very high magnification and directly tracking exciting features on the atomic scale of the sample; for example, the resolution can reach up to 0.5Å [104] on aberration-corrected TEM. This technique can answer questions that arise from other property measurements by resolving the local structure that corresponds to different properties. The multifunctional TEM techniques, including electron diffraction, STEM, electron energy loss spectroscopy, and energy dispersive spectroscopy would provide the solution to not only the crystal structure, but also the chemical properties. For examples, lattice constants, strains, defects, symmetry, stoichiometry, and atomic valence. Furthermore, calculations of the experimental data are needed to extract the intrinsic properties behind the structure. The advanced probing technique in high spatial resolution and diffraction contrast are required to understand the arrangement of local structures and to study their intrinsic

properties regarding the structure-property relationships of noncentrosymmetric ferroelectric materials.

Transmission electron microscopy imaging utilizes the intensity of contrast for structural characterizations. When 300KV electrons of high energy penetrate through the TEM thin foil, the plane waves of the electrons propagate through the crystalline materials to have a diffraction contrast that indicates the different intensity of electron diffraction through the sample. This diffraction contrast is from the interference between the transmitted electron beam and the diffracted beam and demonstrates the areas of different intensity of the diffracted beams. Therefore, the constructive interference would have high intensity, but destructive interference would have low intensity for the contrast. However, the TEM sample cannot be too thick, otherwise the electron scattering will not allow the electrons to penetrate the sample. Usually, the best TEM sample for high-resolution TEM imaging is less than 50 nm.

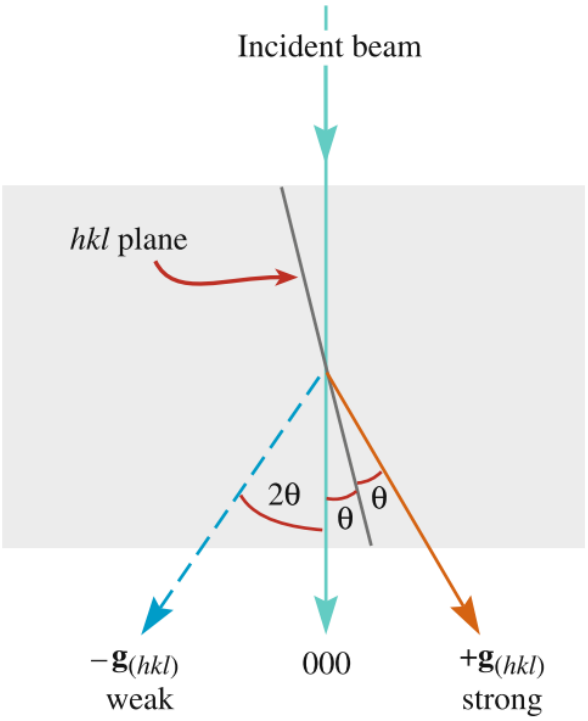

Figure 2.6 The ray diagram of two beam conditions demonstrating the incident beam at 000 spot. The $+g_{(hkl)}$ becomes strong due to the *hkl* plane at the Bragg condition. Adapted from [18].

Figure 2.5 indicates how there are two modes in the conventional TEM after the electron beam penetrates through the TEM sample and is focused by the objective lens. The left mode is the bright field mode, in which the objective aperture only allows the transmitted electron beam to be magnified by the intermediate lens and is projected on the screen to form the bright field imaging. The right mode is the dirty dark field mode, in which the objective aperture only allows some diffracted electrons to penetrate to form the dark field imaging. On the back focal plane, the diffraction pattern in the reciprocal space represents the structural information of materials, and a specific diffraction spot can be selected by the objective aperture to form dark field imaging. Both modes can achieve effective diffraction contrast if the objective aperture is inserted. Without the

objective aperture, the transmitted beam would recombine with the diffracted beam to cancel the intensity of the diffraction contrast.

Figure 2.6 depicts how the dark field in two beam conditions is utilized to obtain the best diffraction contrast. This technique only needs to tilt the sample to one strong diffracted beam and the transmitted beam. That high-intensity diffraction spot has been diffracted by the *hkl* plane that is at the Bragg condition. Therefore, the area indicating bright contrast is at the Bragg condition by that specific *hkl* plane in the dark field imaging, and its g-vector would indicate the orientation information. Another useful technique in this work is to utilize the +g and -g vector imaging to observe the breaking of Friedel's law in dynamical diffraction [17]. Friedel's law defines F(*hkl*) = F(-*h*-*k*-*l*), such that intensity variation cannot be discerned from its inverse for a centrocymmetric material. This usually happens in the diffraction. Regarding the distinction between centrosymmetric and noncentrosymmetric, the breaking of Friedel's law is an excellent tool for the noncentrosymmetric PTO and centrosymmetric STO materials.

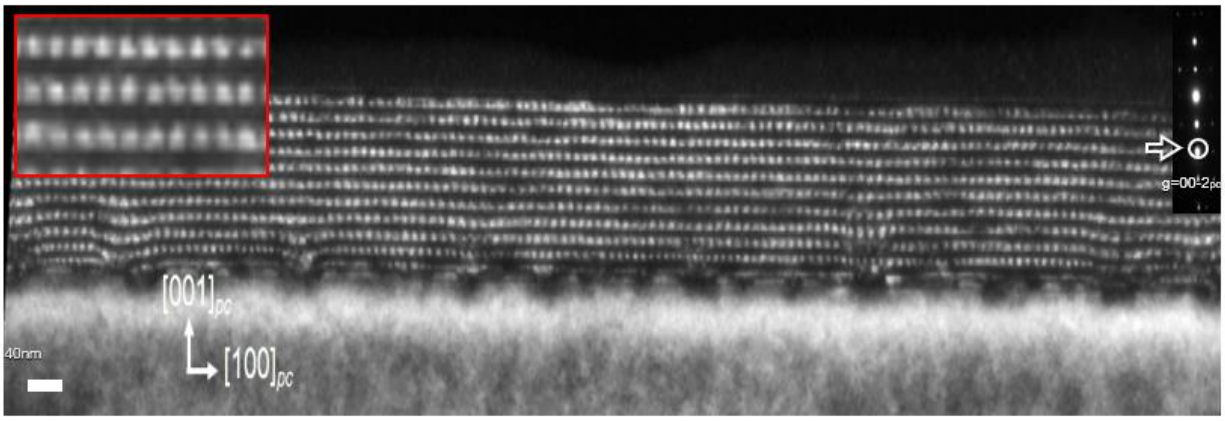

Figure 2.7 Diffraction contrast TEM of $(PTO)_{10}/(STO)_{10}$ superlattices on $DyScO_3$ $(110)_o$ substrate using $[00\text{-}2]_{pc}$ g-vector, showing the out-of-plane modulations inside the PTO layers.

The following is one successful example of DF-TEM in two beam conditions from Figure 2.7. This sample is the $(PTO)_{10}/(STO)_{10}$ superlattice on the $DyScO_3$ $(110)_o$ substrate, and its diffraction contrast that uses the $[00\text{-}2]_{pc}$ g-vector in the out-of-plane direction indicates the bright periodic modulations in a spacing of ~10 nm only in the PTO layers that correspond to the size of polar vortices in the atomic polarization mapping [11]. These periodic modulations with bright contrast have orientations toward the g-vector direction; these modulations are essential parts to form the polar vortices. Therefore, by using +g/-g vector images in both in-plane and out-of-plane directions to confirm the intensity reversal, the polar vortices can be fully characterized for its polarization distributions in a cross-sectional view.

2.2.3 High-resolution scanning transmission electron microscopy

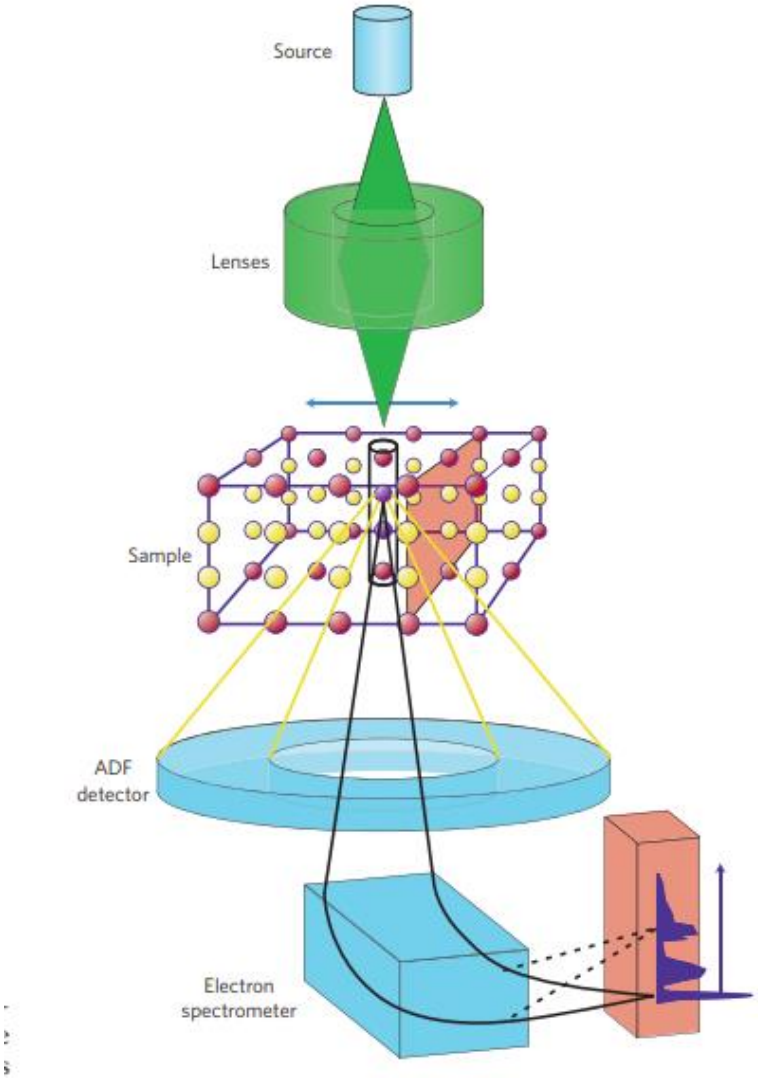

Figure 2.8 The working diagram of the STEM. Adapted from [19].

Conventional TEM allows a parallel electron beam that is exposed on the TEM sample to elastically scatter to form phase-contrast images. These images might have ambiguous information in high resolution due to the mixing of the transmitted beam and diffracted beam. In contrast to the STEM in Figure 2.8, the beam uses focused electrons to raster across the sample in incoherent scattering, and the annular dark-field detector only collects the scattered electron to form the dark-field images without considering the phase differences and interferences because the contrast is coming from different atoms. If the inner angle is changed to the high angle, high angle-scattered electrons compose the high-angle annular dark-field (HAADF) imaging or Z-contrast imaging. Hence, the HAADF imaging is more straightforward to interpret than HR-TEM imaging and is very helpful for observing domain structures in the ferroelectric materials in this research.

After acquiring the sharp atomic resolution HAADF imaging on Cs-corrected STEM as depicted in Figure 2.9, the raster distortion of the TEM sample is a major problem for processing the displacement mapping. Using a pair of HAADF images at the same location in orthogonal scan directions enables the calculation of a pre-distortion image to minimize the slow scan axis [105]. Using the corrected HAADF imaging enables atomic displacements to be calculated and extracted for atomic polarization mapping using A-site and B-site sublattice offset measurement [83]. The relative shifts of the cations can be used as the electric dipole moment, and the offset refers to the polarization in the displacive perovskite ferroelectric materials. The anions, which are oxygen in perovskite ferroelectrics, have weak electron scattering with low signal-to-noise ratios and are not easily observed in the HAADF imaging. For example, the Ti ions in PTO can be used to determine the electric dipole and indicate the offset of the Ti-centered oxygen octahedra.

The following describes the bulk PTO at room temperature for reference. The Ti and O ions are shifted by 16.2 pm and 47-49 pm respectively in the direction opposite to the polarization that is relative to the Pb lattice [106]. The following describes the processing to calculate the displacement vector mapping. Figure 2.9 (c) depicts how a trust-region algorithm in Matlab is used on the four-parameter spherical Gaussians to fit each atomic position on the corrected HAADF imaging to solve the non-linear least squares. The fitting results are performed for five-atom clusters of the B-site-centered perovskite unit cell. Figure 2.9 (d) depicts how the difference between the atom position and the mean position of the surrounding four opposite-type cations was calculated as the displacement for each atom. A pseudocubic grid was used to index and define the image in the *x*-*z* Cartesian plane ($x = [100]_{pc}$, $z = [001]_{pc}$) for an atom at grid position i,j. This corresponds to mean neighbor positions (MNP) of:

$$MNPx_{ij} = 1/4[x_{i-0.5,j-0.5} + x_{i-0.5,j+0.5} + x_{i+0.5,j+0.5} + x_{i+0.5,j-0.5} \quad (2\text{-}1)$$

$$MNPz_{ij} = 1/4[z_{i-0.5,j-0.5} + z_{i-0.5,j+0.5} + z_{i+0.5,j+0.5} + z_{i+0.5,j-0.5} \quad (2\text{-}2)$$

In Figure 2.9 (e), the order for *A*-sites and *B*-sites is reversed to maintain a consistent displacement vector sign:

$$\mathrm{P_{A\text{-}site}} = \left(x_{ij} - MNPx_{ij}\right)\hat{x} + \left(z_{ij} - MNPz_{ij}\right)\hat{z} \quad (2\text{-}3)$$

$$\mathrm{P_{B\text{-}site}} = \left(MNPx_{ij} - x_{ij}\right)\hat{x} + \left(MNPz_{ij} - z_{ij}\right)\hat{z} \quad (2\text{-}4)$$

Therefore, the displacement vector of A and B atoms is the offset of the atom position (x_{ij}, y_{ij}) versus the center of the mass of four neighbors. The calculated displacement vector is usually parallel to the full electrical polarization of the crystalline material in the bulk. The vorticity of the displacement vector field can be calculated using the curl of polarization, which is $\nabla \times \boldsymbol{P}$, or $\left(\frac{\partial \mathrm{P}_Z}{\partial \mathrm{X}} - \frac{\partial \mathrm{P}_X}{\partial \mathrm{Z}}\right)\hat{y}$ in the *x*-*z* plane, which refers to the cross-sectional view, and *y*, which refers to the direction of the electron beam. The polarization gradient terms $\frac{\partial \mathrm{P}_Z}{\partial \mathrm{X}}$ and $\frac{\partial \mathrm{P}_X}{\partial \mathrm{Z}}$ are calculated by a weighted least-squares fit of a two-variable (*x* and *z*) 1st order polynomial to P_x or P_z at each atom site, with a fit area extending to 12 surrounding atoms.

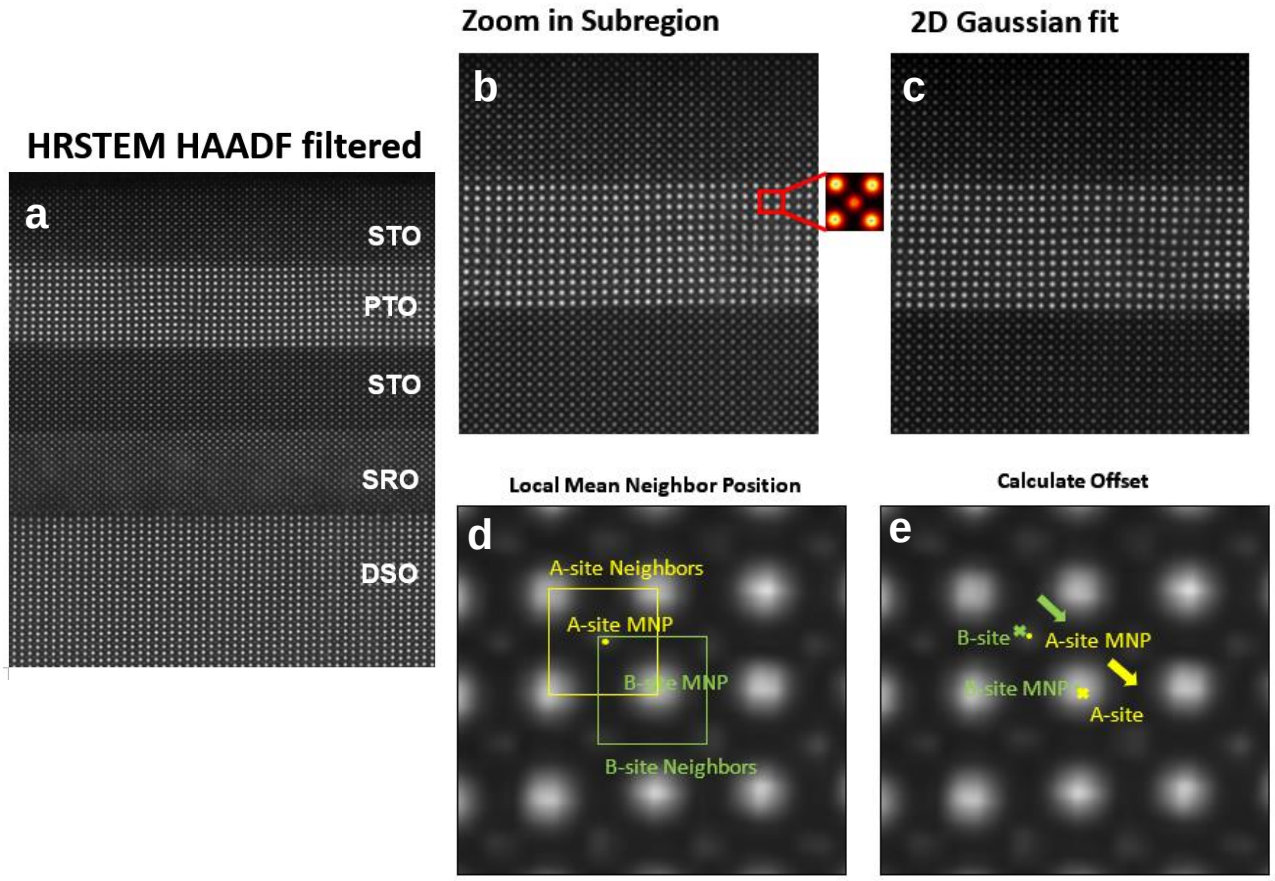

Figure 2.9. Processing of polarization mapping on the $(PTO)_n/(STO)_n$ trilayer on the DSO (110) substrate. (a) HAADF imaging indicating the sharp atomic columns. (b) A magnified view of the boxed subregion in (a) that indicates two overlapping unit cells, namely the A-site-centered perovskite unit cell and the B-site-centered perovskite unit cell. (c) The Gaussian fit of a region of a HAADF STEM image. (d) The mean position of each atom's four nearest cation neighbors (MNP, mean neighbor position) is used to determine a relative sublattice offset. (e) A polar displacement vector (yellow arrow for A-site and green arrow for B-site) is taken as the difference between each atom (filled circle) and the MNP ('×'). Opposite signs for provided for A- and B-sites to maintain a consistent direction.

2.3 Synchrotron-based x-ray diffraction (XRD)

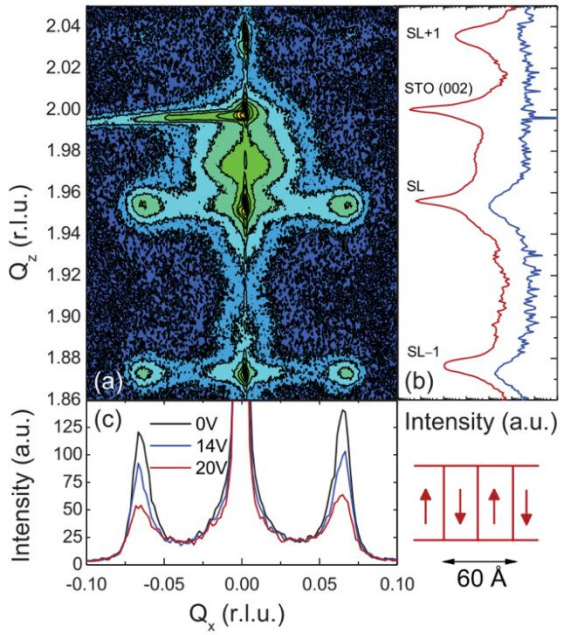

Figure 2.10 (a) RSM of PTO/STO superlattices indicating the substrate STO (002) reflection and three superlattices peaks (SL, SL+1, SL-1). (b) Intensity profile along main Bragg peaks (red) and satellite peaks (blue). (c) Intensity around the main SL peak under different applied electric fields. The identified polar structure is 180° ferroelectric domains with a spacing of 60 Å. Adapted from [20].

X-ray diffraction is an essential tool for structural characterization and is used to discover the crystal structure in all kinds of materials such as powders, thin films, and crystals because their functional properties are related to their stable phases. Since crystalline materials have a periodic structure, monochromatic X-rays can be diffracted, and the constructive interference will satisfy Bragg's law:

$$n\lambda = 2d\sin(\theta) \tag{2-5}$$

where n is the order of diffraction (an integer), d is the spacing between crystal planes, θ is the incident angle of the X-rays, and λ is the wavelength of X-rays. This non-destructive method can identify the crystalline phases qualitatively and elucidate the 3D crystal structures with lattice parameter information to analyze further properties. To observe the possible details of the materials such as all lattice constants to analyze strain condition, asymmetry and multiple scans in a range of tilting are needed as the RSM. This technique is very useful for investigating the polar structures. For example, the RSM of PTO/STO superlattices [20] demonstrate satellite peaks indicative of the 180° ferroelectric domains in a spacing of 60 Å in Figure 2.10.

Synchrotron-based X-ray diffraction studies were performed at beamline 33-BM-C at the Advanced Photon Source at the Argonne National Laboratory. Three-dimensional RSMs were

acquired using the Huber 4-circle diffractometer and the PILATUS 100K pixel detector. The high flux of X-rays available at the synchrotron, coupled with 3D-RSMs, enables the measurement of satellite diffraction peaks that are correlated to orderings of both the in-plane and out-of-plane polarization components in the heterostructures. The synchrotron-based XRD has the same working principle as the general laboratory-based XRD, but the difference is that the X-rays used in synchrotron-based diffraction have a higher energy and intensity. The synchrotron uses magnets and radio frequency waves to accelerate charged particles, such as electrons, at high speed around the magnetic storage ring. The magnetic fields deflect the high-speed electrons, and the acceleration of these charges creates a continuous spectrum of light of different wavelengths such as visible light, soft or hard x-rays, and ultraviolet rays, which can be chosen for investigation of a wide range of materials.

There are three main different usages of the synchrotron XRD: diffraction and scattering, spectroscopy, and imaging. In this research, the diffraction experiments were employed to measure the nanoscale topological structures in three dimensions in ferroelectric heterostructures. The most significant advantage of synchrotron XRD is the high flux of X-rays, which can detect the weak signals or tiny features with greater accuracy than the laboratory XRD. Additionally, there are still some specialties such as the high energy beams that can penetrate deeper into materials, the synchrotron beam that can be polarized or be set at high frequency for specific experiments, and 3D reciprocal space mapping around a specific Bragg reflection.

2.4 Piezoresponse force microscopy

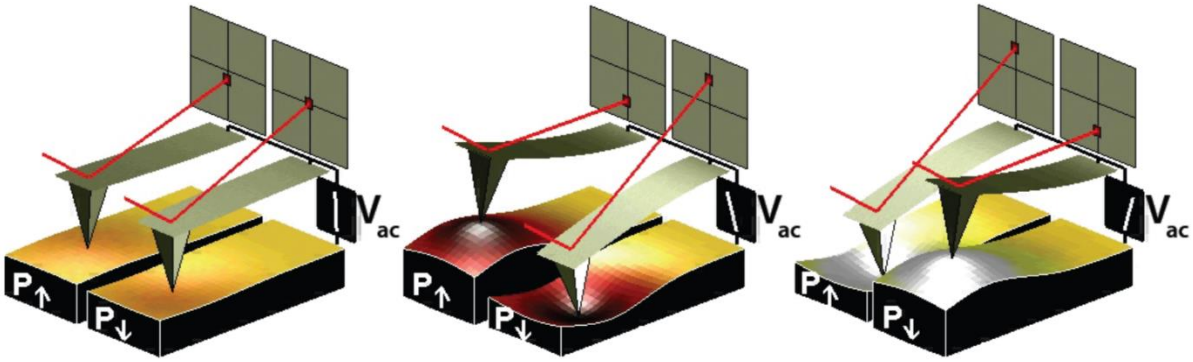

Figure 2.11 The concept of PFM indicating sample deformation and deflection of the cantilever when applying AC voltage. Adapted from [21].

Piezoresponse force microscopy is a powerful tool that uses the capability of atomic force microscopy (AFM) to measure the electromechanical coupling of the specimen. Piezoresponse force microscopy was first performed in [107], specifically to study the piezoelectric and ferroelectric behaviors of the materials due to the inverse piezoelectric effect. The piezoelectric effect is the ability to convert mechanical energy into electrical energy, and the inverse-

piezoelectric effect is the reversible process by which a material is strained as the result of applying an electric field. Piezoresponse force microscopy applies an AC bias voltage between bottom electrodes and the conductive Pt/Ir-coated AFM tip that acts as the top electrode in the specimen to induce mechanical oscillations when the tip is scanning on the surface. The local region of polarization direction and the piezoresponse coefficient can be obtained by the sign of the response of the first harmonic component of the tip deflection, which is the surface expansion or contraction that results in the amplitude and phase information by the reflected laser on a four-quadrant photodetector.

As depicted in Figure 2.11, when the ferroelectric material has a c-domain pointing downward and a positive electric field is applied, the scanned local region will expand. When a negative electric field is applied, the scanned local area will contract. Thus, if the ferroelectric materials have c-domains that point upward and downward and are applied with the positive electric field, the different behaviors will indicate the phase information as an indication of the polarization direction of the local region when applying the oscillating voltage. At the same time, topography information can be obtained from the deflection of the tip, which is the function of the AFM. The asylum research MFP3D system and a mode of dual amplitude resonance tracking (DART) were used in this research. This mode scans at the resonance frequency of the cantilever to obtain maximum signals due to the weak piezoresponse in the picometer scale. The resonance frequency frequently changes during the scanning due to the interference by the combination of the tip, sample surface, and cantilever in contact mode. Therefore, this mode scans in a range between two frequencies to lock in the resonance and reliably obtain the response.

If the polar structure is correlated to the three dimensions, measurements of piezoresponse will need to perform vector PFM at the same location, including the in-plane and out-of-plane directions. In the in-plane measurement, the out-of-plane electric field would cause the local regions to have different shear conditions that result in the left or right polarization direction. It should be noted that there is no contrast along the long axis of the tip, so the sample needs to rotate 90° to measure another direction when doing the in-plane measurement. Then, ferroelectric switching behaviors can be probed by applying a DC bias on the tip to flip the domain orientation for device applications.

2.5 Second harmonic generation

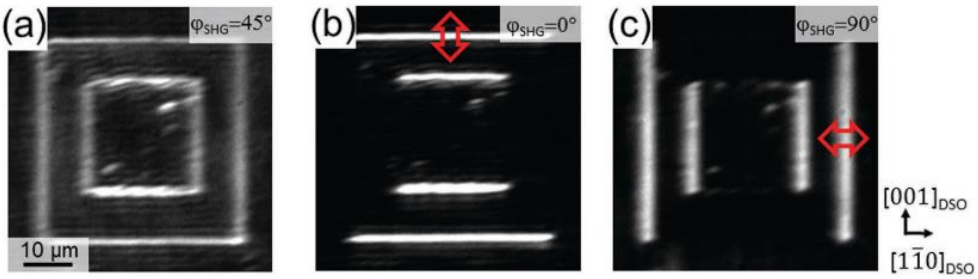

Figure. 2.12 SHG imaging indicating (a) all voltage-induced 180° c-domain walls of the 75 nm PZT film, (b) selective detection of c-domain walls with a $[001]_o$ polarization component, and (c) with a $[1\text{-}10]_o$ polarization component. Adapted from [22].

Optical second harmonic generation (SHG) circular dichroism (CD) measurements were employed to observe the spatial chirality in the $(PTO)_n/(STO)_n$ trilayer heterostructure. These measurements probe the symmetry breaking with right-handed and left-handed circularly polarized light. Second harmonic generation is a nonlinear optical technique that is mainly used to examine any symmetry breaking in long-range ordering for which ferroelectric materials are a strong candidate [108,109]. Figure 2.12 depicts how SHG imaging can resolve the voltage-induced domain walls using angle-dependent SHG light to exhibit all 180° c-domain walls (with linear polarization at 45°) in (a), only $[001]_o$ polarization component of 180° c-domain walls (with linear polarization at 0°) in (b), and $[1\text{-}10]_o$ polarization component of 180° c-domain walls (with linear polarization at 90°) in (b) [22].

Therefore, changing the linear polarization component used in SHG can selectively probe anisotropy in the ferroelectric polarization direction. Figure 2.13 depicts the working principle of how two incident photons with low-frequency ω are absorbed simultaneously to induce the electronic transition from ground state to excited state. The excited state then decays and emits one photon to the ground state with double frequency 2ω. Taylor expansion can be used to express non-linear polarization in the powers of the electric field:

$$P(\omega) = \chi^{(1)} \cdot E(\omega) + \chi^{(2)} \cdot E(\omega)^2 + \chi^{(3)} \cdot E(\omega)^3 + \cdots \tag{2-6}$$

where $\boldsymbol{\chi^{(n)}}$ are tensors of increasing rank that correspond to the n^{th} order susceptibility of the material [23]. The linear term $\boldsymbol{\chi^{(1)} \cdot E(\omega)}$ indicates that the polarization of a material is proportional to the electric field. A noncentrosymmetric material that is lacking in inversion symmetry can be easily detected by SHG measurement due to the symmetry breaking. Ferroelectric materials are noncentrosymmetric, and their square of spontaneous polarization is

proportional to the second-order non-linear optical susceptibilities $\chi^{(2)}$ because the second order polarization is proportional to the square of the electric field with an always positive result. Furthermore, $\chi^{(2)}$ is correlated to the SHG signal which is non-zero for lacking mirror symmetry. The SHG response of a material to light polarized along a crystal axis is determined by its symmetry properties, which determine the elements of its second-order susceptibility tensor. For asymmetric structures these susceptibilities are distinct for different axes, which leads to a strong (weak) SHG response for dipole moments along axes with low (high) symmetry, which is associated with high (low) susceptibility. For circularly polarized excitation light, the rotational symmetry properties of the material's nonlinear susceptibility tensor are probed. Conventional CD examines chemical structures and conformational changes in processes such as protein folding by measuring absorption differences of LH and RH circularly polarized excitation, which are correlated with changes in the intrinsic chirality of the secondary and/or tertiary protein structure. More recently, plasmonic structures with highly asymmetric optical responses to LH and RH polarized light were fabricated [110] and the use of circularly polarized light to control the occupation of spin polarized valley states in 2D semiconductors [111] was pioneered. Additionally, circular dichroism is the difference in SHG intensity for left-handed and right-handed circularly polarized lights, which will be different for chiral signals. Therefore, using SHG measurements with left-handed and right-handed circularly polarized light enables understanding of the symmetry breaking and chirality of $(PTO)_n/(STO)_n$ heterostructures.

In this work, SHG circular dichroism measurements were made in reflection mode using a Ti/Sapphire oscillator for excitation with ~100 fs pulses with a center wavelength of 800 nm, a 78 MHz repetition rate, and an average power of 1 mW. Pulses with linear polarization were sent through a ¼ wave plate to generate left-handed or right-handed circular polarization and focused on the sample using an objective lens (NA = 0.8, WD = 4 mm). The back-scattered SHG signal was detected using a spectrometer (SpectraPro 500i, Princeton Instruments) with a charge-coupled device camera (ProEM+: 1600 eXcelon3, Princeton Instruments). Confocal scanning microscopy was used to create images of the SHG intensity that were generated with left-handed circularly polarized light and subsequently with right-handed circularly polarized light. The left-handed and right-handed circularly polarized intensity were used to calculate images that indicate the spatial variation in the CD signal by applying equation 2-7 to the intensities at each image pixel.

$$\frac{I_{left\ handedness} - I_{right\ handedness}}{I_{left\ handedness} + I_{right\ handedness}} \tag{2-7}$$

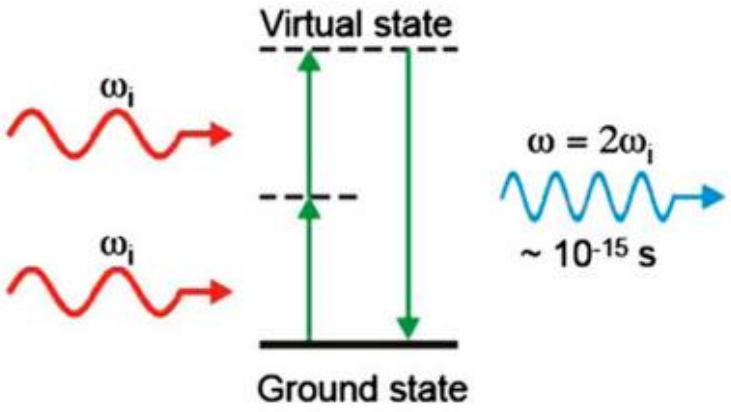

Figure 2.13 Principle of how to generate second harmonic by absorption of two incident photons. Adapted from [23].

2.6 Phase-field modeling

These simulations were performed by phase-field modeling, which is a phenomenological approach that provides significant insights on the energy contributions to and mechanism of the stability of the ferroelectric topological structures. Phase-field modeling has been successfully employed to study domain structures and evolution [112] [113], switching behaviors [114], and phase diagrams [24,115] in ferroelectric thin films. In this style of modeling, the energy contributions can be calculated by using the polarization vector $\vec{p} = (p_x, p_y, p_z)$ as the order parameter to describe the polarization distribution. The polarized structure is described by various interactions in the system, and its stability is determined by the total energy, which includes Landau energy, elastic energy, electrical energy, and gradient energy:

$$F = \int (f_{Landau} + f_{Elastic} + f_{electric} + f_{Gradient}) dV \tag{2-8}$$

The Landau energy is the bulk-free energy, which is a double well in traditional ferroelectrics. The elastic energy typically comes from the total strain conditions of the material that is related to the spontaneous polarization and the substrate. The electric energy is contributed by the electrostatic boundary conditions (*e.g.*, depolarization fields at ferroelectric-dielectric interfaces, *etc.*) The gradient energy arises from the polarization changes associated with an inhomogeneous polarization distribution. Each energy density can be written as follows:

$$f_{Landau} = \alpha_{ij} P_i P_j + \beta_{ijkl} P_i P_j P_k P_l + \gamma_{ijklmn} P_i P_j P_k P_l P_m P_n + \cdots \tag{2-9}$$

$$f_{\text{elastic}} = \frac{1}{2} C_{ijkl} e_{ij} e_{kl} = \frac{1}{2} C_{ijkl} (\varepsilon_{ij} - {\varepsilon_{ij}}^0)(\varepsilon_{kl} - {\varepsilon_{kl}}^0) \tag{2-10}$$

$$f_{\text{electric}} = -\frac{1}{2}K_{ij}\varepsilon_0 E_i E_j - E_i P_i. \tag{2-11}$$

$$f_{\text{gradient}} = \frac{1}{2}G_{ijkl}P_{i,j}P_{k,l} \tag{2-12}$$

In the Landau free energy density, the expression is a polynomial equation, where the odd terms vanish due to the inversion symmetry. In the elastic energy density, the elastic strain is considered, and C_{ijkl}, e_{ij}, ε_{ij}, $\varepsilon_{ij}{}^0$ are the elastic stiffness tensor, elastic strain, total strain, and eigen strain respectively. In the electric energy density, ε_0 is the dielectric permittivity of free space, κ_{ij} is the background dielectric constants of the superlattice film, and E_i is the local electric field defined as the gradient of the electric potential $E_i = -\nabla_i \varphi$. The gradient energy density has the pseudo-cubic assumption, and G_{ijkl} is the gradient coefficient tensor; $P_{i,j}$ stands for the spatial differential of the polarization vector: $P_{i,j} = \frac{\partial P_i}{\partial x_j}$. A more detailed description of the film-based phase-field method and the iteration method for solving anisotropic elastic equations can be found elsewhere [112,116,117]. Later, the evolution of the polarizations to the stable states can be calculated by minimizing the total energy using time-dependent Ginzburg-Landau (TDGL) equations:

$$\frac{\partial P_i}{\partial t} = -L\frac{\delta F}{\delta P_i(\vec{r},t)}(i = 1,2,3) \tag{2-13}$$

where L is the kinetic coefficient related to the interface mobility, and r and t are spatial position vectors and time respectively. As a result, the local polarization vectors from the solution provide the microstructure of the polarization distribution in three dimensions, and this prediction can enable the discovery of the real polarized state in the experiments.

In this work, the pseudo-cubic lattice constants for PTO and STO were taken as 3.9547 Å and 3.905 Å respectively [116]. The anisotropic in-plane lattice constants for the substrate $DyScO_3$ were taken from the literature to calculate the misfit strain [118]. The material constants for the PTO and STO used in the simulations were gleaned from the literature and include the Landau potentials, elastic constants, electrostrictive coefficients, background dielectric constants, and gradient energy coefficients [103,112,119–121]. The three-dimensional phase-field simulation of the $[(STO)_{10}/(PTO)_{10}]_n$ multilayer system is performed using discrete grids of $(80\Delta x)\times(80\Delta y)\times(250\Delta z)$ with $\Delta x = \Delta y = \Delta z = 0.4$ nm, where Δx, Δy, and Δz are in real space. The thickness of the substrate, film, and air are $30\Delta z$, $(20n+9)\Delta z$, and $(211-20n)\Delta z$ respectively, where n is the number of the confined PTO layer. In the film, alternating nine grids of PTO layers and nine grids of STO layers were incorporated to simulate the multilayer system. The periodicity of the PTO and STO layers effectively describes the experimental observations. Periodic boundary conditions are assumed in both the x and y directions, and a superposition method is used along the z-direction [120]. The short-circuit electric boundary condition was used, where the electrical potential was zero on the top and bottom. A mixed mechanical boundary condition was used, where the out-of-plane stress on the top surface of the film was free while the displacement was zero at the bottom, far from the film/substrate interface. Random noise was used as the initial nuclei.

Chapter 3
The emergence of polar vortices in $(PTO)_n/(STO)_n$ trilayer heterostructures

After the discovery of polar vortices in the PTO/STO artificial superlattices, the mysteries of this state such as phase stability, the formation mechanism, and the properties remain unknown. When attempts were made to solve these mysteries in the PTO/STO artificial superlattices, several difficulties in the measurements occurred. Hence, the material system is changed to the simplest PTO/STO trilayer heterostructure with only one confined PTO layer. This chapter explains why this researcher studies the PTO/STO trilayer system instead of superlattices and how to measure and identify the vortex phase that combines the experiments and simulations. The combination studies of DF-TEM in two beam conditions (HR-STEM with displacement mapping and phase-field modeling) are utilized to identify the polar structure of a confined PTO heterostructure. Thus, the emergence of the vortex phase in a confined PTO layer is an essential simple model that can help to expand the scope to solve the mysteries.

3.1 Introduction

Emergent phenomena in ferroic materials have attracted significant attention over the past years due to the exciting opportunities to design and facilitate the miniaturization of future electronic devices [43,122–124]. The complex interplay of spin, lattice, orbital, and charge degrees of freedom in ferroic systems gives rise to unique topological textures such as vortices [125,126], skyrmions [127], and domain walls [128–130] that have unique properties that are intriguing for both fundamental scientific studies and potential applications. For example, magnetic topologies have been theoretically studied in-depth and observed experimentally [131,132], and routes to control them have been potentially demonstrated for spintronics [43]. Polar structures that are analogous to these topological magnetic systems have been predicted – such as in ferroelectric nanodots in which spontaneous toroidal moments form [7] – and have led to various theoretical predictions and experiments on low-dimensional ferroelectrics [83] [84] [8] due to the effect of constrained dimensionality.

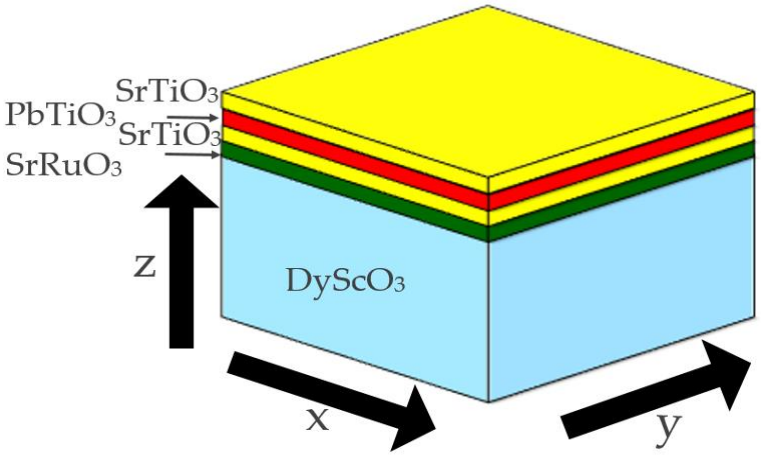

Figure 3.1 Schematic layer stacking of tri-layer system: $(STO)_n/(PTO)_n/(STO)_n$ on the bottom electrode SRO and the DSO substrate

However, the underlying mechanism for the formation and phase transitions of ferroelectric topologies has yet to be systematically studied. For example, the thickness of the layers in PTO/STO superlattices can drive the complex evolution of the depolarization field when coupled with the right substrate strain conditions. This thickness can generate dramatically different phenomena such as improper ferroelectricity for extremely thin PTO/STO superlattices [9] and flux closure domains for thick PTO/STO superlattices [10], which offers a possible route to stabilize polar topological structures. Notably, the understanding of toroidal phase stability is crucial for the design of novel phases such as ferroelectric skyrmion texture and anti-skyrmion texture.

Recent work has demonstrated the possibility of creating toroidal polarization (or vortex) structures in PTO/STO superlattices with careful control over the superlattice periodicity at intermediate thicknesses of PTO. The vortex phase emerges as a direct consequence of the

interplay between the electrostatic energy and the strain energy, which allows for structures with non-uniform polarization textures [11] and coexists with the ferroelectric polarized a_1-a_2 twin domains [12]. These PTO/STO superlattices also exhibit emergent chirality due to the formation of chiral arrays of polar vortices [13]. Prior work in this regard has focused on relatively thick (100 nm) superlattices, thus keeping the useful macroscopic strain constant. However, several questions have emerged from these observations: First, how does the toroidal phase emerge from the ferroelectric phase? Second, is the formation of the toroidal phase a consequence of long-range interactions amongst multiple PTO layers, or are the interactions local to the neighboring layers of STO/PTO/STO? Third, is there any evidence of the antiparallel axial polarizations that result in the 3D chirality? If yes, are there any differences in the chirality?

Before answering these questions, the difficulties of obtaining the limited information of the in-plane polarization distribution of the single vortex were addressed. Simultaneously, the vortex evolution and the property of the vortex phase in the $(PTO)_n/(STO)_n$ superlattices heterostructures were investigated due to the alignment or misalignment of the vortex pairs in multiple confined PTO layers. Thus, the critical solution is to reduce the complexity of the superlattices to one of its simplest forms and probe the evolution of polar structures in symmetric $(PTO)_n/(STO)_n$ trilayer heterostructures where intermediate thicknesses of the layers (*i.e.*, n = 12, 16, 20) are used as depicted in Figure 3.1.

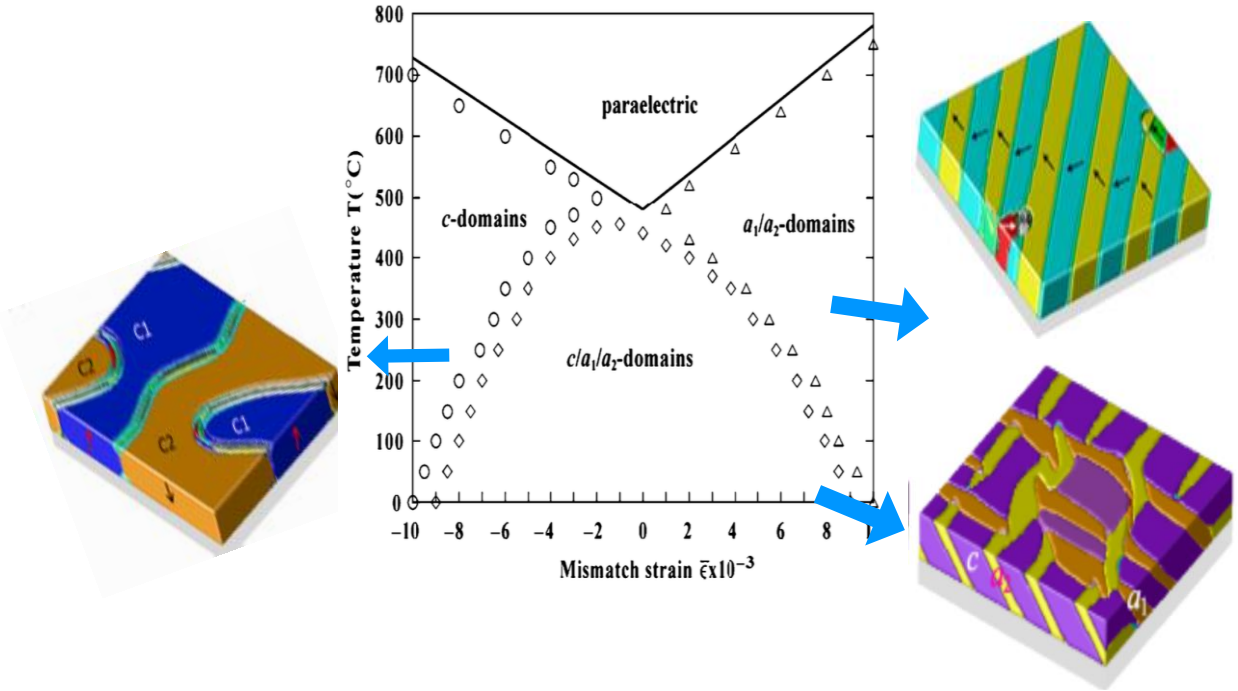

Figure 3.2 Domain stability map of PTO from the phase-field model. Adapted from [24] and [25].

The strategy is similar to the superlattices: utilize the depolarization effect at the interfaces between PTO and STO and introduce ~1% tensile strain from the $DyScO_3$ substrate to manipulate the polar structure in the confined PTO layer. As depicted in Figure 3.2, the domain stability map of PTO calculated from phase-field modeling indicates the phase diagram under different strain conditions to guide understanding of the $(PTO)_n/(STO)_n$ trilayer system. The large tensile strain

would cause PTO to form in-plane a_1-a_2 domains, and the top right 3D polarization mapping demonstrates the in-plane polarized a_1-a_2 domains twin structure with 45° domain walls. The large compressive strain would cause the PTO layer to exhibit out-of-plane *c*-domains, and its polarization mapping indicates the out-of-plane c_1-c_2 domain with meandering boundaries. Thus, the DSO substrate has ~1% tensile strain and should be able to form the mixture of the c/a_1/a_2 domains. Additionally, the depolarization effect demonstrates the suppression of the polarization distribution between the PTO and STO superlattices in previous simulations. These two boundary conditions imply that the polarization rotation can occur in the confined PTO layer and are likely to emerge in the vortex phase due to the continuous rotation polarization field of the vortex phase.

3.2 Phase identification of the vortex state

In previous artificial $(PTO)_n/(STO)_n$ superlattices on the DSO substrate, continuous rotation of polar vortices was found at $n = 10$, and phase-field modeling suggested that this state could be found in the range of an intermediate length scale such as $10 < n < 16$ [11]. Although the trilayer system has similar boundary conditions to the superlattices, the trilayer only possesses one confined PTO layer and would have subtle differences of periodicity (*n*) for emerging the vortex phase compared to the multiple stacking of superlattices. In the prediction of polarization mapping on the $(PTO)_n/(STO)_n$ ($n = 16$) trilayer heterostructures from phase-field modeling depicted in Figure 3.3, continuous rotations of the vortex array exist only in a confined PTO layer and exhibit the zigzag arrangement of the vortex core.

The total energy of this toroidal phase in the trilayer system is competed by elastic energy, electrostatic energy, and gradient energy. The elastic energy comes from the epitaxial PTO/STO layers on DSO substrate that provide the ~ 1% tensile strain for a mixture of the c/a_1/a_2 in-plane and out-of-plane polarizations. The electrostatic energy comes from the polar discontinuity, which occurs at the interface that indicates the $\nabla \cdot P \neq 0$ to influence the polarization distribution. The gradient energy represents the change of direction and magnitude of the polarization, such as the increase of gradient energy in the phase transition of the vortex phase from the ferroelectric a_1-a_2 twin domains. All three energies contribute to the formation of the vortex phase. This prediction is similar to polarization mapping of cross-sectional HR-STEM imaging on the superlattices and can assist to search for the emergence of the vortex phase in the intermediate scale of periodicity, such as $10 < n < 16$. The $(PTO)_n/(STO)_n$ ($n = 12$) trilayer heterostructure was employed in this experiment.

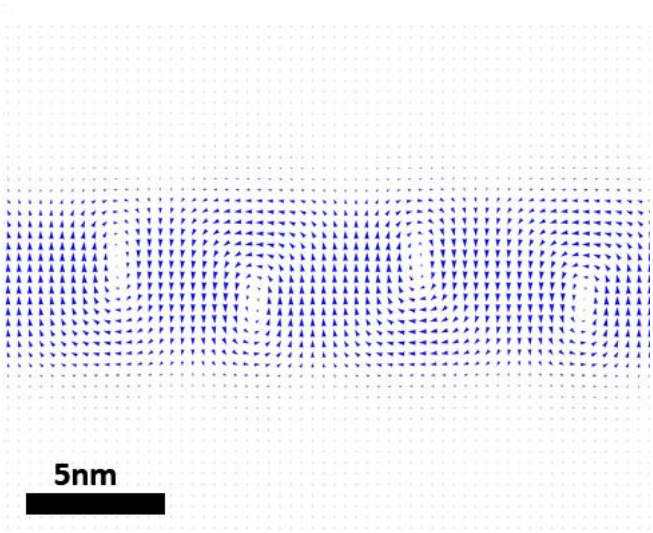

Figure 3.3 Phase-field modeling for a $(PTO)_n/(STO)_n$ (n = 16) trilayer heterostructure on a DSO (110) substrate in the cross-sectional view. This suggests the emergence of the vortex phase only in the confined PTO layer.

The crucial requirement to observe the vortex phase is to get the high quality epitaxial thin film of $(PTO)_n/(STO)_n$ trilayer on top of the SRO buffer layer and the DSO (110) substrate from the fabrication. It is necessary to avoid any defects due to the coupling to the polarization. They can form the nucleation sites for switching and pinning sites for domain-wall motion and are well-known to control the thermodynamic stability of ferroelectric polarization [133]. Besides, defects can obscure our observation, lowering the chance for the system to form the ordering phase. Thus, atomic resolution HR-STEM on $(PTO)_n/(STO)_n$ trilayer (n = 12) is utilized and exhibits the high quality epitaxial thin films with sharp and coherent interfaces with layer uniformity in Figure 3.4, that would give the chance to observe the emergence of vortex phase without interference.

The PTO layer indicates higher contrast than STO layers due to the Z-contrast sensitivity of STEM imaging because Pb is heavier than the Sr atom, and the electron can be detected with a high angle annular dark field (HAADF) detector. Additionally, perfect TEM sample preparation is needed to obtain the right thickness of the flat TEM thin foil. If the TEM thin foil is too thick, dynamical scattering will make the random polarization distribution of the ferroelectric materials the same as the curved TEM thin foil. If the TEM thin foil is too thin, the depolarization field of the ferroelectric materials parallel to the electron beam direction in the TEM will influence the polarization distribution to cancel out the polarization. The next steps are to use DF-TEM in two beam conditions to search for the in-plane and out-of-plane modulations and to use HR-STEM imaging on the zone axis with displacement mapping to search for the vortex phase.

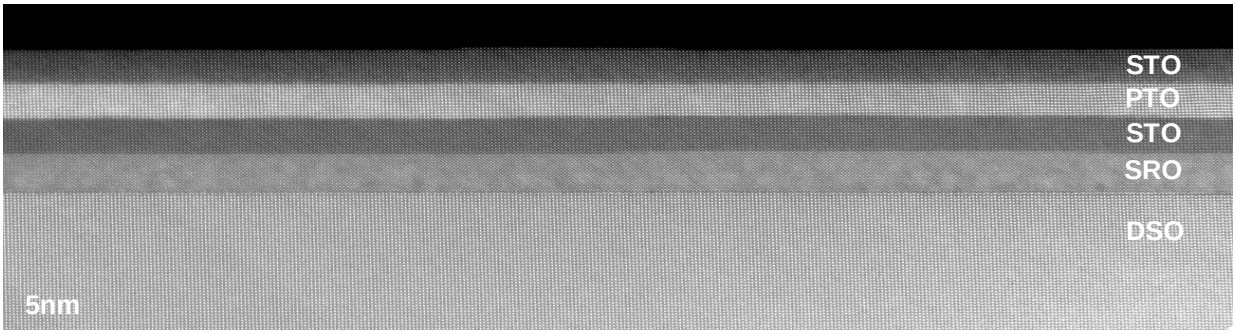

Figure 3.4 HR-STEM imaging indicating the high quality of the epitaxial thin film of $(PTO)_n/(STO)_n$ trilayer (n =12) on top of the SRO buffer layer and the DSO $(110)_o$ substrate.

3.3 Polar vortices array in a confined $PbTiO_3$ layer

After confirming the high quality of the TEM thin foil sample with the right thickness and the periodicity PTO/STO trilayer heterostructure, the local region can be focused on to search for the existence of the toroidal phase in the trilayer heterostructures. By tilting precisely on the zone axis to image the atomic columns, the zoom-in of the atomic-scale STEM image in Figure 3.5 (a) reveals the sharp Z-contrast imaging of the atomic ABO_3 structure of PTO and STO with the distinct interfaces. The local non-centrosymmetry of the atomic columns in the ABO_3 lattice is probed to trace the emergence of a toroidal phase. The result can determine the polarization configuration, which can be extracted using a displacement vector-mapping algorithm that is applied to the cross-sectional atomic resolution STEM images [83]. As a result, the continuous rotation of alternating clockwise (CW) (blue arrows) and counterclockwise (CCW) (red arrows) polar vortices with a spacing of ~10 nm was only revealed in the confined PTO layer depicted in Figure 3.5 (b). The result is opposed to the ferroelectric a_1/a_2 domains that were observed for short-length scales of PTO/STO superlattices [134] and the flux closure domains that were observed for long-length scales PTO/STO superlattices [10]. Furthermore, the vorticity of the toroidal phase can be probed by calculating the curl of polarization ($\vec{\nabla} \times \vec{P}$) that exhibits the non-zero value in the PTO layer and zero value in the two STO layers depicted in Figure 3.5 (c). The core of the vortices indicating the alternating CW and CCW rotation centers can be clearly observed. Thus, the existence of the array of polar vortices is found in a confined PTO layer of $(PTO)_n/(STO)_n$ trilayer heterostructure (n =12) that matches with the prediction of the phase-field modeling.

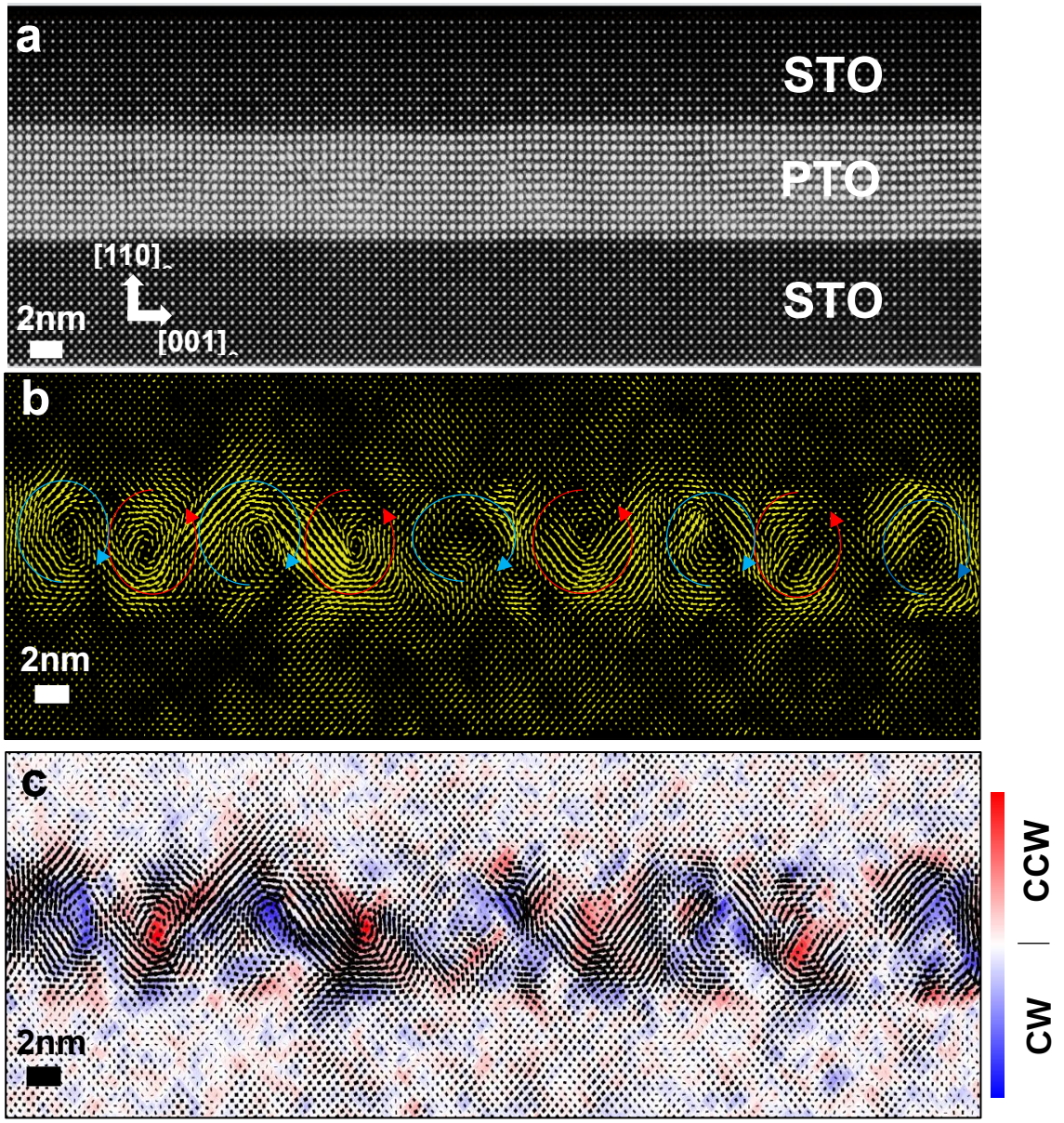

Figure 3.5 Searching for the vortex phase in the confined PTO layer on $(PTO)_n/(STO)_n$ superlattices (n =12) indicates the (a) high-quality HR-STEM imaging, (b) polarization mapping, and (c) curl of polarization overlaying with the polarization mapping.

Additionally, the in-plane and out-of-plane polarization distributions can be extracted from the overall polarization distribution to extract the partial components to form the vortex phase. As depicted in Figure 3.6 (a), the periodic ordering indicates the in-plane polarization distribution toward $[001]_o$. The red triangular structure represents the polarization that is pointing to the right, and the blue triangular structure represents the polarization that is pointing to the left. The quantification of their displacement magnitude is ~38 pm, which is similar to the $(PTO)_n/(STO)_n$ superlattices system. On the other hand, the periodic ordering demonstrates the out-of-plane polarization distribution toward $[110]_o$. The ordering in red represents the polarization that points upward, and the ordering in blue represents the polarization that points downward. These components of periodic modulations are critical components of polar vortices that correspond to the polarization mapping depicted in Figure 3.5 (b).

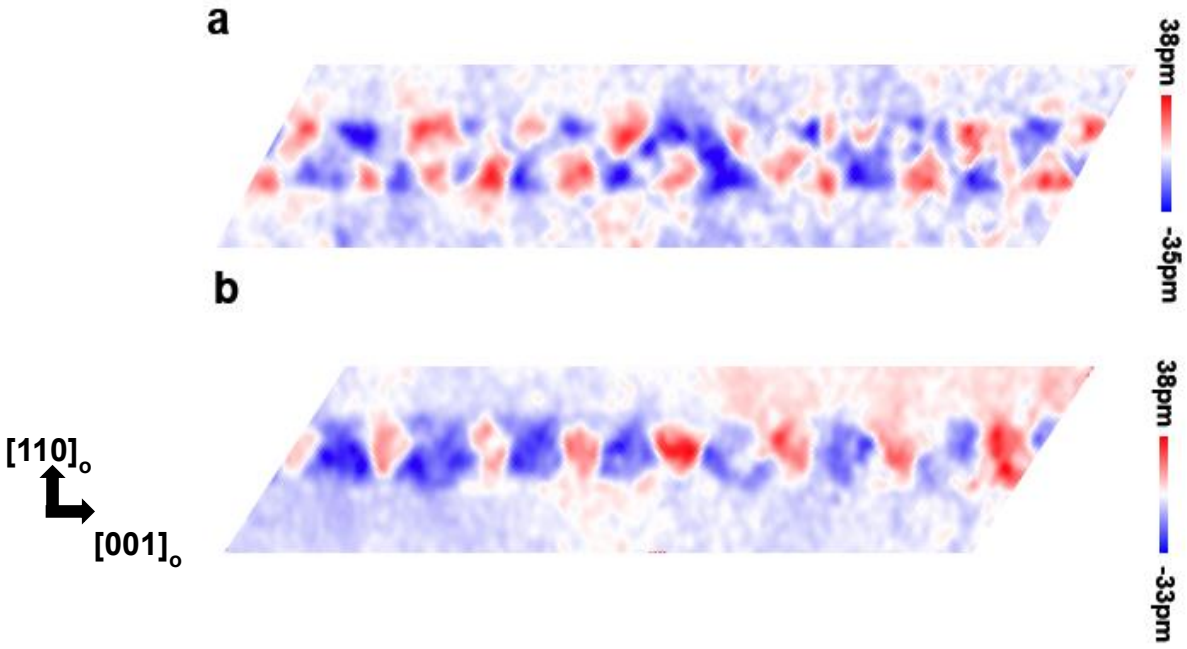

Figure 3.6 The (a) in-plane and (b) out-of-plane polarization distribution that is extracted from the atomic displacement mapping indicates the long-range ordering to form the vortex phase.

3.4 Periodic ordering in a confined $PbTiO_3$ layer

To probe the polar structure of the PTO layer, DF-TEM in two beam conditions was utilized to examine the components of polar vortices. This experiment aimed to measure the non-centrosymmetry of the ferroelectric material. Due to Friedel's law, which means the F(*hkl*) = F(*-h -k-l*), no domain contrast is revealed in a material with inversion symmetry material such as the centrosymmetric STO. The breaking of inversion symmetry and of Friedel's law can reveal the dynamical contrast such as the domain wall in BTO [135] and can be explained by the dynamical

scattering theory for the noncentrosymmetric materials [136]. Furthermore, this kind of dynamical contrast can be influenced by the thickness of the TEM sample. Hence, the thickness of the TEM thin foils is very important for the measurement. Figure 3.7 (a) depicts how the two-beam imaging conditions in DF-TEM on the cross-sectional TEM thin foil reveal the periodic long-range orderings in triangular contrast using the $[00\text{-}2]_o$ g-vector. These orderings only revealed in a confined PTO layer, which is noncentrosymmetric compared to the centrosymmetric STO. The polarization direction of these triangular in-plane modulations points to the $[00\text{-}2]_o$. The out-of-plane two-beam conditions of DF-TEM using the $[\text{-}2\text{-}20]_o$ g-vector are depicted in Figure 3.7 (b) and reveal the periodic long-range ordering in rectangular contrast only in a confined PTO layer. This means that the polarization direction of the ordering points to the $[\text{-}2\text{-}20]_o$. These findings support the atomic polarization mapping analysis that these intensity modulations are vital components of the vortex phase; see Figure 3.6.

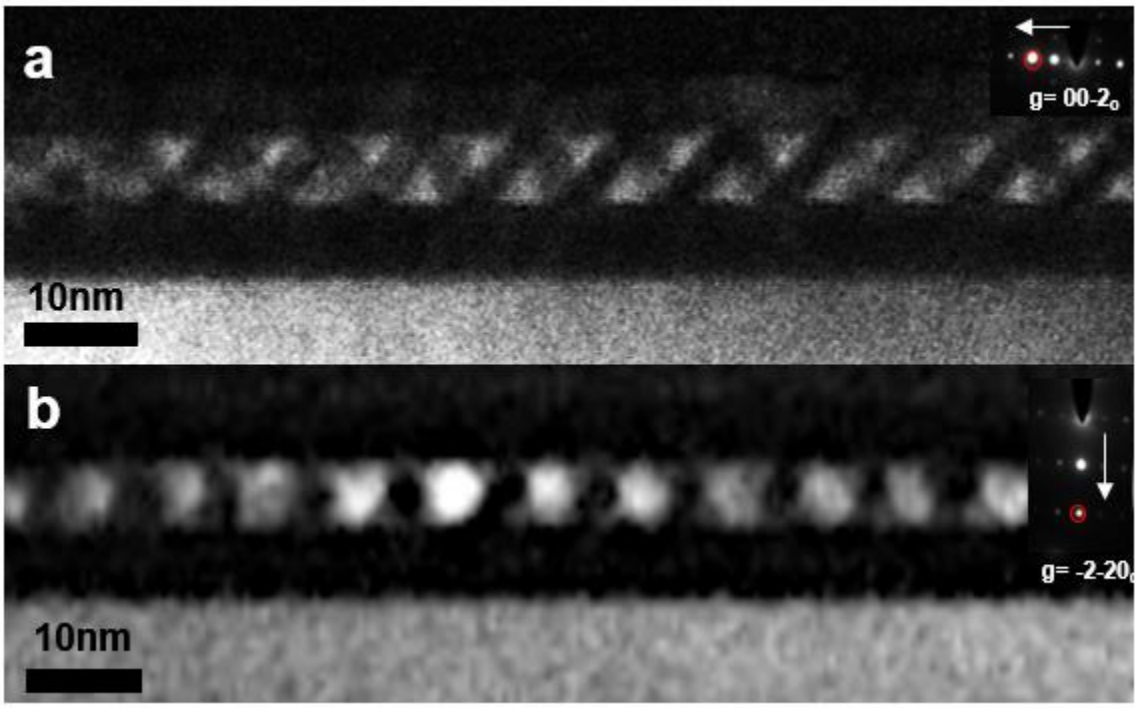

Figure 3.7 The (a) in-plane and (b) out-of-plane polarization distribution extracted from the DF-TEM that indicates the long-range ordering to form the vortex phase.

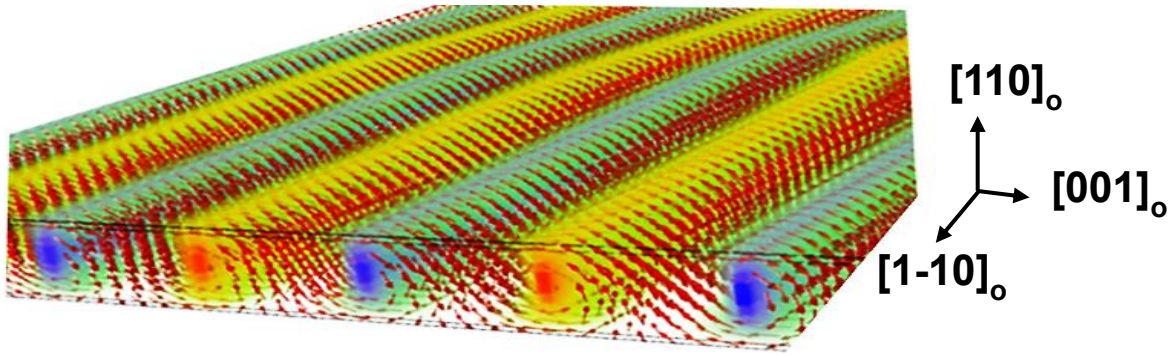

Figure 3.8 The 3D polarization mapping demonstrating the vortex stripes in a confined PTO layer

3.5 Summary

The polar vortices indicate a stripe-like structure when viewed from the top in the $(PTO)_n/(STO)_n$ superlattice system. Figure 3.8 depicts how the 3D polarization mapping that was calculated from the phase-field modeling also suggests the similar result by demonstrating that the vortex stripes lie along the in-plane $[1\text{-}10]_o$. These stripes are found to be stabilized by different contributions from Landau, elastic, electrostatic, and gradient energies. However, because the trilayer system only has one confined PTO layer, it is more straightforward than superlattices in terms of observing the in-plane polarization of the polar vortices. As mentioned earlier, the questions that arise from the polar vortices in a confined PTO layer pertain to the phase transition of the vortex phase and understanding the chirality distribution of the polar vortices. The vortex stripes in a confined PTO layer are the direct solution to these questions regarding the characterization the vortex phase. Based on the observations in this chapter, it can be concluded that even a single confined PTO layer has long-range ordering of polar vortices that are akin to those in superlattices [11], and such trilayer systems provide a simple model system that enables the deep probing of the evolution of this vortex state.

Chapter 4
Phase Stability of Polar Vortices in $PbTiO_3$/ $SrTiO_3$ Heterostructures

After discovering the vortex phase in the trilayer system, this chapter continues to study the phase stability of the vortex phase, including the phase transition and the mechanism entailing how the vortex phase evolves. Compared to the ~100 nm superlattice system with seven confined PTO layers, the trilayer system with only one confined PTO layer is the best candidate for investigating the single vortex itself. Trilayer heterostructures $(STO)_n/(PTO)_n/(STO)_n$ with varying periodicity (n = 10, 16, 20) were deposited on a DSO substrate $(110)_o$. More specifically, this chapter utilizes the trilayer system as a function of the periodicity of the PTO layer in order to understand the phase stability by combining the experimental results and calculations using phase-field modeling. The characterization of polar structures was first imaged by DF-TEM on the planar-view TEM sample—mainly using electrons from the top of the trilayer heterostructures to observe the primary domain structures. The vector mappings of phase-field modeling were utilized to confirm the polar structures from top of the trilayer heterostructures, and the energy calculations helped to understand the critical factors in the trilayer heterostructures. Finally, synchrotron-based XRD provided three-dimensional RSMs for in-depth structural information. Combing all these studies, I confirm the polar structures of these trilayer heterostructures. Furthermore, the mechanism can be realized through use of a series of confined PTO layers from trilayer to superlattices.

.

4.1 Introduction

The phase transition is a seminal research topic in materials science and, furthermore, offers the potential for technological applications because it can dramatically alter the properties of a given material without the addition or deduction of elements. Topological structures often excite various exotic phenomena in physics due to their unique symmetry and interactions. In ferromagnetic materials, the phase transition of topological structures is intriguing because temperature and magnetic field can decide the stable state. To this end, one can consider, for example, skyrmions: MnSi is a helical magnet, and its skyrmions phase can be stabilized near the transition temperature in a limited region when an applied magnetic field is used, as Figure 4.1 (a) illustrates [63]. In the $Fe_{0.5}Co_{0.5}Si$ system, the phase transition of skyrmions and helical states can also be tuned by temperature and magnetic field, as Figure 4.1 (b) and (c) illustrate [27]. Thus, understanding the mechanisms of the phase transition associated with their interactions is an essential task for future device applications.

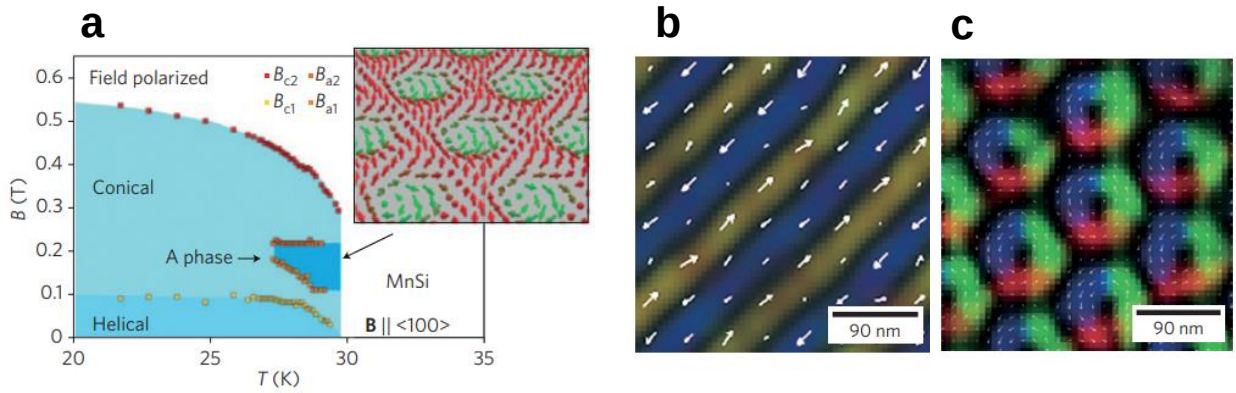

Figure 4.1 (a) The phase diagram of MnSi as a function of temperature and magnetic flux density. The inset shows the schematic view of the triangular crystal of skyrmions. A real-space observation of (b) helical state and (c) skyrmions by Lorentz TEM. Adapted from [26] and [27].

A crystal structure with symmetry plays a crucial role in determining the properties of a given material. Thus, the collective atomic arrangement can be varied during the phase transition of a material and can easily be investigated through macroscopic measurements. However, it is essential to understand the microscopic behavior correlated to atomic structure for future electronic devices. In a recent discovery, polarization vortices with a toroidal order in a spacing of ~10 nm in $(PTO)_n/(STO)_n$ superlattices have engendered tremendous scholarly interest with respect to developing novel polarization topologies as well as exotic functionalities, such as emergent structural chirality. The polar vortex array in the $(PTO)_n/(STO)_n$ superlattices only emerges in the range of an intermediate length scale such as $10 < n < 24$, stabilized by a combination of Landau, elastic, electrostatic, and gradient energies [11]. For the length scale within this range in superlattices, the polar structure would exhibit a tetragonal ferroelectric phase with in-plane polarized a_1/a_2 twin domains coexisting with the polar vortices [12]. The phase competition between uniform and non-uniform polarization modes in superlattices could tip the balance of the

various energy terms in stabilizing novel polarization topologies, and the vortex state could be switched reversibly to the ferroelectric state when an electric field is applied. Furthermore, the calculations of phase coexistence from phase-field modeling in the superlattice system has suggested the existence of antiparallel axial polarizations since the axial electric toroidal moment arises from the ferroelectric phase to the vortex phase along $[100]_{pc}$, as Figure 4.2 illustrates [134]. These experimental and simulation results provide hope for the novel properties of the vortex phase as the 3D chirality texture, not the 2D cycloid textures as we observed in the cross-sectional TEM.

Accordingly, I would like to present the phase stability of the vortex phase by using a microscopic approach down to the nanoscale using the DF-TEM techniques; this is achieved mainly by employing the planar view TEM sample to characterize the features around 10 nm. When DF-TEM is used to observe a function of the periodicity of $(PTO)_n$ /$(STO)_n$ trilayer heterostructures in planar view, novel polarization topologies and traditional a1/a2 twin domains can be observed even subtle changes of the boundary conditions. The phase coexistence and the evolution of the vortex phase indicate that it might eventually be possible to stabilize a single phase of polar vortices, and the phase transition is significant for understanding the nature of the polarization of vortices and for developing the functionalities of their emergent properties.

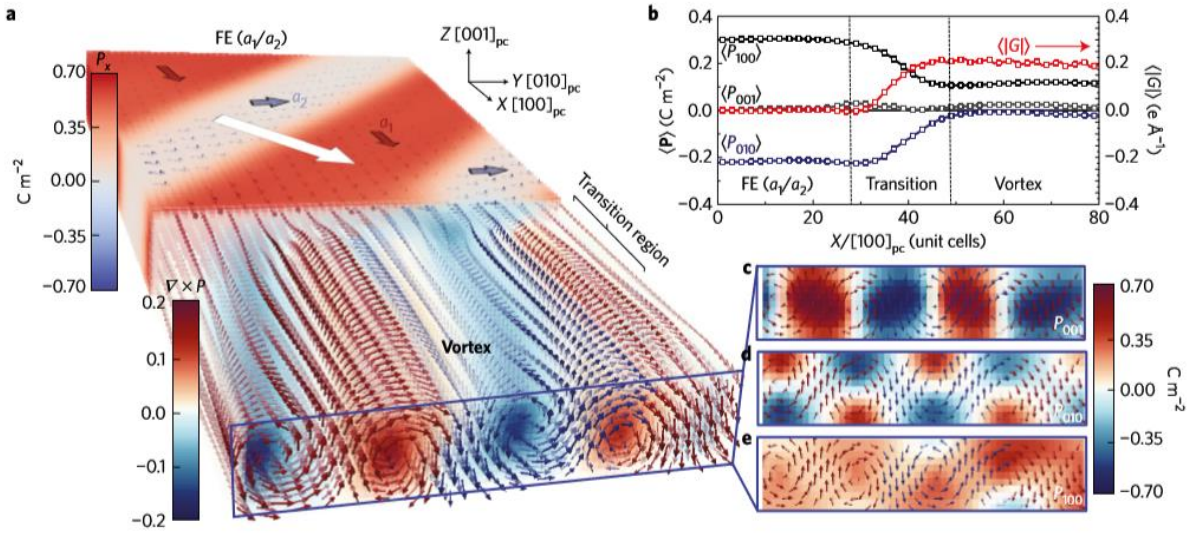

Figure 4.2 A phase-field calculation, showing the phase coexistence in a single PTO layer with the antiparallel polarizations along the axial direction of the vortex phase. Adapted from [12]

4.2 Phase diagram of symmetric trilayer system

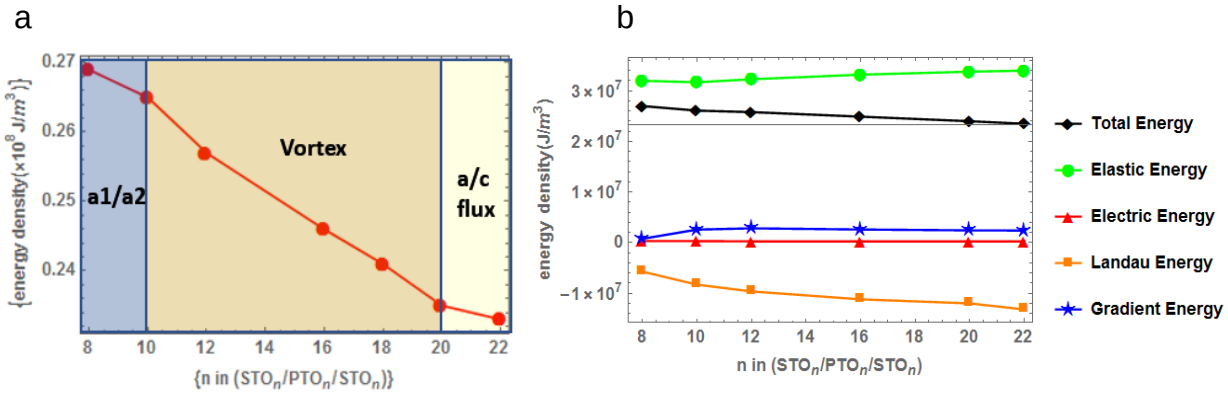

Figure 4.3 Phase diagram of $(PTO)_n/(STO)_n$ trilayer heterostructures on a DSO substrate and of all energy terms versus the periodicity calculated by the phase-field modeling.

The polar structures are strongly influenced by the size of the ferroelectric material. For example, the vortex array only emerges in the range of an intermediate length scale in the PTO/STO superlattices, and this kind of behavior is not observed in bulk ferroelectric materials. The trilayers behave similarly, as the simulation results in Figure 4.3 (a) illustrate, and the phase diagram of PTO/STO trilayer heterostructures calculated by the phase-field modeling suggests three polar structures can be stabilized in the narrow range of a length scale. In a short-period, such as when $n = 8$, which Figure 4.4 (a) illustrates, the polarization distribution exhibits the traditional a_1-a_2 twin structure as the ground state. All polarization components pointing to in-plane directions in thin ferroelectrics mean that the depolarization field is too large and different from bulk ferroelectric materials, in general. Furthermore, from an energy perspective, the total energy density in Figure 4.3 (a) is too high to stabilize the vortex phase. The gradient energy and electrostatic energy are minimized in Figure 4.3 (b) to allow all polarization components to point in-plane directions.

As the periodicity increases toward the intermediate scale range, such as $10 < n < 20$ in trilayer heterostructures, total energy density dramatically drops with the increasing gradient energy in order to stabilize the vortex phase (which I demonstrated in Chapter 3). The top view of polarization distribution, as Figure 4.4 (b) illustrates, shows the emergence of vortex stripes with out-of-plane polarization between CW and CCW rotations of vortices; this means that with the increasing of periodicity, the polarization is no longer purely in-plane, and, moreover, that depolarization is not that high anymore. In long-period trilayer heterostructures, the energy density drops more to stabilize the classic c/a flux-closure domains the same as in the bulk-like ferroelectrics, as in Figure 4.3 (a). With a larger out-of-plane polarization, the polarization distribution shows larger out-of-plane domains near only one direction of the in-plane a-domains when viewing from the top, as in Figure 4.4 (c). Also, due to the growing c- and a-domains, domain

walls can start to form in the system. These calculated results give a greater understanding of trilayer heterostructures as the guide for experimental observation.

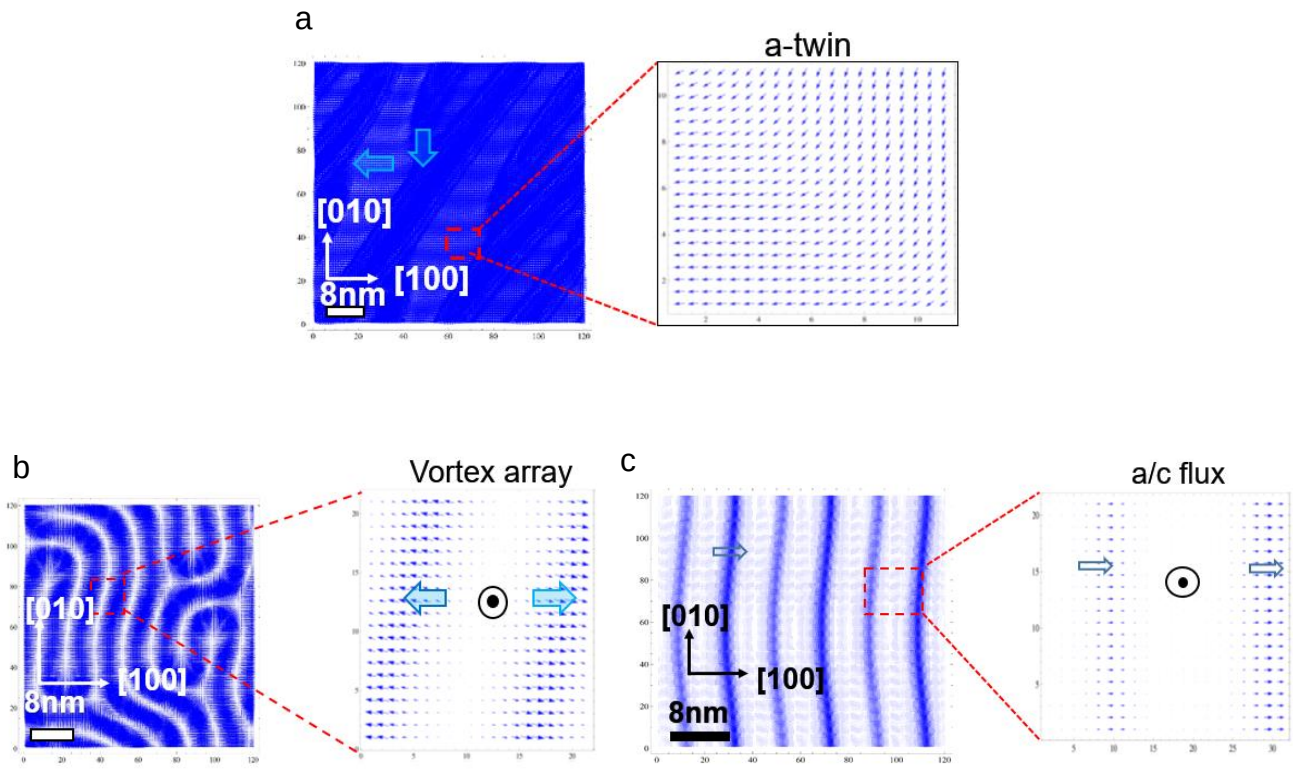

Figure 4.4 The polarization distribution of three phases: (a) a-twin domains, (b) the vortex array, and (c) c/a flux-closure domains.

4.3 Phase coexistence of ferroelectric domains and polar vortices

4.3.1 Thickness dependence of microscopic polar structure

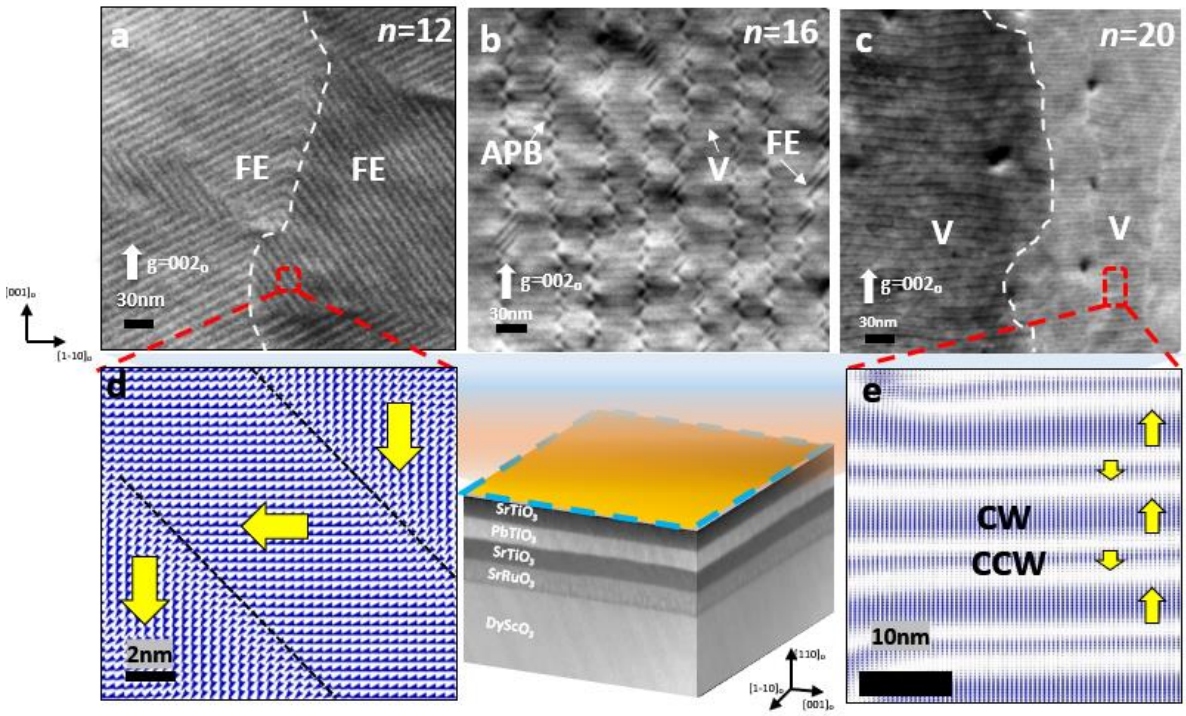

Figure 4.5 The evolution of the vortex state (V) from the ferroelectric state (FE). Diffraction-contrast TEM images on a planar view TEM sample in two-beam conditions from a central schematic $(PTO)_n/(STO)_n$ tri-layer system, (a) n = 12, ferroelectric a_1/a_2 twin domains (FE), (b) n = 16, formation of vortex stripes along $[1\text{-}10]_o$ with anti-phase boundaries and residual a_1/a_2 twin domains, and (c) n = 20, vortex state (V). (d) The prediction of n = 12 by phase-field modeling suggests ferroelectric state a_1/a_2 twin domains, and (e) the prediction of n = 20 suggests CW/CCW rotation of vortex state.

To better assess how the toroidal phase emerges from the ferroelectric phase, the thickness dependence of the layers in the $(PTO)_n/(STO)_n$ trilayers (n = 12, 16, 20) is employed for observation from the top of the heterostructures. Especially, characterization in planar view is the target in this research. In turn, to understand the polarization distribution and phase evolution as a function of periodicity, diffraction-contrast DF-TEM in the planar view using the $[002]_o$ g-vector

and synchrotron-based 3D-RSMs are applied, and the size and direction of the features determine the stability of the state. It should be noted that vortex formation in cross-sectional TEM samples occurs in thinner trilayer heterostructures (as small as $n \approx 4$), as compared to bulk-like measurements observed from previous studies on superlattices [11] [12], and the size effect is the critical factor to examine the phase evolution of the vortex structure. For a trilayer heterostructure ($n = 12$) in Figure 4.5 (a), the overall light/dark diffraction contrast on the left/right sides parallel to the $[002]_o$ g-vector indicates a reversal of net polarization. Inside these broad light and dark regions, the periodic diffraction contrast reveals traditional ferroelectric a_1/a_2 twin domain structures with 45° domain walls and ~10 nm domain width due to the strong depolarization effect that drives all variants parallel to the in-plane directions [134]. In addition, 3D-RSMs of the same heterostructures reveal the absence of ordering in scans about the out-of-plane 220_o-diffraction condition and the presence of ordering in the 45° section of the scan about the 400_o-diffraction condition with calculated spacing ~10 nm, as Figure 4.6 (d) illustrates; this supports the idea that the system contains ferroelectric 45° twin domains with ~10 nm domain width. The phase-field modeling further supports the phenomenon that the polarization distribution shows ferroelectric a_1-a_2 twin structures, as Figure 4.5 (d) illustrates.

When the periodicity of the trilayer heterostructures is increased to $n = 16$, as Figure 4.5 (b) illustrates, most of the ferroelectric a_1/a_2 domains transform to periodic ~10 nm stripes that are aligned along the $[1\text{-}10]_o$; this transformation corresponds to the exact same size and direction of the vortex state that was observed in the cross-sectional view TEM in Figure 3.5. The vortex stripes mainly lie along the $[1\text{-}10]_o$; this is due to the in-plane anisotropy of the $DyScO_3$ substrate [137], which drives the preferred orientation of the vortex formation. Meanwhile, anti-phase boundaries (APBs) between regions of the vortex state can be observed where CW and CCW rotations meet to form an axial domain wall, which is often punctuated with remaining short segments of ferroelectric a_1/a_2 domains, as Figure 4.5 (b) shows. In turn, 3D-RSMs about the on-axis 220_o- and off-axis 400_o-diffraction conditions exhibit ordering modulations, and their size is consistent with the presence of both the vortex state and ferroelectric a_1/a_2 domains. It can, accordingly, be concluded that when $n = 16$ trilayer heterostructures, there is a mixed-phase system with APBs, as Figure 4.6 (b, e) illustrates.

When the periodicity of the trilayer heterostructures is increased to $n = 20$, as Figure 4.5 (c) illustrates, most *a*-domains transform into periodic CW/CCW vortex stripes inside these broad light and dark regions that dominate the entire trilayer system. In the 3D-RSMs, the increasing intensity of on-axis 220_o-diffraction satellite peaks refers a more stable vortex phase as the primary phase, as in Figure 4.6 (c). The decreasing ordering intensity for the off-axis 400_o-diffraction satellite peaks shows that the fraction of a_1/a_2 domains is shrinking as the vortex state becomes more stable, as in Figure 4.6 (f). This is, again, supported by phase-field modeling observing from top of the heterostructures in Figure 4.5 (e). The wide/narrow stripes represent the CW/CCW rotation of vortices due to the asymmetry arrangement of the vortex core. Thus, these direct observations demonstrate the phase evolution of the vortex state from the ferroelectric phase through the mixed-phase system of the vortex and ferroelectric states.

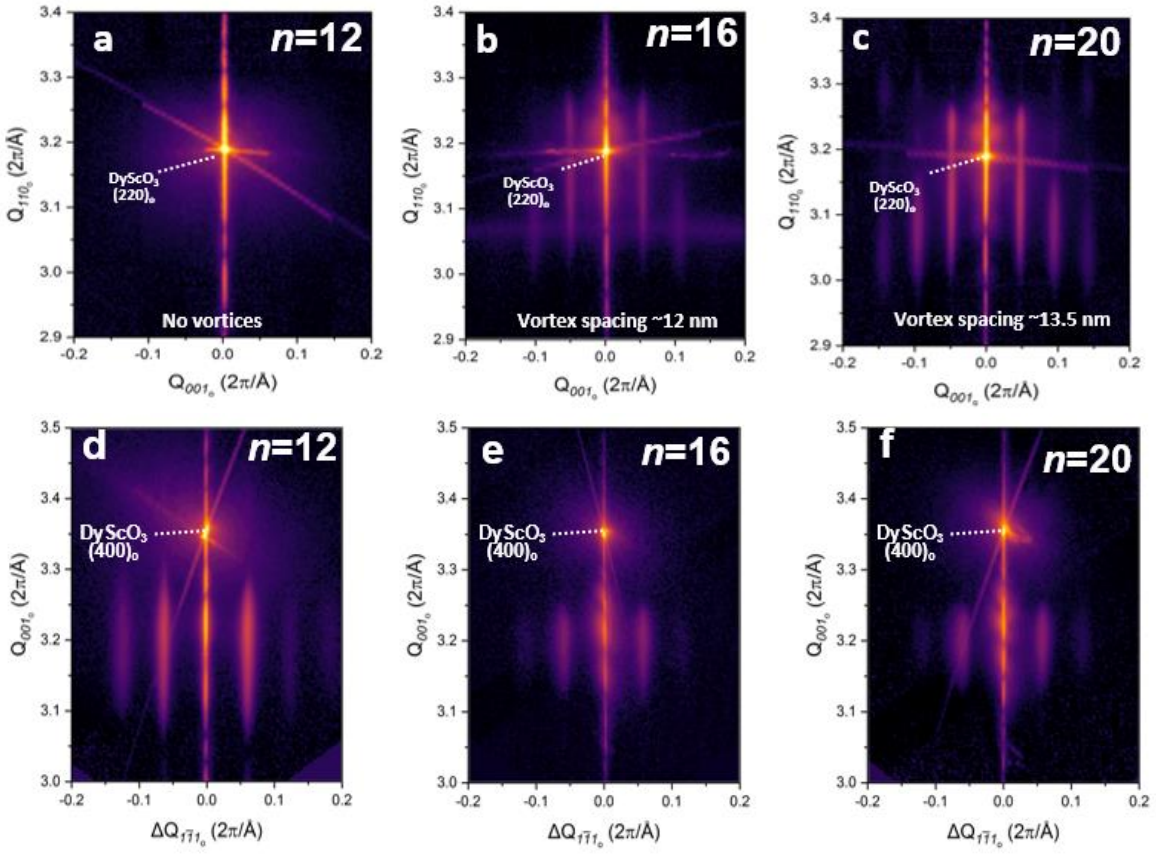

Figure 4.6 The out-of-plane $(220)_o$ ordering information for the 3D-RSM study reveals the following information: (a) when n = 12, there is no vortex state; (b) when n = 16, there is the formation of a vortex state; and (c) when n = 20, there is a vortex state. Reciprocal space maps around $(400)_o$ peak (that is, off-axis)–slice at 45 degrees: (a) when n = 12, there are ferroelectric a_1-a_2 twin structures; (b) when n = 16, there are residual a_1-a_2 twin structures; (c) and when n = 20, there are residual a_1-a_2 twin structures

4.3.2 Thickness dependence of macroscopic polar structure

Besides the microscopic measurements of the vortex evolution, a macroscopic view of the polar structures is vital to this study in understanding the collective behaviors of single unit local polar structures. The macroscopic polarization distribution of the trilayer heterostructures as a function of periodicity is characterized by measuring the response of the in-plane directions: ± $[001]_o$ and ± $[1\text{-}10]_o$ in vector lateral PFM studies at the same region. In general, a sharp conductive probe tip can be used when alternating current bias is applied on the atomic force microscope, and the limited imaging resolution should be approximately 25 nm. Thus, the vortex phase is too small to detect its individual polarizations due to its size (about 10 nm). However, this vortex phase is transverse on the DSO substrate, and macroscopic in-plane polarizations can be detected based on the previous structural characterization of planar view TEM study.

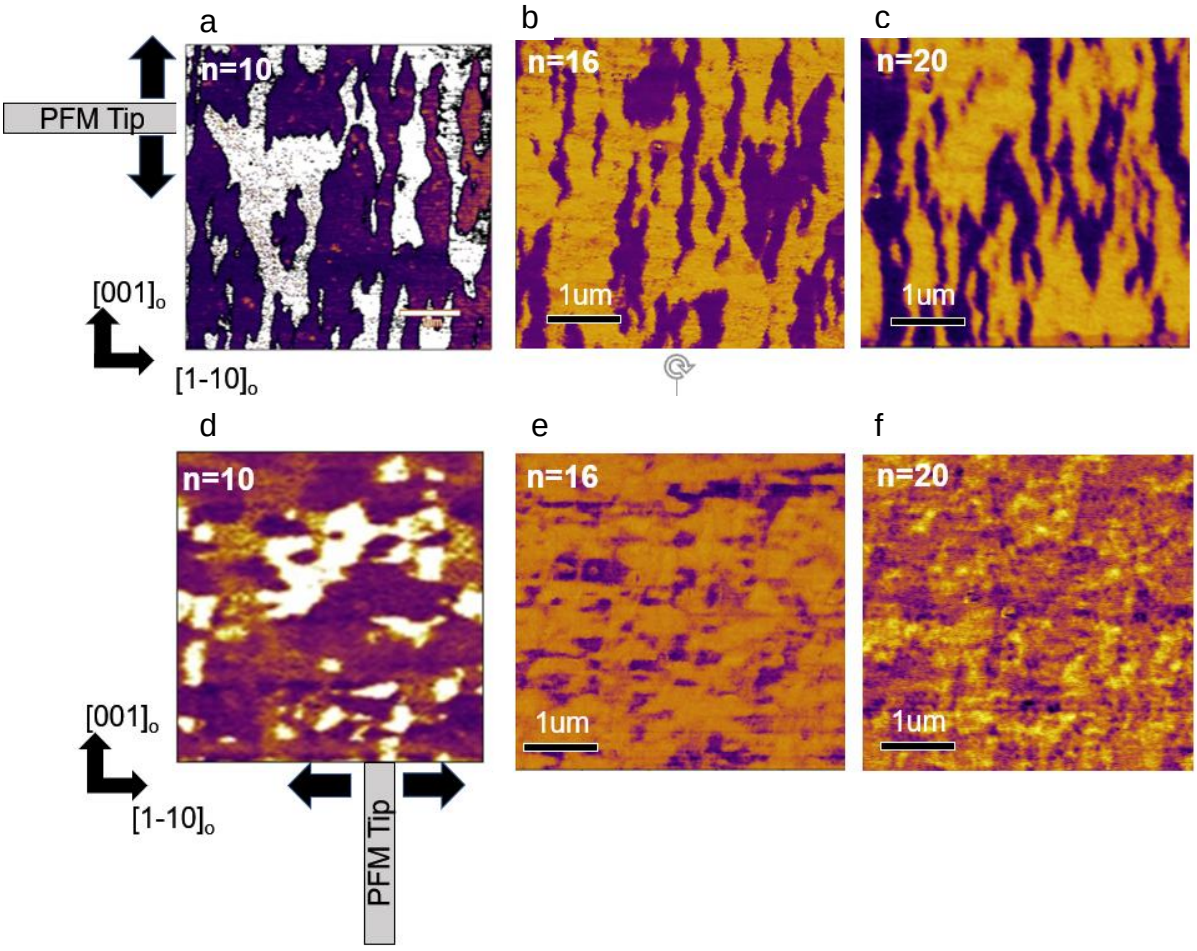

Figure 4.7 The phase contrast of PTO/STO trilayer heterostructures as a function of periodicity, showing superdomain structures with ± $[001]_o$ variants (a–c) and ± $[1–10]_o$ variants (d–f).

In the lateral PFM measurement, the fast scan direction $[1\text{-}10]_o$ is only sensitive to the tip reaction at ± $[001]_o$; this means that the polarization direction shifts to ± $[001]_o$, as Figure 4.7 (a–c) illustrates. The bulky contrast pattern are roughly the same when the periodicity is increased from n = 12 to n = 20. In contrast, the fast scan direction $[001]_o$ is only sensitive at ± $[1\text{-}10]_o$, as Figure 4.7 (d–f) illustrates. The polar structure has dramatic changes from bulky to clumpy pattern when the periodicity is increased from n = 12 to n = 20. Overall, domain walls are not presented here because the size of the features is below the resolution limit. The trilayer heterostructure (n = 10) exhibits the super-domains [89,138], showing the bulky reversal of phase contrast in a micrometer scale along ± $[001]_o$ in Figure 4.7 (a) and the same bulky reversal of phase contrast along ± $[1\text{-}10]_o$ in Figure 4.7 (d). The combination of these two lateral-PFMs is the total polarization toward 45° directions, and this means that the ferroelectric in-plane polarized a_1/a_2

twin domains are consistent with previous simulations calculated by phase-field modeling in Figure 4.5 (d) and by the DF-TEM study in Figure 4.5 (a)

Next, the trilayer heterostructure (n = 16) exhibits a similar reversal bulky phase contrast along ± $[001]_o$, as Figure 4.7 (b) illustrates, but small clumps domains along ± $[1\text{-}10]_o$, as Figure 4.7 (e) shows; this reveals the phase transition from n = 10. The combination of these two lateral-PFM images shows the total polarizations deflecting certain degrees to the ± $[001]_o$. This phenomenon from n = 10 to n = 16 suggests that there is a phase transition from the ferroelectric a_1/a_2 twin domains to the vortex phase according to DF-TEM study in Figure 4.5—in particular, the ferroelectric phase becomes the secondary phase. Due to the $[001]_o$ direction is an easy axis from DSO substrate to influence PTO unit distortion, total in-plane polarization moves to ± $[001]_o$ and the large displacement is along ± $[001]_o$. The $[1\text{-}10]_o$ axis of the DSO substrate has a larger Young's modulus and bending rigidity than the other $[001]_o$ axis [137]. From the superlattice study, the phase coexistence of ferroelectric in-plane polarized a_1/a_2 twin domains and polar vortices create large size of alternating stripes ~ 300 nm along $[001]_o$ [12]. This phenomenon explains why the trilayer with only one confined PTO layer cannot stabilize the two phases in the same ordered large-stripe domains, as in the superlattice, and why the ratio of the ferroelectric a_1/a_2 twin domains is lower than the vortex phase resulting inthe residual irregular a-domains. The physical reason behind this could be the subtle changes of the elastic boundary conditions from trilayer to superlattices—thus maintaining the same DSO substrate.

The trilayer heterostructure (n = 20) exhibits a similar bulky wavy domain phase contrast along ± $[001]_o$, as Figure 4.7 (c) illustrates, and the smaller clumps domains phase contrast along ± $[1\text{-}10]_o$, as Figure 4.7 (f) illustrates. The combination of these two lateral PFM images shows that the total polarization slight deflects to the ± $[001]_o$; this means that the vortex phase becomes the dominating phase, according to previous DF-TEM studies and phase-field modeling. Importantly, the response of the phase contrast along ± $[1\text{-}10]_o$ supports the existence of antiparallel axial polarizations of the vortex phase. Besides the ordering structure of this trilayer heterostructure, n = 20 does not form classic c/a flux-closure domains because the top view of the flux-closure domains in trilayer heterostructures according to the phase field modeling forms a large size of c-domains and a small portion of a-domains. Thus, the single vortex phase and the polarization response of ± $[1\text{-}10]_o$ refer that the antiparallel polarizations of the vortex phase are significant for further studies on the 3D chirality in Chapter 5.

4.4 Origin of the metastable vortex state

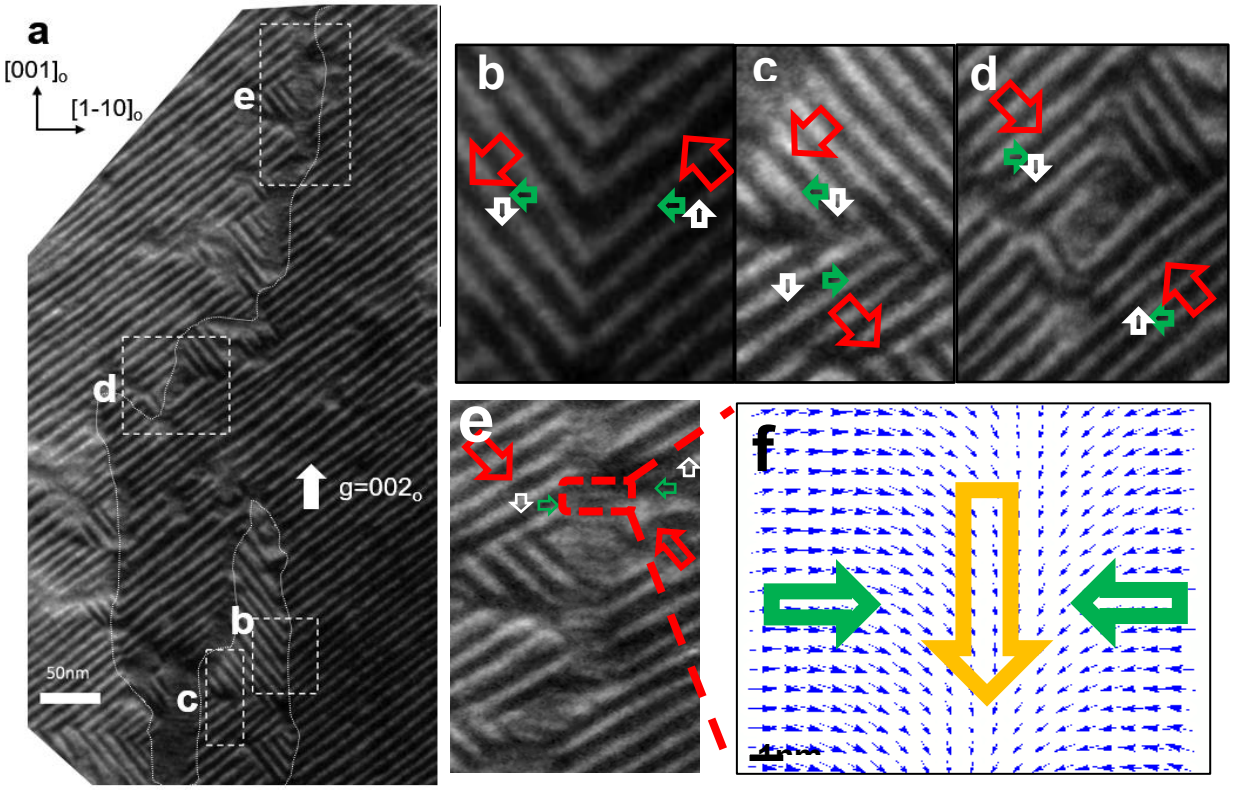

Figure 4.8 The origins of the vortex state from the boundaries of the FE state (n = 12) by diffraction-contrast DF-TEM in two-beam conditions. (a) Ferroelectric a_1/a_2 twin domains with four types of boundaries; (b, c) a head-to-tail boundary; (d) an in-plane vortex domain; and (e) Vortex stripes as the bridge phase between head-to-head domains; (f) Calculation of metastable vortex phase between head-to-head domains by phase-field modeling.

Given that the evolution from the ferroelectric state to the vortex state manifests itself as a function of periodicity, the origin of the vortex state from the ferroelectric state is not clear. In order to explore this metastable vortex state, the plan-view diffraction-contrast DF-TEM for a trilayer heterostructure (n = 12) was studied in this research, particularly at the boundaries of the ferroelectric domains. The large scale of light/dark diffraction contrast represents the net reversal of polarization in the $[002]_o$ g-vector direction, as in Figure 4.8 (a). There are four types of boundaries in order to minimize electrostatic energy and to remain charge neutral. The boundary between the two a_1/a_2 domains is formed by two sets of head-to-tail domains (represented as a white and green pair of arrows in Figure 4.8 (b)). At the boundary, 180° domain walls occur in the light stripes (the white arrows), which results in a 90º rotation of the net polarization (the red arrows). This boundary is again formed by two sets of head-to-tail domains (white to green arrows in Figure 4.8 (c)). In this case, the 180° domain walls occur in the dark stripes (green arrows).

Surprisingly, the head-to-head domains give rise to two types of boundaries in Figure 4.8 (d–e). One type is the typical in-plane vortex domain in Figure 4.8 (d) [139], while the other type entails the vortex stripes along the $[1\text{-}10]_o$ in Figure 4.8 (e)—these are similar to Bloch point domain walls that emerge from two head-to-head spins texture in 1D magnetic nano-stripes [140,141]. Vector mapping extracted from the phase-field modeling shows this metastable state to be the beginning of the vortex stripes (orange arrow pointing along $[001]_o$ that show the lateral polarization component of the vortex) along the $[1\text{-}10]_o$ between two head-to-head domains in Figure 4.8 (f). Hence, the vortex phase emerges as a bridging phase between head-to-head domains in order to help minimize electrostatic energy; subsequently, the entire vortex stripes gradually form so as to stabilize and develop a more extended and straight vortex phase as a function of periodicity in the trilayer heterostructure.

4.5 The emergence of vortex state as a function of repeating trilayer to superlattices

To further clarify the effect of long-range interactions among multiple PTO layers on the formation of the toroidal phase, this research investigated the polarization distribution while varying the number of confined PTO layers from 1 to 7 (that is, changing from trilayer to superlattice heterostructures). Notably, the *a*-domain phase was chosen as a starting point for the trilayer (n = 12) so as to explore the underlying mechanism of vortex formation when the number of confined PTO layers is increased. The low magnification, dark-field TEM images that use the $[002]_o$ g-vector in Figure 4.9 (a–d) exhibit mostly bulky stripes with light/dark diffraction contrast; this indicates the reversal of net polarization pointing $\pm$ $[002]_o$, as Figure 4.7 (a) illustrates. To gain more insights into this phenomenon, high-magnification images of local stripes were used to explore the local phase distribution, which is represented in Figure 4.10 (a–d). Under the bulky non-uniform light/dark diffraction contrast in Figure 4.9 (a), ferroelectric a_1/a_2 twin domains exist as the main phase in Figure 4.10 (a). When the stacking is increased to 3 PTO layers in Figure 4.9 (b), the non-uniform light/dark diffraction contrast becomes more stripy. This phenomenon implies that more confined PTO layers can adjust the arrangement of the polar structures between PTO layers and ferroelectric a_1/a_2 twin domains are still the primary phase in Figure 4.10 (b).

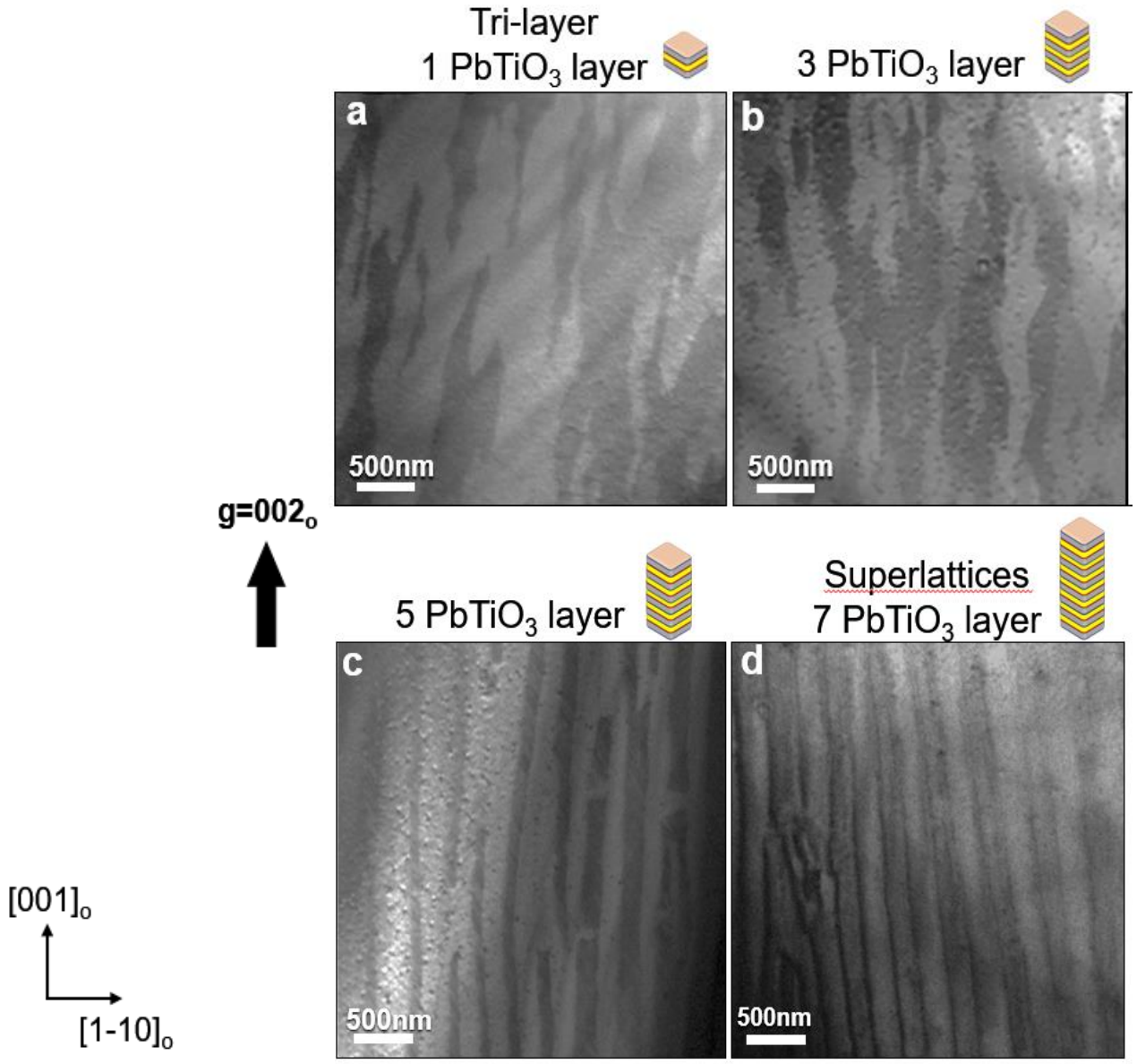

Figure 4.9 The formation of the toroidal phase from the PTO/STO tri-layer (n = 12) to PTO/STO superlattices (n = 12), observed by diffraction contrast DF-TEM in low and high magnifications. Low-magnification images (a–d) represent 1, 3, 5, and 7 confined PTO layers.

Furthermore, as the PTO layers is increased to 5 in Figure 4.9 (c), the light/dark diffraction contrast changes to ordered stripes separately without continuity, and this implies the enhancement of the alignment of polar structures and phase separation. Remarkably, between these ordered stripes, the local microstructures show the emergence of vortex stripes along $[1\text{-}10]_o$ adjacent to the ferroelectric a_1/a_2 twin domains in Figure 4.10 (c), and this suggests that long-range interactions among multiple PTO layers can modulate the polarization distribution and can stabilize the vortex phase. Finally, the light/dark diffraction contrast shows the ordered, straight,

and continuous stripes in the superlattices within 7 confined PTO layers in Figure 4.9 (d), and this suggests more PTO stacking layers stabilizes the phase coexistence of the vortex phase and the ferroelectric phase [12]. The polar structure in more stacking layers of heterostructures behaves the bulk-like ferroelectric domains in Figure 4.10 (d). Hence, my observation of phase evolution as a function of PTO layers shows not only the polarization rearrangement but also the emergence of the vortex phase, and this indicates that long-range interactions among multiple PTO layers can play an essential role in influencing the vortex stability.

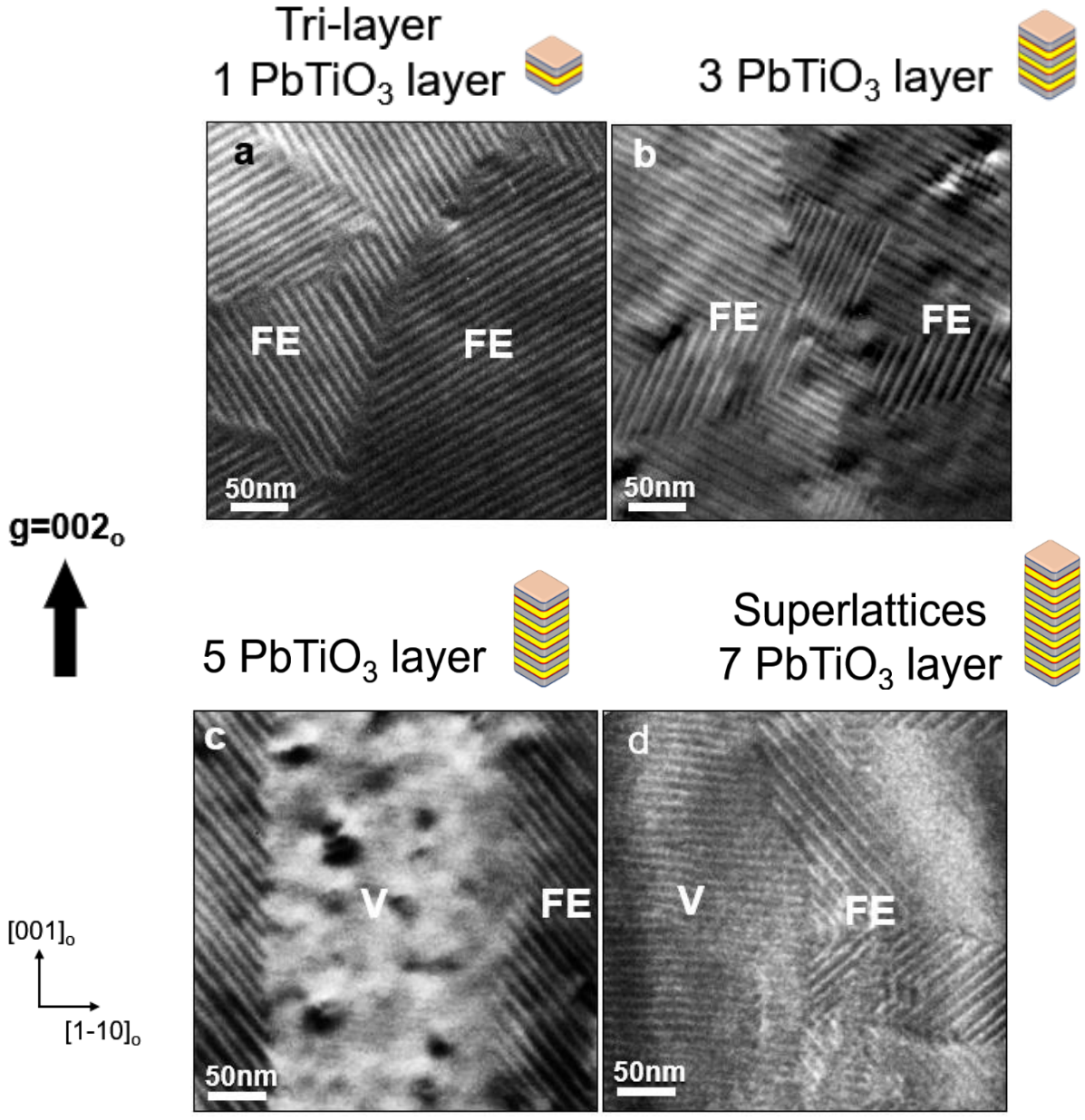

Figure 4.10 High-magnification images (a–d) from trilayer to superlattice exhibit the evolution from full FE states to the phase coexistence of FE and V states.

4.6 The role of elastic boundary condition

Phase-field simulations were performed to provide a better understanding of the film-thickness dependent polar structure transition. It was revealed that a higher fraction of the vortex phase is obtained in thicker films (as the transition from one to seven confined PTO layers), in suitable agreement with the experimental observations. Meanwhile, the average total energy density of the system in Figure 4.11 (a) drops along with this transition, and this indicates that the system is lower in energy (more stable) with more PTO/STO layers. The stabilization is mainly attributed to the decrease of the average elastic-energy density since the vortex phase has a higher ratio of elastically favorable out-of-plane polarization in Figure 4.11 (b). In contrast, the electrostatic (electric) and gradient energy densities increase due to the *a*-domain twin to polar vortex transition, which has also been demonstrated previously [11] [134]. A subtle decrease of the Landau-energy density is also shown, due to the relaxation of the polarization towards thermodynamic equilibrium. From an energetic point of view, the film-thickness-driven phase transition (with the PTO/STO ratio kept constant) is a result of the competition between the individual energies—elastic, electric, Landau, and gradient. The increasing layer stacking leads to a higher order of elastic relaxation, which counterbalances the energy penalty of a higher gradient energy density that arises from a complex polar texture and higher electric energy with increased out-of-plane polarization. Hence, these findings reveal that the formation of the vortex state can be excited by increasing the number of confined PTO layers, and this implies the importance of long-range elastic interaction among the PTO layers.

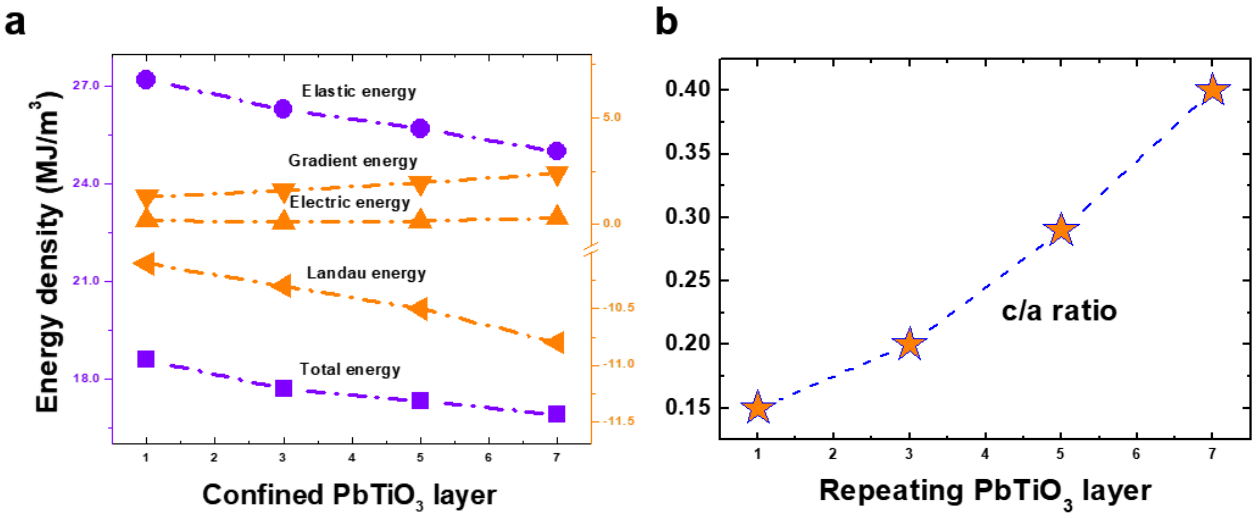

Figure 4.11 A film-thickness-dependent polar structure transition for the PTO/STO tri-layer (n = 12) to PTO/STO superlattices (n = 12), calculated by phase-field simulation. (a) Energy density diagrams; (b) lattice constant c/a ratio.

4.7 Summary

To summarize, by utilizing the thickness dependence of the symmetric trilayer structure, one can directly observe the polarization distribution evolving from a ferroelectric state to a phase coexistence of ferroelectric and vortex phases. Notably, the origin of the vortex state is introduced by head-to-head domains between ferroelectric phases at the beginning of the phase evolution. Ultimately, tipping the energy balance of the system by using elastic energy from the long-range interactions in the PTO/STO system can be an essential knob to excite the vortex state. These studies should contribute to further understanding of novel polarization topologies and provide possible routes to design polarization topologies that enable the development of high-density memory devices.

Chapter 5
The antiparallel axial polarization of polar vortices

From previous studies, lateral polarization investigated by atomic resolution STEM with atomic displacement mapping represents the clockwise or counterclockwise rotations of vortex polarization distribution in the superlattice heterostructures. However, the investigation of the antiparallel axial polarization of polar vortices has been prevented due to the multilayers of polar vortices in the PTO layers that overlap when they are observed from the top of the superlattices. Antiparallel axial polarization was mainly investigated in Chapter 5 by atomic resolution STEM imaging with displacement mapping, diffraction-contrast TEM with two-beam conditions and weak-beam conditions, and simulations calculated by phase-field modeling. Notably, the planar-view TEM sample of the $(PTO)_n/(STO)_n$ trilayer heterostructures on the DSO substrate was employed. Through use of the atomic resolution STEM to focus on the zone axis to get sharp atomic columns, the zone axis of the PTO was selected but not the DSO substrate. If the zone axis of the DSO substrate were selected, the ABO_3 perovskite of PTO would not be revealed. This is because, in the planar TEM sample, the DSO substrate still maintained a large portion of sample volume compared to the thin film, and thus the intensity of PTO is extremely weak. Furthermore, due to the 87.2° alpha-angle, the zone axis of the PTO was a little bit away from the DSO zone. Thus, the zone axis of the PTO was crucial to get the high-quality atomic columns on this planar view TEM sample for displacement mapping. Hence, Chapter 5 focuses on why I use trilayer heterostructures and how to measure the axial polarizations of polar vortices. Furthermore, the result is meaningful for polar vortices having 3D chirality.

5.1 Introduction

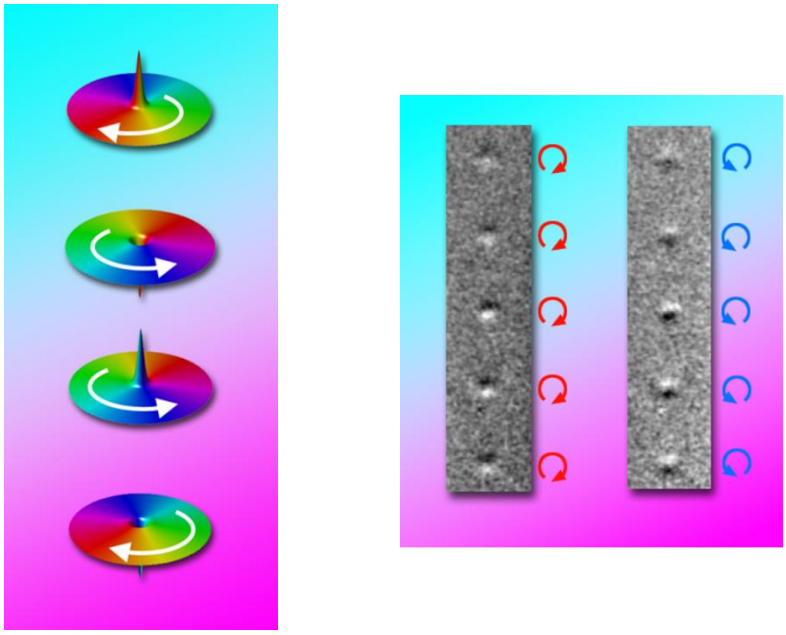

Figure 5.1 (a) A schematic illustration of four orientations of circularity and polarity in magnetic vortices. (b) The magnetic transmission soft X-ray microscope shows the reversal of spin circularity in magnetic vortices in a row of nanodisks through the application of a pulsed magnetic field. Adapted from [28]

In magnetic materials, the theory of topological defects such as helical magnetic structures that are correlated to the phase transition and their properties have been studied as far back as the 1980s [142]. Notably, the characterization of the topological defects and the science behind their core have attracted fundamental research for decades due to their valuable potential applications to information technologies. For the skyrmions/vortex structure, for example, studies have demonstrated the reversal of the magnetic vortex core through an applied electric field to switch its out-of-plane core polarization [59], the polarity switching on chiral magnetic nanodisks [143], and the control of four orientations of circularity and polarity states for multi-bit storage systems [28]. Thus, circularity and polarity are the two vital components to characterize the property of the topological defects, such as the handedness and the sign of the D-M interactions. For the magnetic materials, the circularity is defined as the rotational components, either CW or CCW of in-plane magnetizations, while the polarity is defined as the out-of-plane magnetization pointing up or down at the core. Subsequently, the ferroelectric material is analogous to the ferromagnetic material but lacks the spin degree of freedom. The ferroelectric vortex structure has been theoretically studied from 2004 [7] and has been discovered recently [11]. The critical task from the beginning of the ferroelectric vortex structures is the comprehensive understanding of the polarization distribution of the vortex structure; in particular, the concept of three dimensional distribution is similar to circularity or polarity, which are the two essential components of magnetic topological defects.

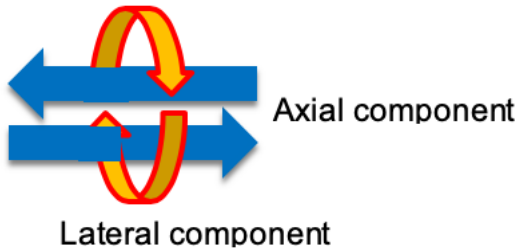

Figure 5.2 Schematic graph of lateral and axial polarizations of a vortex structure

From previous experimental results of superlattices, a significant surprising discovery is that resonant soft X-ray diffraction can measure the emergent chirality in the polar vortices of $PbTiO_3/SrTiO_3$ superlattice heterostructures [13]. However, since 2D cycloid and 3D helical topological defects have significantly different phenomena associated with their properties, a critical problem is the existence of antiparallel axial polarizations of polar vortices that reveal helical rotations of polarization. The schematic graph is shown in Figure 5.2. The lateral polarization of the vortex phase has been well studied in superlattices and trilayer heterostructures as the CW or CCW rotation of the vortex phase, but axial polarization is not easy to detect in superlattices. This axial component has been undetectable in XRD experiments, which could be a result of the extremely weak diffraction from this axial component, and it also might imply the weak magnitude of this axial component. If the axial polarization is aligned in all the vortices, it would not have a signature in the XRD measurement. The critical observation here entails the polarization distribution of the polar vortices, especially in the axial component. The transverse components are well known by cross-sectional HR-TEM [11,144], but the similar characterization of the axial component is hampered by non-uniform structure if it projects through a non-axial direction. The problem includes observing multiple overlapping vortices in the superlattice heterostructures, and for directions normal to the substrate, low symmetry $DyScO_3$ which includes its large A-site and oxygen rotation anti-ferrodistortive structure.

To overcome these problems, I have studied only one layer of $PbTiO_3$ that shows polar vortices in the trilayer heterostructures: $(SrTiO_3)_n/(PbTiO_3)_n/ (SrTiO_3)_n$ [144] in order to discern the polarization distribution in planar view. Thus, as I discussed in Chapter 4, the single vortex phase in a trilayer heterostructure (n = 20) could be the best candidate for detecting the axial component without any interference. The characterizations of polarization distribution and structure show the preferred orientation of vortex structure, and this makes $[001]_o$ the large displacement with CW or CCW rotation of the vortex phase due to the easy axis $[001]_o$ of the DSO substrate. In this chapter, the structural characterization through use of DF-TEM and HR-STEM with atomic displacement mapping can be used to study the antiparallel polarizations of the vortex phase along $[1\text{-}10]_o$—particularly, the unknown nature of the polarization in the axial direction. The studies of phase-field modeling and first-principles simulations predict a polarization component along the toroidal

axis of the vortices, which would be exciting for optical devices with the potential for electrically switchable chirality.

5.2 Diffraction contrast of polar vortices

While axial polarizations of polar vortices in superlattices have not been able to be detected in high-resolution XRD measurements, the $(PTO)_n/(STO)_n$ trilayer heterostructure (n = 16) is employed and uses a similar concept to search for ordered modulations on the zone axis in the electron diffraction; this can help to determine the possible polar orientations of domain configurations [145,146]. In Figure 5.3 (a), the diffraction contrast of the zone axis shows the vortex array along $[1\text{-}10]_o$ with the spacing of ~10 nm. The diffraction pattern shows the higher order diffraction spot 300_{pc} with satellites along $[001]_o$; this means that ordered modulations have the same polar orientations as the lateral polarizations of polar vortices. Interestingly, the diffraction spot 030_{pc} shows faint satellites along $[001]_o$; this indicates that the weak modulations have the polar orientations pointing along $\pm[1\text{-}10]_o$—which is expected for the antiparallel axial polarizations in CW and CCW polar vortices. In contrast, through the scrutiny of a batch of planar-view TEM samples, another direction of polar vortices with boundaries along $[001]_o$ can be created, but the diffraction contrast is extremely weak, as Figure 5.3 (b) illustrates. The diffraction spots, 300_{pc} and 030_{pc}, reveal no modulations, and this means that there are no polarized features or that they are too weak to detect. However, although there is the intriguing signal on the axial polarizations, the diffraction pattern on the zone axis has too many multiple scatterings, and more pieces of evidence are needed.

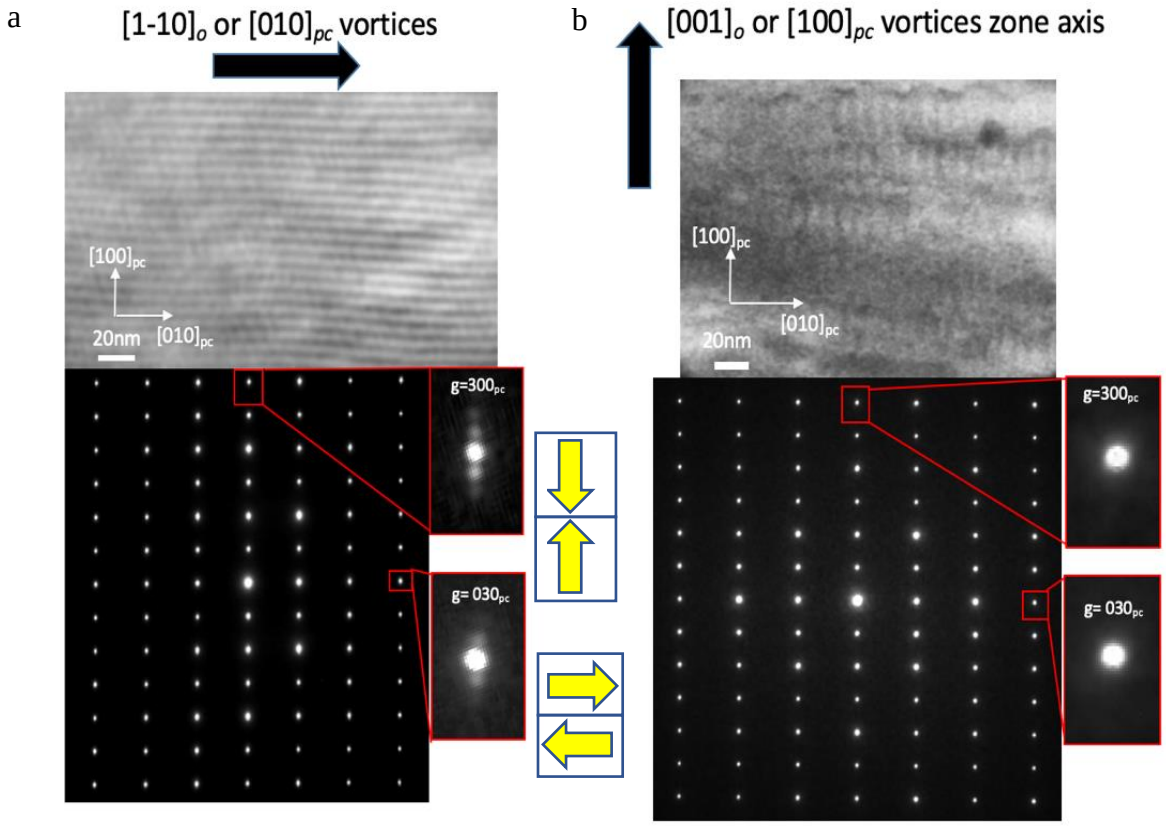

Figure 5.3 Searching for the axial polarizations using electron diffraction. (a) Polar vortices along $[1\text{-}10]_o$ and (b) polar vortices along $[001]_o$.

Another method is to use diffraction-contrast DF-TEM to search for the axial polarizations of polar vortices. Tilting the planar TEM sample far from the zone axis to make the two-beam conditions can avoid multiple scattering and can obtain Bragg conditions; as Figure 5.4 (a) shows, the schematic two-beam conditions of electron diffraction circle the positions of the +g vector (red) and the -g vector (blue). Their corresponding diffraction contrast images are (b) and (c). In (b) and (c), the polar structures present the polar vortices with residual a-domains in the $(PTO)_n/(STO)_n$ trilayer heterostructure (n = 16). It is obvious that diffraction contrast imaging of the +g vector is larger than the -g vector and that (d) is the difference of diffraction contrast (b) and (c). The residual diffraction contrast in (d) suggests an intensity modulation that matches the periodicity and orientation of the vortices. Subsequently, the line profile on the diffraction contrast images of +g and -g vectors in (e), the difference graph shows the intensity modulation. However, because the modulation does not entirely reverse the sign for +g and -g, it is hard to claim a non-centrosymmetric contrast is responsible for this modulation.

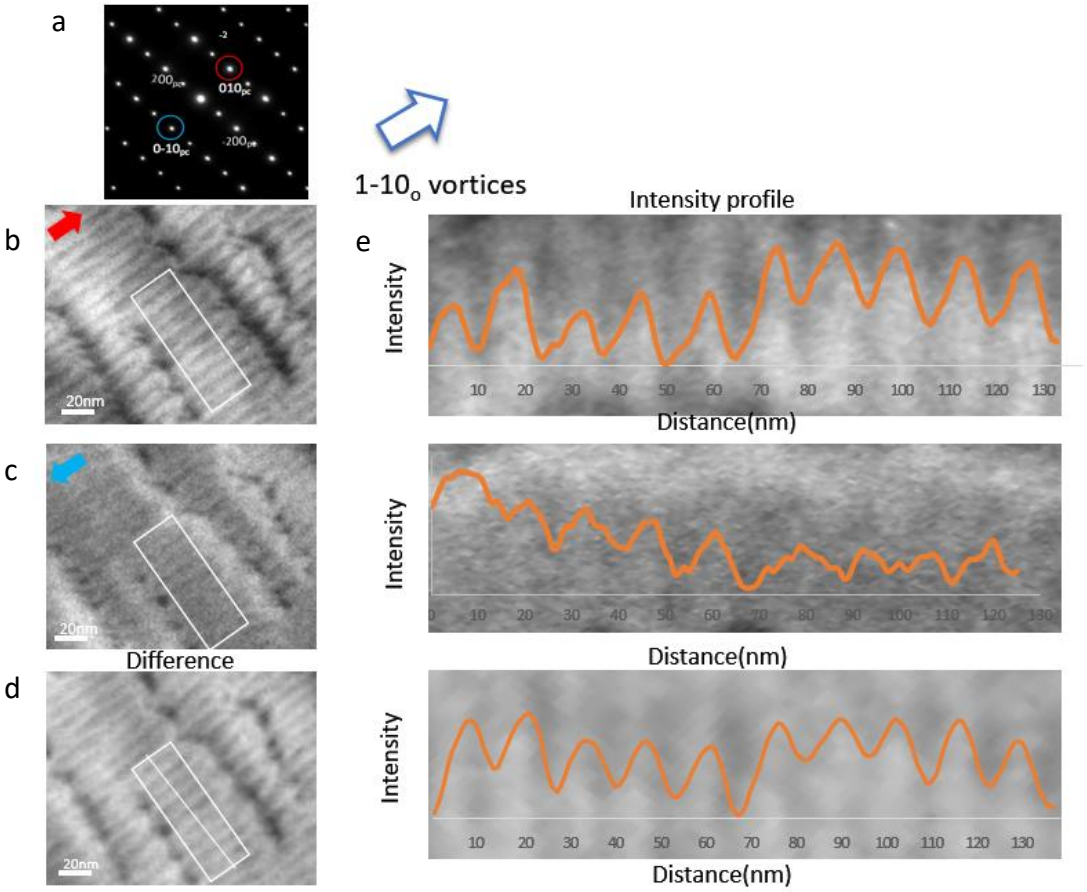

Figure 5.4 Searching for the axial polarization features of polar vortices along $[1\text{-}10]_o$ in electron diffraction and diffraction contrast; (a) Schematic two-beam conditions of electron diffraction. The red circle represents the position of the objective aperture in 010_{pc}, and the diffraction contrast is in (b). The blue circle represents the position of the objective aperture in $0\text{-}10_{pc,}$ and the diffraction contrast is in (c). (d) is the difference between (b) and (c). (e) the line profile of white box in (b), (c), and (d)

5.3 Atomic polar displacement mapping of phase coexistence and single vortex phase

After I tried conventional TEM techniques, HR-STEM imaging was used, which is another robust zone axis technique that can measure the polarization distribution of polar vortices. At first, the $(PTO)_n/(STO)_n$ trilayer heterostructure (n = 12) was found to possess the emerging vortex phase evolving from the ferroelectric a_1-a_2 twin domains. It would be intriguing, moreover, to see if the axial polarizations are coming from the ferroelectric a_1-a_2 twin domains due to their large in-plane polarizations. As Figure 5.5 (a) shows, a low magnification of the large area is probed, and the inset figure shows the atomic resolution of the ABO_3 structure so as to validate the uniform and high-quality data without universal tilting. After the atomic displacement is extracted from the spherical Gaussian fitting, the polarization mapping with angle map indication, as shown in Figure 5.5 (b), provides abundant in-plane polarization information. The polar vortices are along $[1\text{-}10]_o$ (red is the CW rotation of vortices, while light blue is the CCW rotation of vortices) in a spacing of ~10 nm, and the ferroelectric a_1-a_2 twin domains with 45° domain walls are also present in a spacing of ~10 nm. The boundary between two polar vortices shows the black color which is ~0 degree; this means that the polar vectors are pointing along the direction and penetrating in or out of the page. The winding boundaries of the vortices indicate that the vortex phase is not stable enough. Since polar vortices are evolved from the ferroelectric a_1-a_2 twin domains and connected, it would be valuable if applying electric field control on this metastable state could potentially be used for the switching of the phases.

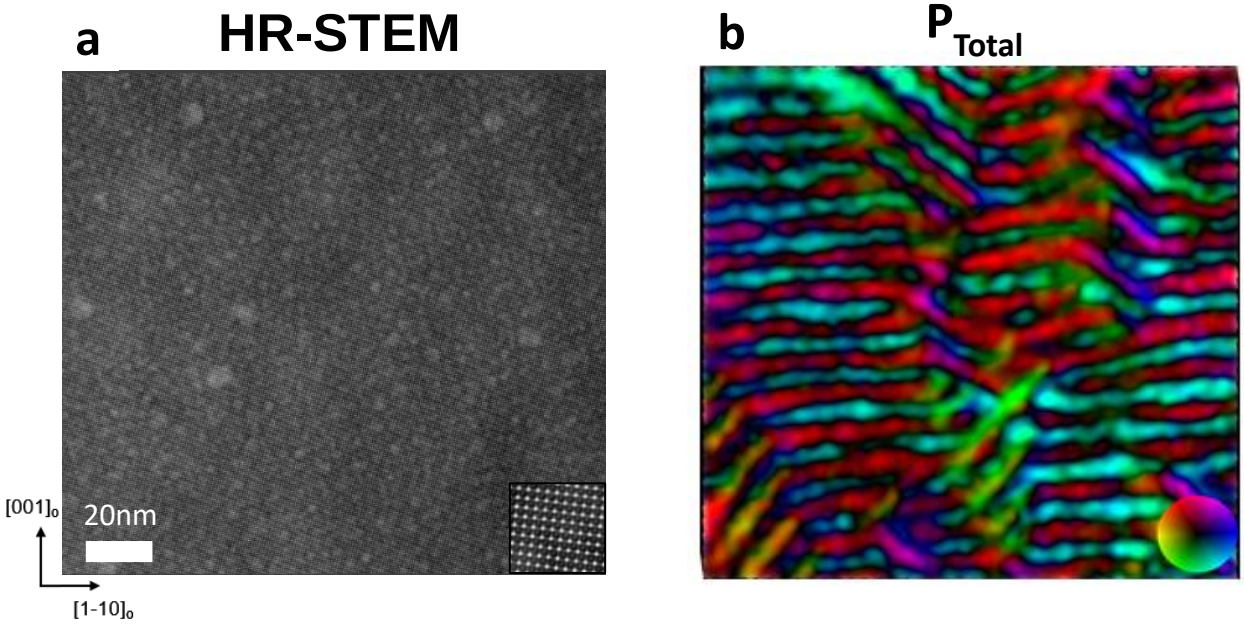

Figure 5.5 Using HR-STEM mode on $(PTO)_n/(STO)_n$ trilayer heterostructure (n = 12) to probe atomic columns in (a) and to calculate the atomic displacement for polar mapping in (b).

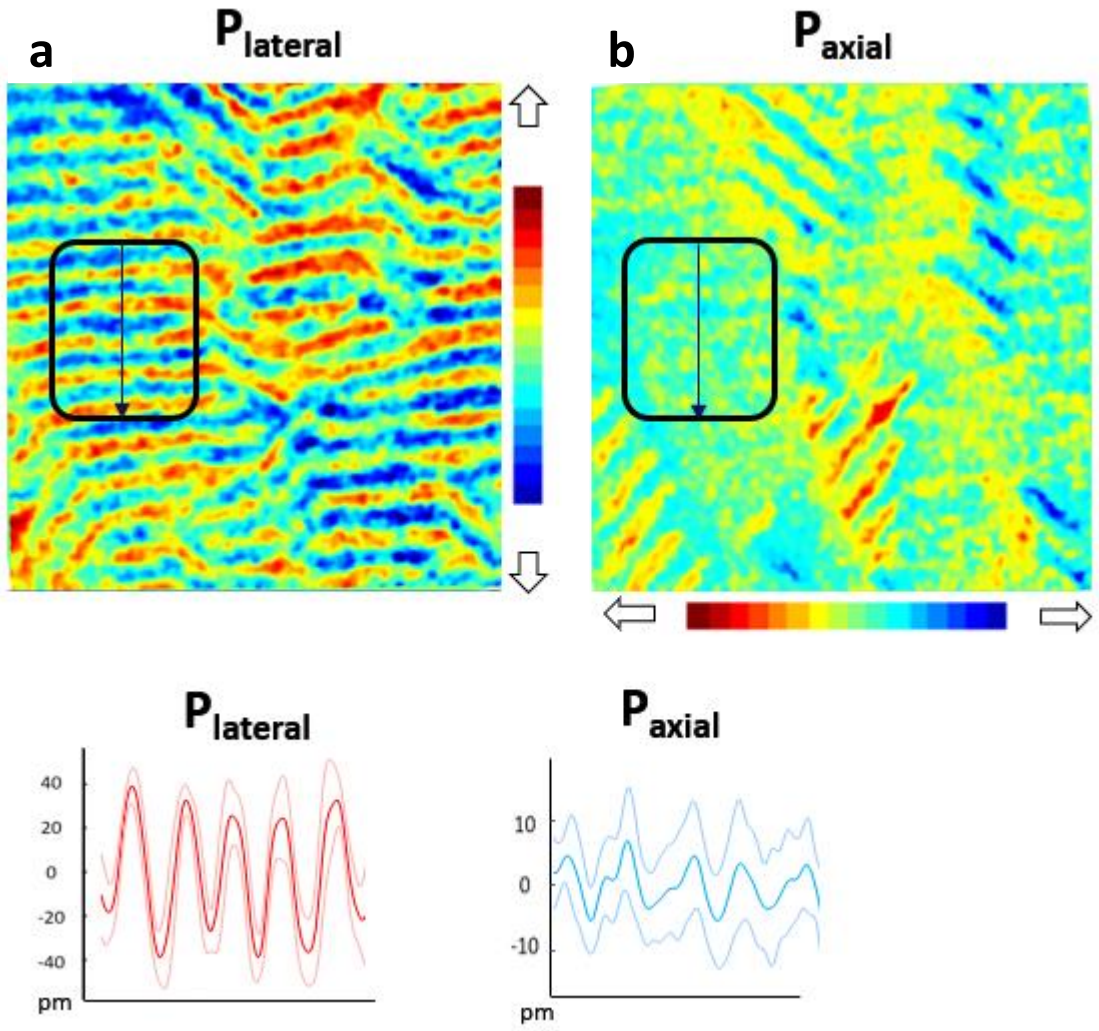

Figure 5.6 (a) lateral and (b) axial component of polarizations from Figure 5.5. Quartile analysis of profiles in 20%, 50%, and 75% curves are shown in the bottom figures.

The extraction of lateral and axial polarization mapping is shown in Figure 5.6 (a, b). It is obvious that the lateral polarization is much larger than the axial polarization. The displacement of the CW or CCW rotation of vortices shows different intensities in different areas, such as the left bottom and right bottom in Figure 5.6 (a). This intensity variation could be correlated to the chirality and is discussed in Chapter 6. The profile in a black box in (a) is probed and quantified by the quartile analysis that shows 25%, 50% (darker red), and 75% modulations in trends. The averaged CW, or CCW polar displacement is up to ~ 40 pm, which is close to the measurement of cross-sectional TEM in $(PTO)_n/(STO)_n$ superlattices. For reference, the bulk PTO at room temperature is as follows: the Ti and O ions are offset by 16.2 pm and by 47–49 pm relative to the Pb lattice in the direction opposite to the polarization, where in this research the Ti ion is used to infer the offset of the Ti-centered oxygen octahedra to determine the electric dipole [106]. About the axial polarization in Figure 5.6 (b), besides the large magnitude of ferroelectric a_1-a_2 twin

domains, the modulations along $[1\text{-}10]_o$ are miniscule. To see if any modulations are present, the profile in the black box in (b) with the quartile analysis reveals a modulation of up to 5 pm, which is around one-sixth of the lateral polarization. This modulation is not as uniform as the lateral one, and this suggests that the weak axial polarization is averaged and canceled by the depth of the planar-view TEM sample. Additionally, the rapid delocalization of the electron beam and the strong scattering on heavy atoms (Pb in this work) would make the top half of the PTO layer be more responsive to the polarization information.

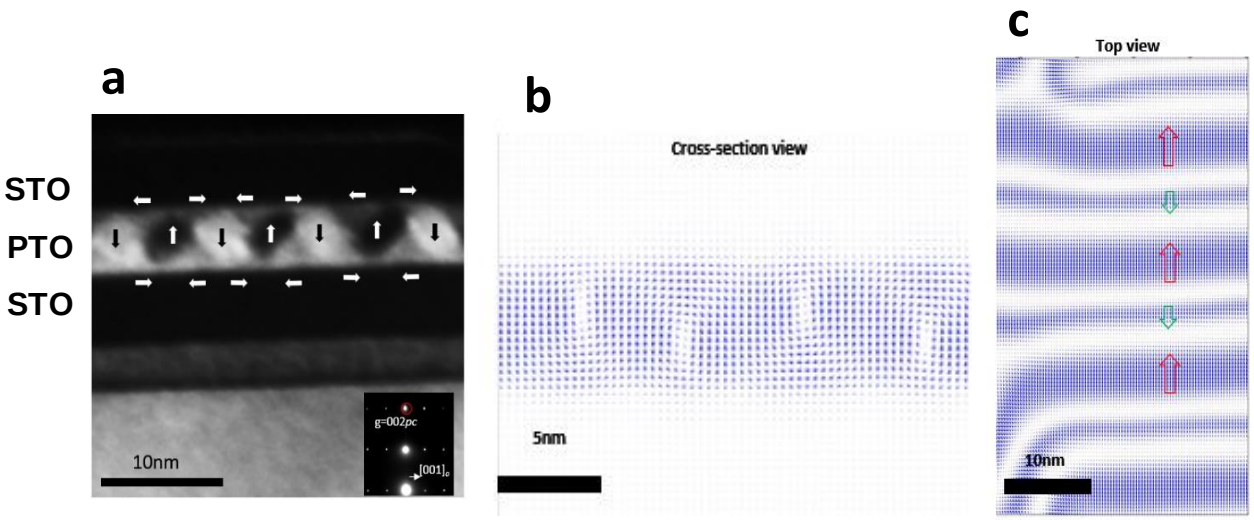

Figure 5.7 (a) DF-TEM in two-beam conditions on $(PTO)_n/(STO)_n$ trilayer heterostructures (n = 20) showing out-of-plane modulations. Polarization vector mapping of the $(PTO)_n/(STO)_n$ trilayer heterostructures (n = 20), calculated by phase-field modeling. (b) A cross-sectional view. (c) A top view.

Since the axial polarization of polar vortices in the $(PTO)_n/(STO)_n$ trilayer heterostructures (n = 12) is extremely weak due to the core of the vortex phase, the $(PTO)_n/(STO)_n$ trilayer heterostructures (n = 20) were explored due to the single vortex phase being without interference and due to the asymmetry of the vortex's core. When the periodicity is increased, the vortex core would change to zigzag symmetry, and, finally, out-of-plane c domains would grow to become classic c/a flux-closure domains. Thus, the asymmetric vortices would be better for measuring axial polarizations. Therefore, having the single vortex phase on the $(PTO)_n/(STO)_n$ trilayer heterostructures (n = 20) is the best means of probing the axial polarizations. As Figure 5.7 (a) shows, the DF-TEM in two-beam conditions shows out-of-plane modulations with black/white contrast in the PTO layer. The overall polarization distribution has a butterfly-like shape. This measurement again validates the vortex phase as the single phase in the $(PTO)_n/(STO)_n$ trilayer heterostructures (n = 20), but the vortex core is asymmetric in a zigzag arrangement. Polarization vector mapping, calculated by phase-filed modeling in Figure 5.7 (b), also suggests the zigzag arrangement of the vortex core. Furthermore, the calculation also suggests the top view of the polarization distribution in Figure 5.7 (c) with the CW and CCW stripes with large and small rotations of the vortices corresponding to the top view of the butterfly shape.

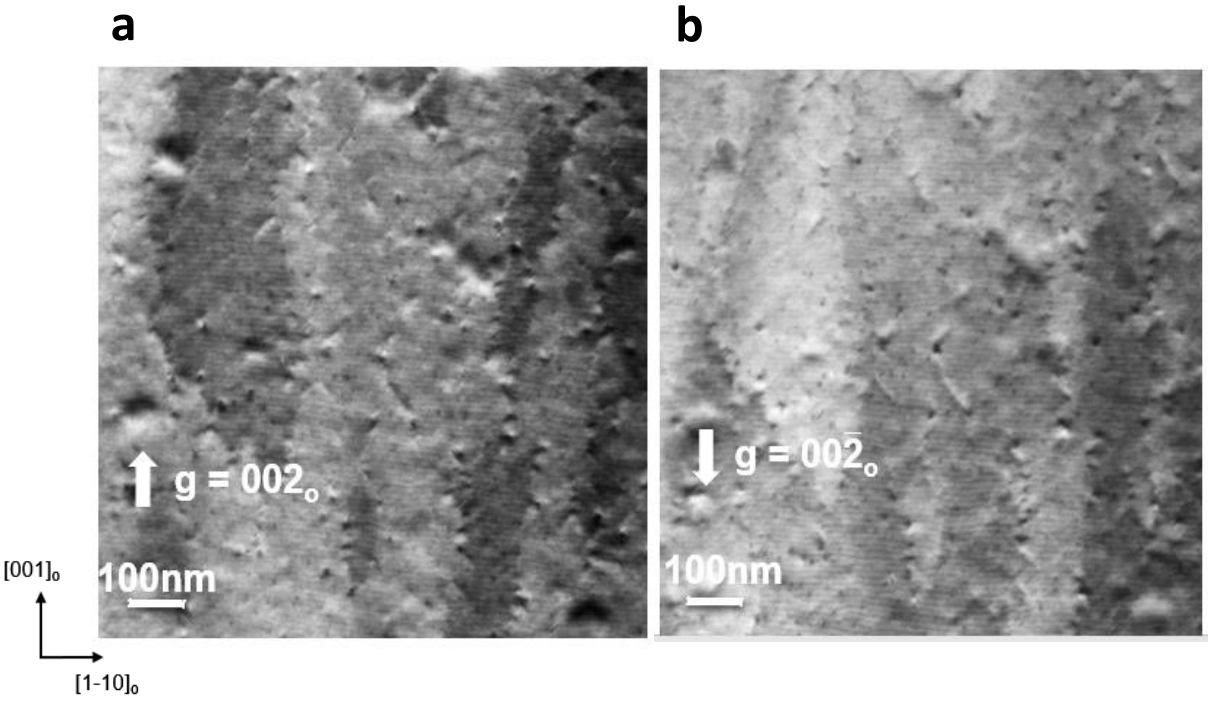

Figure 5.8 DF-TEM in two-beam conditions on $(PTO)_n/(STO)_n$ trilayer heterostructures (n = 20) showing a bulky stripe contrast with polar vortices along $[1\text{-}10]_o$: (a) +g vector planar-view imaging, and (b) -g vector planar-view imaging.

To further understand the behavior of polar vortices for the $(PTO)_n/(STO)_n$ trilayer heterostructures (n = 20), diffraction-contrast ± g-vector DF-TEM is applied through breaking Friedel's law on planar-view TEM samples. The two-beam conditions $[002]_o$ g-vector image in Figure 5.8 (a) reveals bulky stripe patterns in light/dark diffraction contrast, and the $[00\text{-}2]_o$ g-vector image in Figure 5.8 (b) verifies the reversal of the diffraction contrast due to the reversal of the sign for +g and -g vectors; this corresponds to bulky stripe contrast of the PFM study in Figure 4.7 (c). This evidence shows the collective behavior of polar vortices in different regions with overall reversal polarizations. Most importantly, stripes form an array in a spacing of ~10 nm periodicity and preferably lie on $[1\text{-}10]_o$ referring to the polar vortices in a spacing of ~10 nm in the $PbTiO_3/SrTiO_3$ trilayer heterostructures in Figure 4.5 (c).

To unveil the detailed information underneath the bulky stripe contrast, the weak-beam condition $[004]_o$ g-vector DF-TEM in Figure 5.9 (a) boosts the diffraction contrast of polar vortices and reveals the lateral polarization of polar vortices such as the CW or CCW rotation toward $[004]_o$. As I have already mentioned, the vortex stipes lie on $[1\text{-}10]_o$, and larger lateral displacements occur along ± $[001]_o$, compared to ± $[1\text{-}10]_o$ due to the easy axis of $[001]_o$. If one exchanges the substrate from $DyScO_3$ to SAGT, the vortex stripes prefer to lie along two axes, $[100]_c$ and $[010]_c$, due to the strain condition changing from tensile to almost zero strain. Even more, the arrangements of vortex stripes perform the twisting to form an anti-phase boundary instead of long and straight

lines. In the zoom-in imaging in Figure 5.9 (b), the anti-phase boundary shows the random offset of the left-side and right-side of the vortices. In such cases, dislocation-like vortex structures are formed in some areas marked by the yellow box and are possibly topologically protected in Figure 5.9 (a).

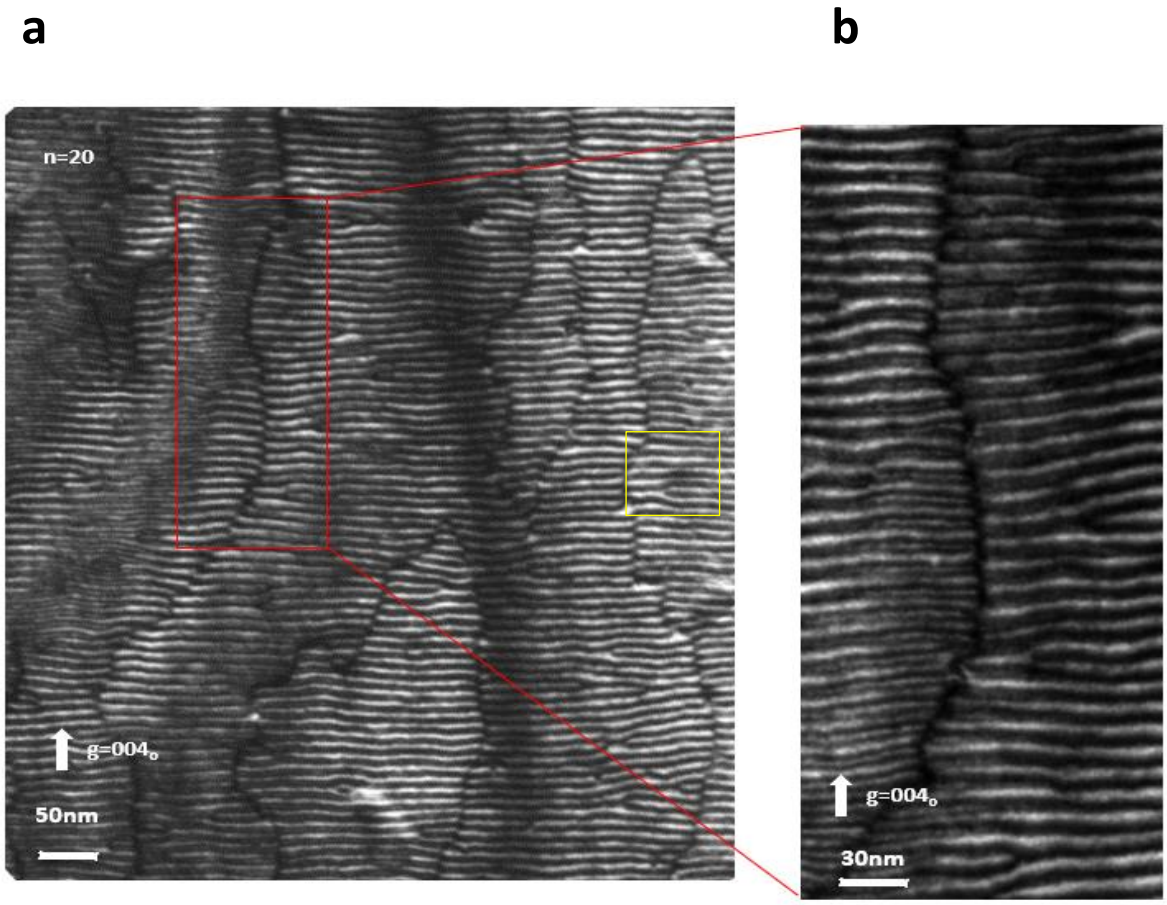

Figure 5.9 DF-TEM in weak-beam conditions on $(PTO)_n/(STO)_n$ trilayer heterostructures (n = 20) showing (a) polar vortices along $[1\text{-}10]_o$ with an anti-phase boundary with log magnification. (b) Zoom-in imaging shows the explicit random offset between the left and right sides of the polar vortices.

.

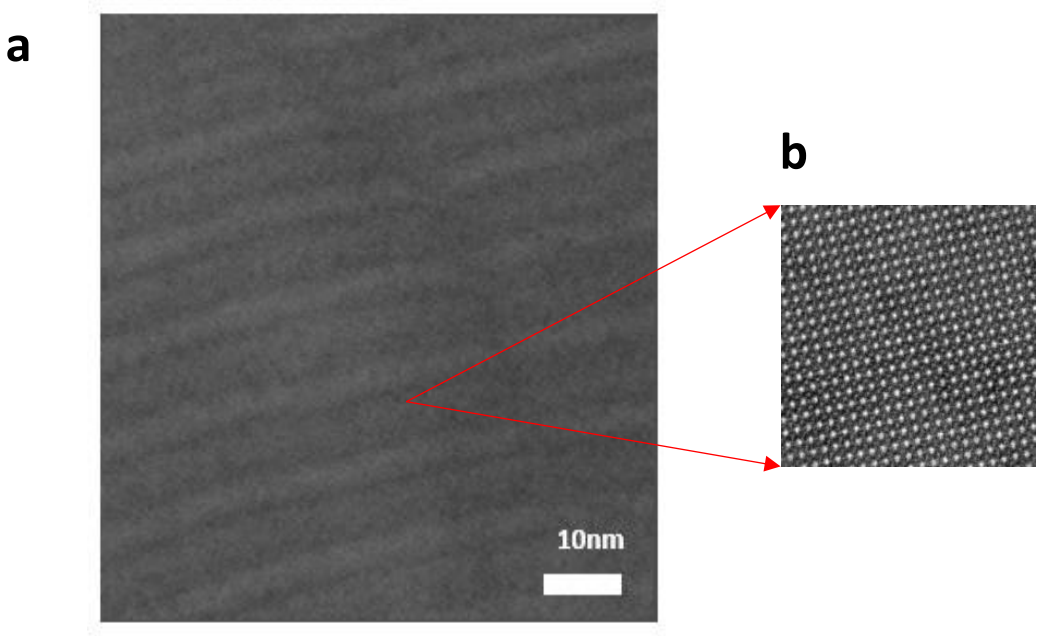

Figure 5.10 HR-STEM imaging on $(PTO)_n/(STO)_n$ trilayer heterostructures (n = 20) zone axis showing (a) polar vortices along $[1\text{-}10]_o$ with an anti-phase boundary. (b) Zoom-in imaging shows the clear ABO_3 perovskite structure.

.

The anti-phase boundary composed of polar vortices could have influenced the polarization distribution. Hence, through the utilization of atomic resolution HR-STEM imaging in planar view, the zone axis of the $PbTiO_3$ was focused in the planar-view sample, and a high-quality large view of the ABO_3 structure in the high-angle annular dark field (HADDF) Z-contrast imaging is illustrated in Figure 5.10 (a, b). This image contrast provides the boundary between polar vortices, with the anti-phase boundary in the middle right of the image due to the in-plane strain dechanneling. Primarily, I probed the non-centrosymmetry of the sublattice displacement in order to determine the polarization distribution with angle mapping in Figure 5.11 (a). The polarization mapping exhibits the polar vortices along $[1\text{-}10]_o$ (red is the CW rotation of vortices, while light blue is the CCW rotation of vortices) in a spacing of ~10 nm, and the small boundary between two polar vortices shows a black color, indicating the out-of-plane component of the vortices. In this regard, the straight boundary of the vortices turns out to be more stable than the polar vortices in the trilayer heterostructure (n = 12).

The alternating CW and CCW rotations of polar vortices exhibit twisting 180° on the anti-phase boundary, corresponding to the weak-beam diffraction contrast study in Figure 5.9. Calculated vector mapping by phase-field modeling validates the twisted anti-phase boundary with the alternative rotation of the CW/CCW vortices, as in Figure 5.11 (d). The axial component can be resolved by separating the in-plane polarization into the lateral and axial component of the polar vortices. As Figure 5.11 (b) shows, lateral polarizations again contribute significantly to the polarization distribution of polar vortices and exhibit the twisting of the anti-phase boundary.

Surprisingly, the antiparallel axial polarizations of polar vortices with a small magnitude can be probed to provide a 3D chirality, as in Figure 5.11 (c). In both lateral and axial polarization mapping, it is obvious that the collective behavior of polarization occurs between the left and right side of the region, and this suggests the role of the anti-phase boundary to influence the polarization distribution.

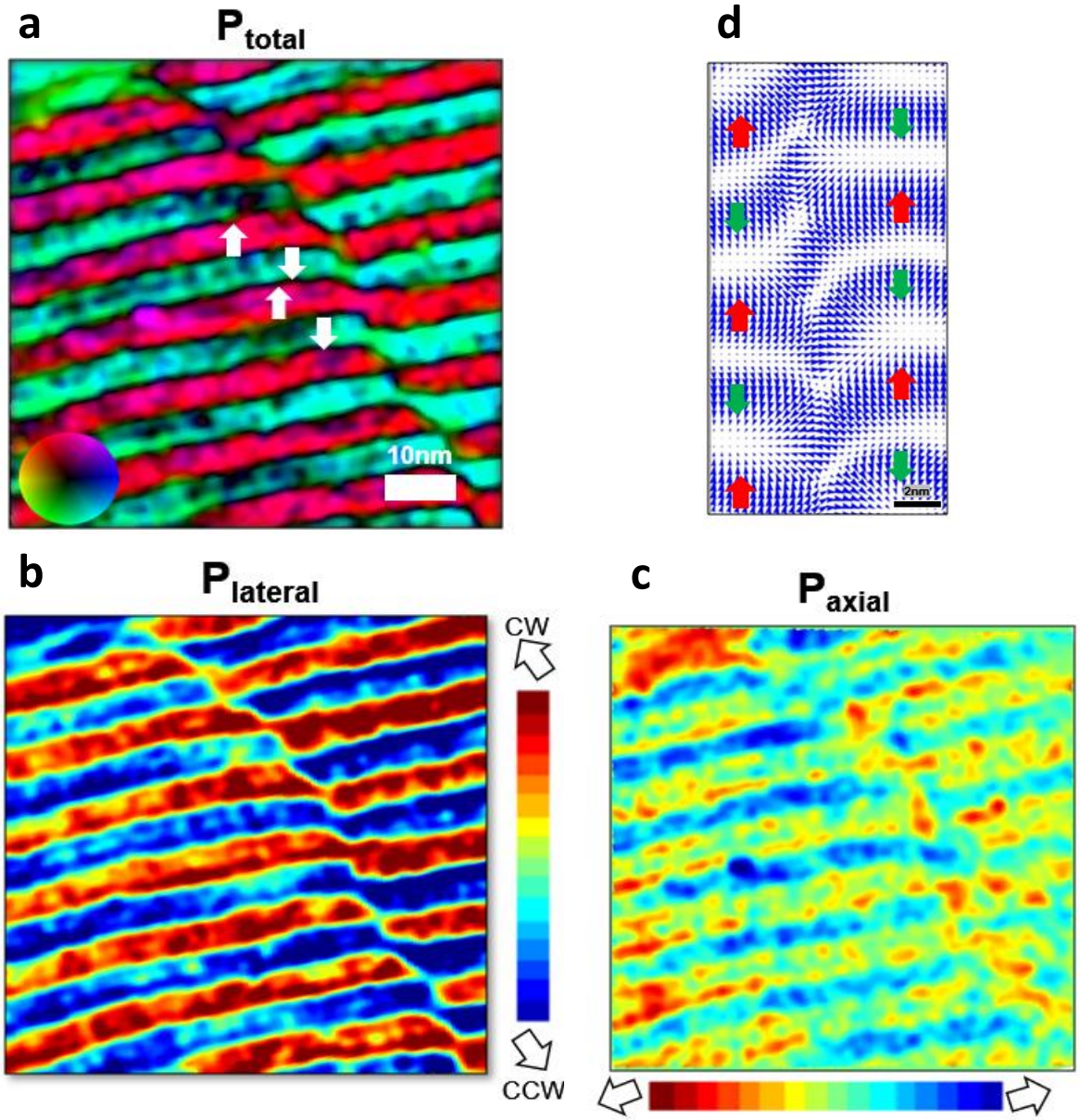

Figure 5.11 Atomic polarization mapping on $(PTO)_n/(STO)_n$ trilayer heterostructures (n = 20) zone axis, showing (a) the total polarization mapping with angle indication, (b) the lateral polarization mapping, (c) the axial polarization mapping, and (d) the polarization vectors of the anti-phase boundary.

Furthermore, the quantification of polarization distribution is shown in Figure 5.12 to present the quartile analysis of the left side and right side of the vortex region so as to show the trends of the polarizations. Significant displacement of the vortex comes from the lateral component up to 40 pm, and the magnitude of the axial component is up to 10–15 pm. Surprisingly, there are two modulations in the axial component. One is the single peak (CW), while the other is the double peak (CCW)—possibly due to the alpha angle 87.2° of the substrate causing the anisotropy of polarization along $[1\text{-}10]_o$. The different amplitudes of the axial polarization across the anti-phase boundary suggest that this anti-phase boundary plays an important role in changing the polarization distribution and even, to a certain degree, in changing the chirality of the vortices. In addition, the profile of axial polarization extracted by phase-field modeling clarifies the two modulations, the single peak, and the double peaks, these two modulations corresponding to the quartile analysis of the HR-STEM in Figure 5.12. Another piece of evidence, as Figure 5.14 illustrates, calculated from the first-principles simulations on the $(PTO)_n/(STO)_n$ superlattices heterostructures (n = 6) on the DSO substrate in cross-sectional view, also suggests the potential two modes of axial component—where the axial polarizations exhibit two peaks in a red color and the other peak in a blue color, and this implies the asymmetry of the substrate correlated to the axial polarizations.

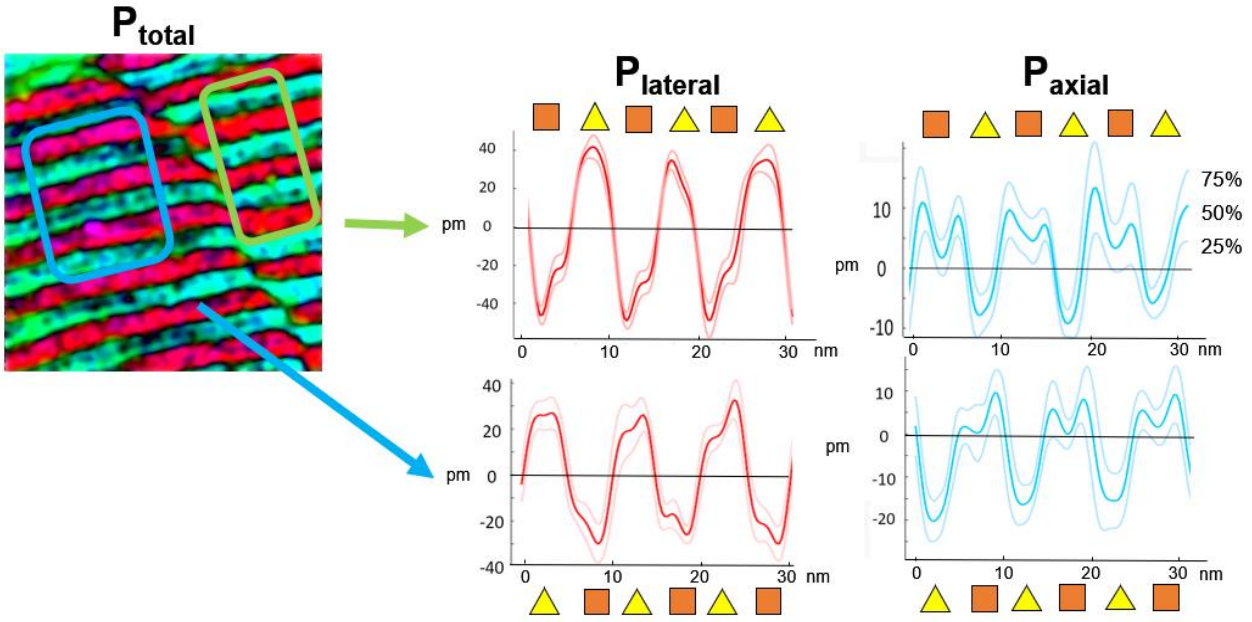

Figure 5.12 Quartile analysis of the atomic polarization mapping on $(PTO)_n/(STO)_n$ trilayer heterostructures (n = 20), showing a different polarization distribution of left (blue box) and right (green box) sides of the vortex region. There are two modulations in the axial polarizations.

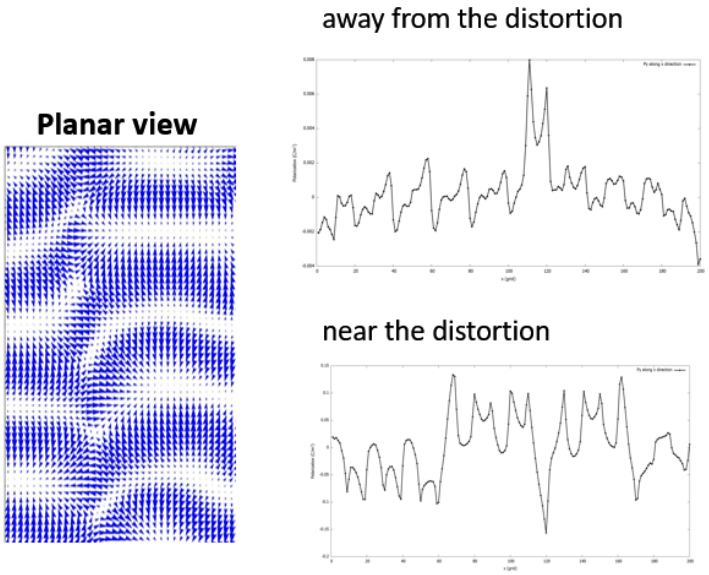

Figure 5.13 Polarization vector mapping, showing an anti-phase boundary composed of polar vortices as well as the profile of the axial polarizations near and away from the boundary from phase-field modeling.

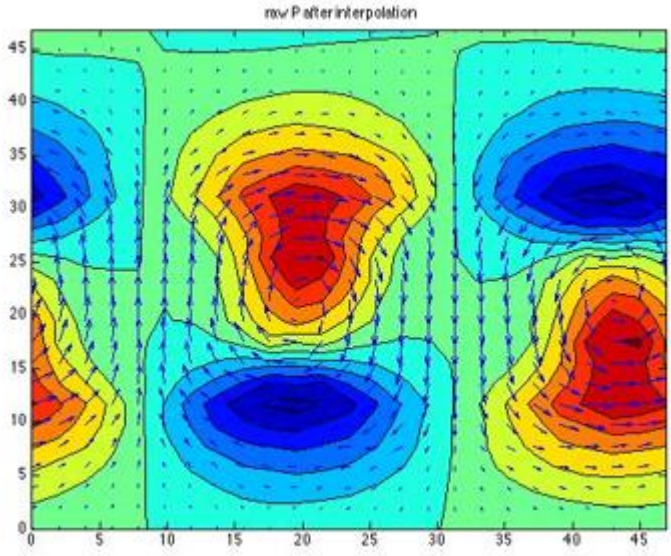

Figure 5.14 Polarization vector, mapping with antiparallel axial polarization (red/blue, in/out of the page) of polar vortices in $(PTO)_n/(STO)_n$ superlattices heterostructures (n = 6) on a DSO substrate in cross-sectional view, calculated by first-principles simulations.

5.4 Summary

In sum, the antiparallel axial polarizations of polar vortices are not straightforward to probe due to their weak magnitude. However, if one uses the zone axis of the TEM techniques, including electron diffraction and HR-STEM imaging with atomic displacement mapping, then the antiparallel axial polarizations of polar vortices in the $(PTO)_n/(STO)_n$ trilayer heterostructures can be probed—revealing that they have modulations in real space and reciprocal space. Most importantly, these pieces of evidence can prove that 3D chirality shows the helicity arrangement of polarization. Furthermore, the anti-phase boundary is composed of polar vortices, where the vortex state flips 180° to the other side of the anti-phase boundary. According to the quantification of polarization distribution of the two sides of the anti-phase boundary, this boundary can change the polarization distribution across the boundary, thereby potentially causing a gradient of chirality (to be discussed in the next chapter).

Chapter 6
Chiral vortex domains in ferroelectric heterostructures

After the structural characterization of trilayer heterostructures (which Chapter 5 described), antiparallel axial polarizations of the vortex state can be measured—suggesting that the vortex phase possesses not only a 2D cycloid polar distribution but also 3D chirality with helicity. Since the single vortex phase was found to possess helicity, the collective polarization behavior of polar vortices with an anti-phase boundary and their chirality should be valuable to investigate and discuss. Furthermore, the identification of chirality in polar vortices is vital for clarifying the handedness of the polar vortices. This chapter focuses on the microscopic and macroscopic spatial arrangement of several regions composed of polar vortices with the anti-phase boundary in order to search for a different handedness and for novel phases for the sake of possible future electronic device applications.

6.1 Introduction

Chirality is a unique property and a widespread phenomenon in nature—defined as an object whose mirror image cannot be superimposed onto the original object. The handedness control of chiral molecules with specific responses has already helped to design essential applications in biological categories such as drug and chemical biology in our daily life. For example, optically active materials with chiral symmetry can rotate the polarization direction of linearly polarized light when light travels through this material. Given the exciting phenomena and intriguing properties in ferroic materials, chiral magnetic materials have already been extensively investigated, such as chiral magnetic domains [147] and chirality in nanoscale magnets [148,149]. The spin-orbital interaction, called the D-M interaction, twists the magnetization to induce topological defects such as magnetic skyrmions—which demonstrate chirality in most cases [64,150–152] – and topological chiral domain walls [129] [153]. Additionally, the ability to tune the chirality of Bloch-type and Néel-type domain walls has been demonstrated [154–156]. These scientific developments promise future applications for information storage and spintronic devices.

As for ferroelectric materials lacking the spin-orbital interactions, domain walls traditionally separate domains resulting uniform polarizations without chirality and reveal physical properties diversely [122]. The complex ferroelectric domain walls such as Bloch-type and Néel-type present the local polarization rotation and offer a glimpse into the discovery of chirality [157–159]. In the search for ferroelectric chiral domains, topological defects such as vortex structures can become the best candidate. The possibilities of clockwise (CW)/ counterclockwise (CCW) rotation and antiparallel axial polarization in two directions of the vortex structure are potential to resolve left-handedness and right-handedness chirality. In recent studies, polar vortices as the localized dipole textures reveal a non-uniform polarization state in the ferroelectric superlattices due to the interactions between the electrostatic and elastic boundary conditions [11,134]. Also, when resonant soft X-ray diffraction is used, the strong circular dichroism from circularly polarized light on the polar vortices in the superlattices is indicative of chiral structure [13]. On the basis of the previous two chapters, the single vortex phase in trilayer heterostructures can be discovered and can be proved to possess structural 3D chirality with a helicity corresponding to the results of resonant soft X-ray diffraction. The identification of chirality in trilayer heterostructures can provide a different handedness, and the handedness can be characterized by the sign of the helicity, as Figure 6.1 shows. The helicity density is defined as follows:

$$\mathcal{H} = \int \vec{P} \cdot (\nabla \times \vec{P}) d^3\vec{r} \tag{6-1}$$

And the sign of the scalar field is defined as follows:

$$\gamma = sign(\mathcal{H}) \tag{6-2}$$

It should be noted that the overall chirality is defined as a volume integral over the CW and CCW polar vortices. There are three possible degenerate states with different chiral properties: right-handed helicity with positive helicity density, the achiral structure with zero helicity, and left-handed helicity with negative helicity density. Most importantly, the chirality distribution of vortex

structures is essential for the possible manipulation of chiral domains [160–163] in erasing or writing handedness domains deterministically.

.

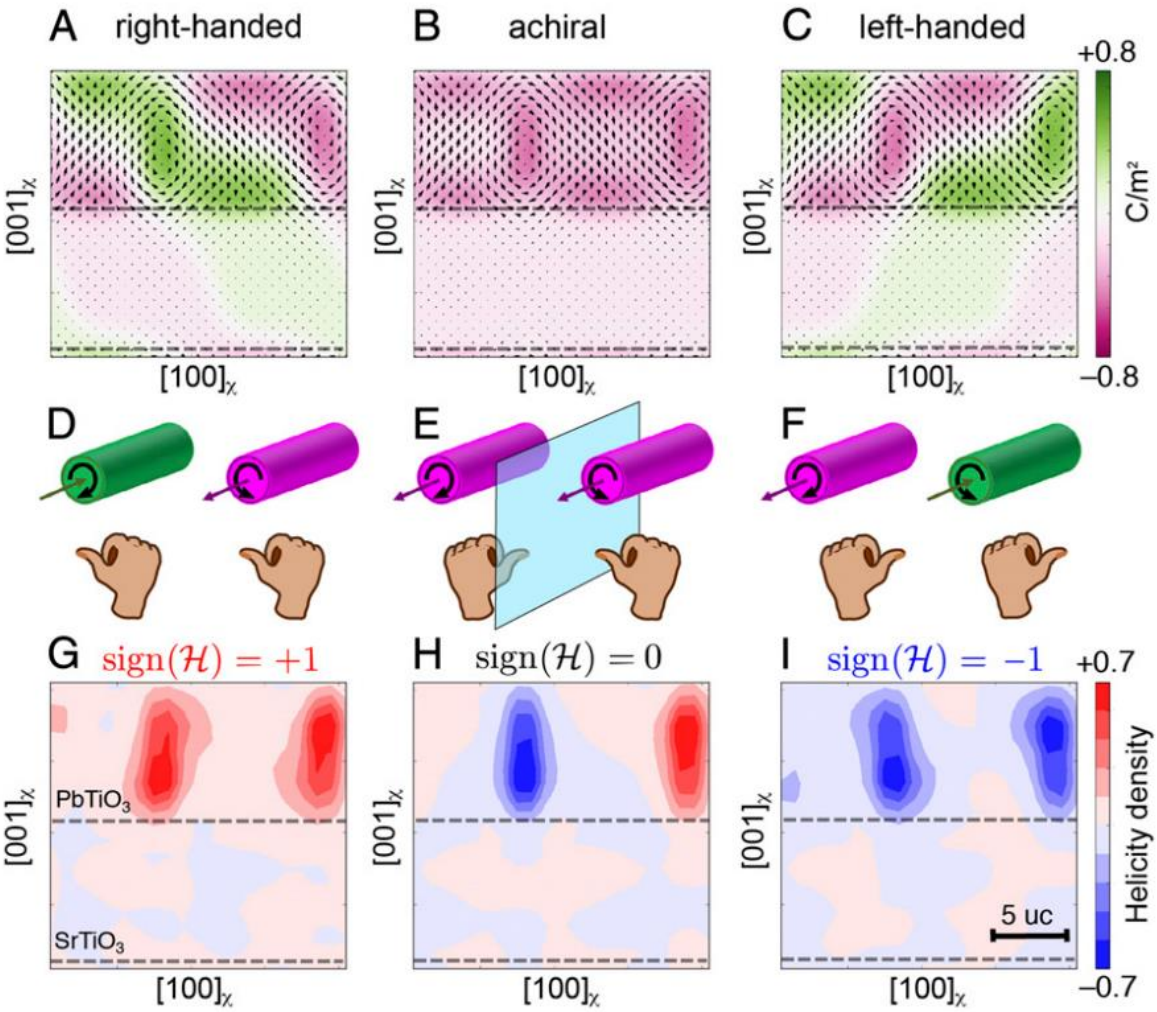

Figure 6.1 Second-principles calculations on $(PTO)_n/(STO)_n$ superlattices (n = 10) show three different degenerate ground states with different chiral properties: right-handed, achiral, and left-handed. Adapted from [13]

6.2 Chirality identification of anti-phase boundary with polar vortices

While I found the axial polarization of vortices in Figure 5.11 (c), I can identify the whole area as a chiral structure by using fundamental mirror symmetries in three dimensions, through which any mirror image and the original object are non-superimposable by any translation or rotation, as Figure 6.2 illustrates. The original object is at the middle left showing the distribution of in-plane polarizations, and the expected out-of-plane polarizations at the boundaries are marked with circles. Through the use of the mirrors on three axes to inspect the symmetry, the three reflected images all can be superimposed onto one another but cannot be superimposed onto the original object by any combination of rotations and/or translations. Thus, this region can be identified as having a net chirality. Most importantly, based on the sign of the lateral and axial polarizations in Figure 5.11, the chirality of this region only follows the left-handed rule through exhibiting left-handed helicity across the anti-phase boundary. According to previous simulated work on the $(PTO)_n/(STO)_n$ superlattice heterostructures (n = 20) [13], there are three degenerate ground states, as Figure 6.1 illustrates. Two of the structures are chiral enantiomers, which have left- or right-handed helicity showing the same helicity density concentrated at the vortex cores, and the third structure is an achiral structure having alternating helicity in neighbor vortex cores [13]. Furthermore, the two sides of the anti-phase boundary reveal the varying magnitude of lateral and axial polarizations of the polar vortices, and this suggests the different extent of helicity density. This variation of helicity density implies that different helicity density in other regions can vary to the other end of right-handed helicity.

By rigorously exploring the polar vortices with an anti-phase boundary, I also found a region only following right-handed helicity and that had similar behavior with an anti-phase boundary changing the polarization distribution on both sides of the boundary. As Figure 6.3 (a) shows, the high-quality HR-STEM imaging on the zone axis shows the polar vortices along $[1\text{-}10]_o$ as well as the random offset of the two sides of polar vortices at the anti-phase boundary. It should be noted that the straight boundary and the arrangement of the polar vortices here are the same as the previous region with left-handed chirality. Thus, the atomic polarization distribution, as Figure 6.3 (b) shows, exhibits similar CW and CCW rotations of polar vortices with the anti-phase boundary. The right side of the anti-phase boundary shows a higher magnitude than left side, and this implies the role of the anti-phase boundary in changing the polarization distribution. As Figure 6.3 (c, d) shows, lateral polarizations and axial polarizations exhibit the different magnitudes of polar vortices across the boundary, corresponding to previous results, and axial polarization also proves polar vortices to have 3D chirality. Lastly, the chirality in this whole region only follows the right-hand rule to have right-handedness chirality. Consequently, the gradient of helicity is changed by the anti-phase boundary, composed of polar vortices widespread in trilayer heterostructures.

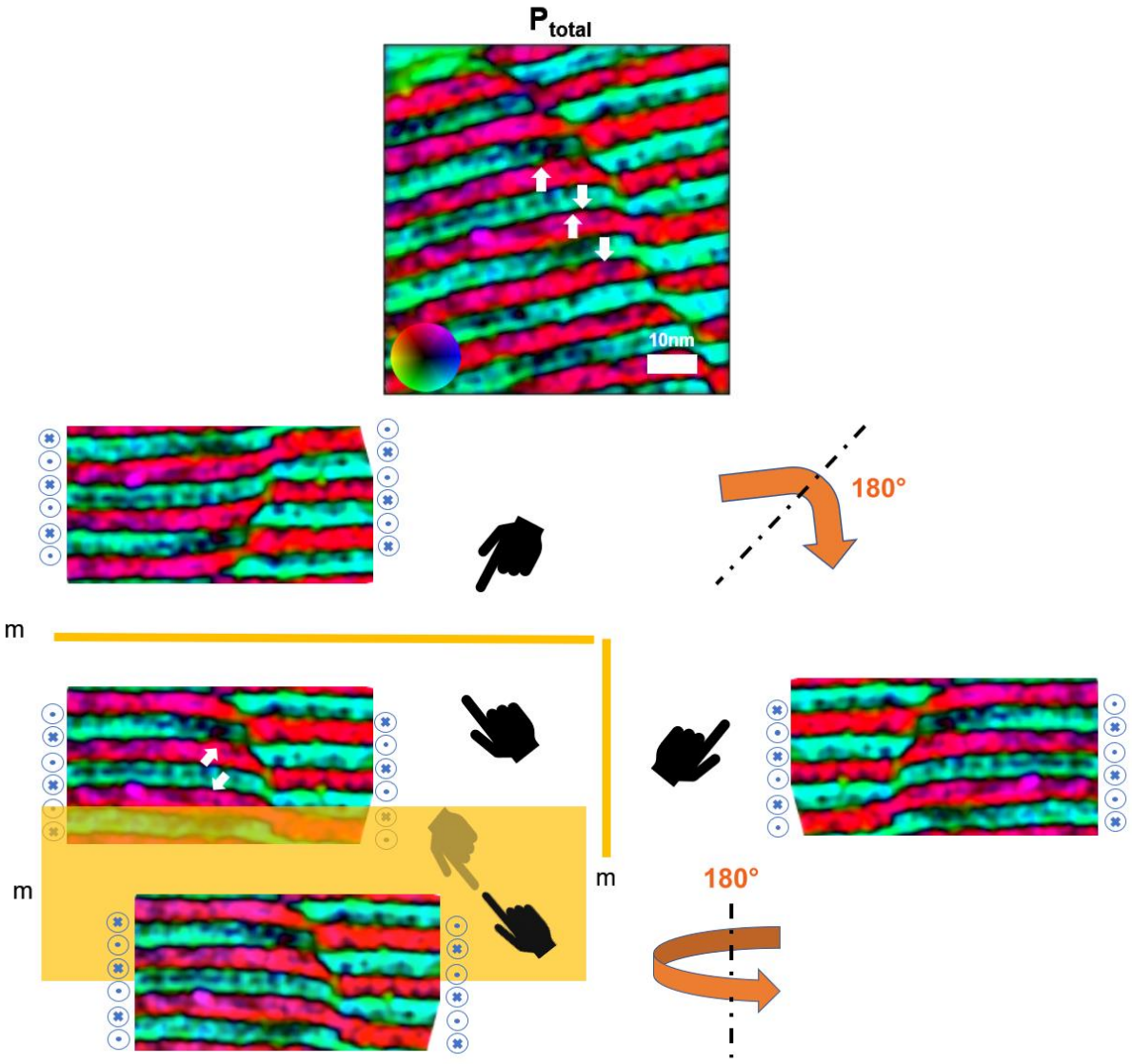

Figure 6.2 The identification of chirality on the polar vortices with the anti-phase boundary with the use of mirror symmetries in all dimensions.

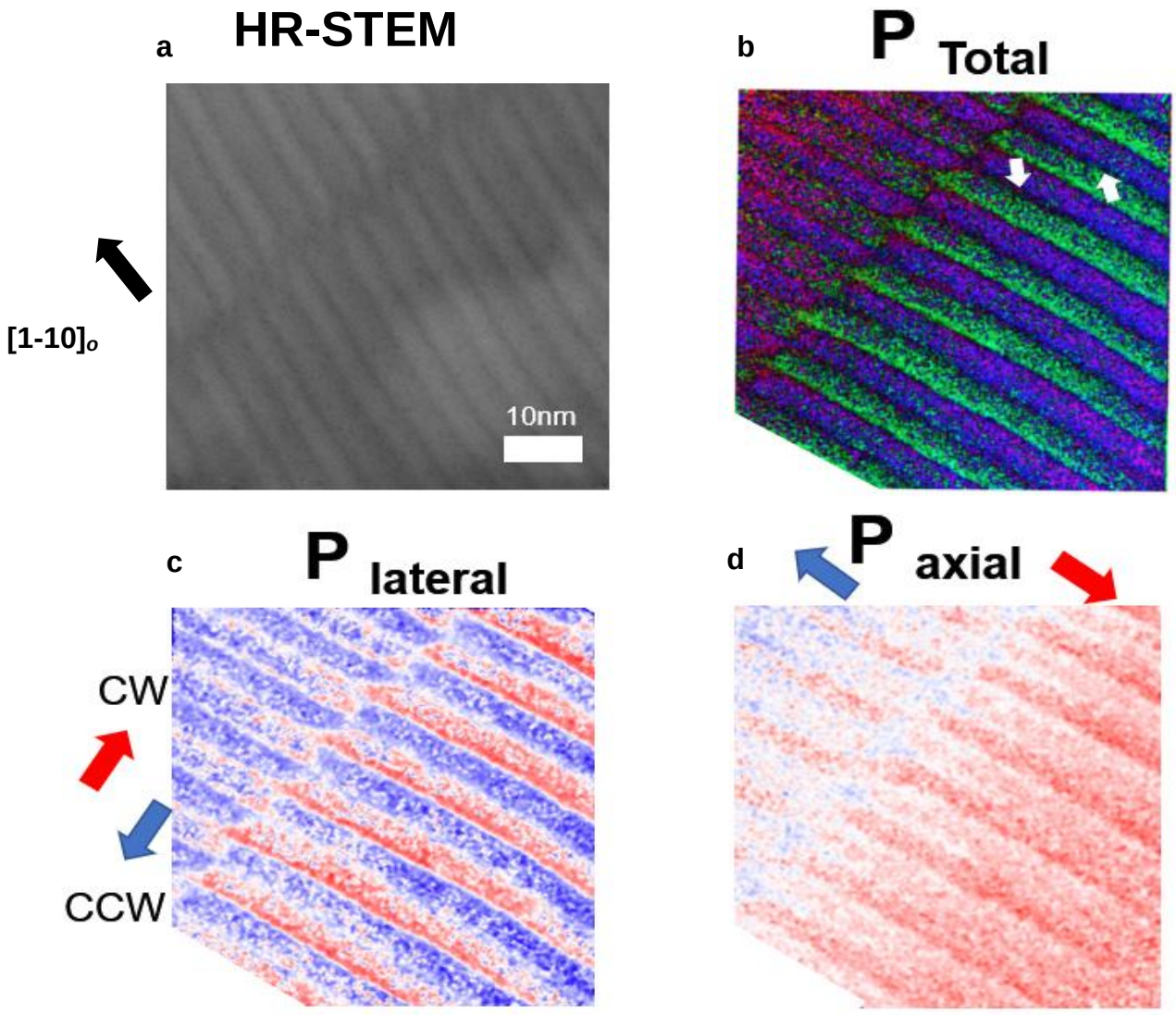

Figure 6.3 The anti-phase boundary composed of polar vortices showing the right-handed helicity, depicted through: (a) HR-STEM imaging, (b) total polarization mapping, (c) lateral polarization mapping, and (d) axial polarization mapping.

6.3 Achiral Structure

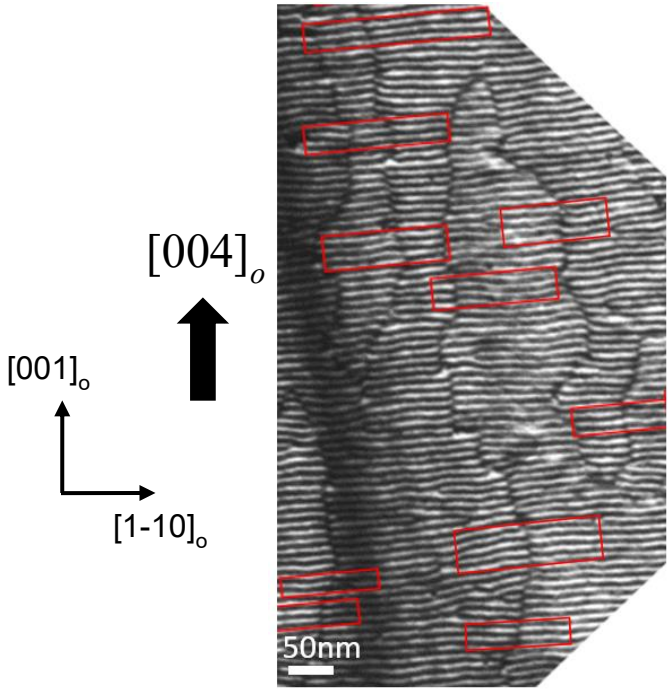

Figure 6.4 Low magnification of DF-TEM in weak-beam conditions. Red boxes exhibit the continuity of the left side and the right side of the polar vortices across the boundary.

After the regions of the left-handed and right-handed helicity are discovered, the achiral region should be in the middle of these two regions to complete the gradient of helicity. Without symmetry breaking, the achiral structure such as the mixing region with the left-handed and the right-handed helicity can be found in nature [162,164]. The diffraction-contrast TEM using a weak-beam conditions $[004]_o$ g-vector in Figure 6.4 and marked by red boxes shows that the same rotation of two vortices lie across the boundary only in some local regions. As I mentioned before, the offset on the left and right sides of the anti-phase boundary is random, and, eventually, it would reach the zero offset and form structures with the same rotational polar vortices. Again, to disclose the polarization distribution of this local region, the atomic resolution HR-STEM with polar mapping is needed. The HR-STEM in Figure 6.5 (a) shows the faint structures of polar vortices. It is not simple to find this structure in the STEM mode, but this structure can be traced by anti-phase boundary. As Figure 6.5 (b) shows, the total polarization mapping exhibits the same rotations of the polar vortices across the boundary and does not reveal the anti-phase boundary. In turn, the polar vectors at the middle of the boundary could have an out-of-plane projection along the $\pm [110]_o$, and this type of polarization distribution could be the precursor for the skyrmion-like textures emerging in the PTO/STO superlattice heterostructures on the STO substrate with compressive strain [165]. In this local region, lateral polarization mapping, as in Figure 6.5 (c), reveals the connection of two CW rotations of vortices and few displacements at the middle of the boundary. The axial polarizations mapping exhibits different axial polarizations across the boundary, as shown in Figure 6.5 (d), and almost zero displacements at the middle of the boundary.

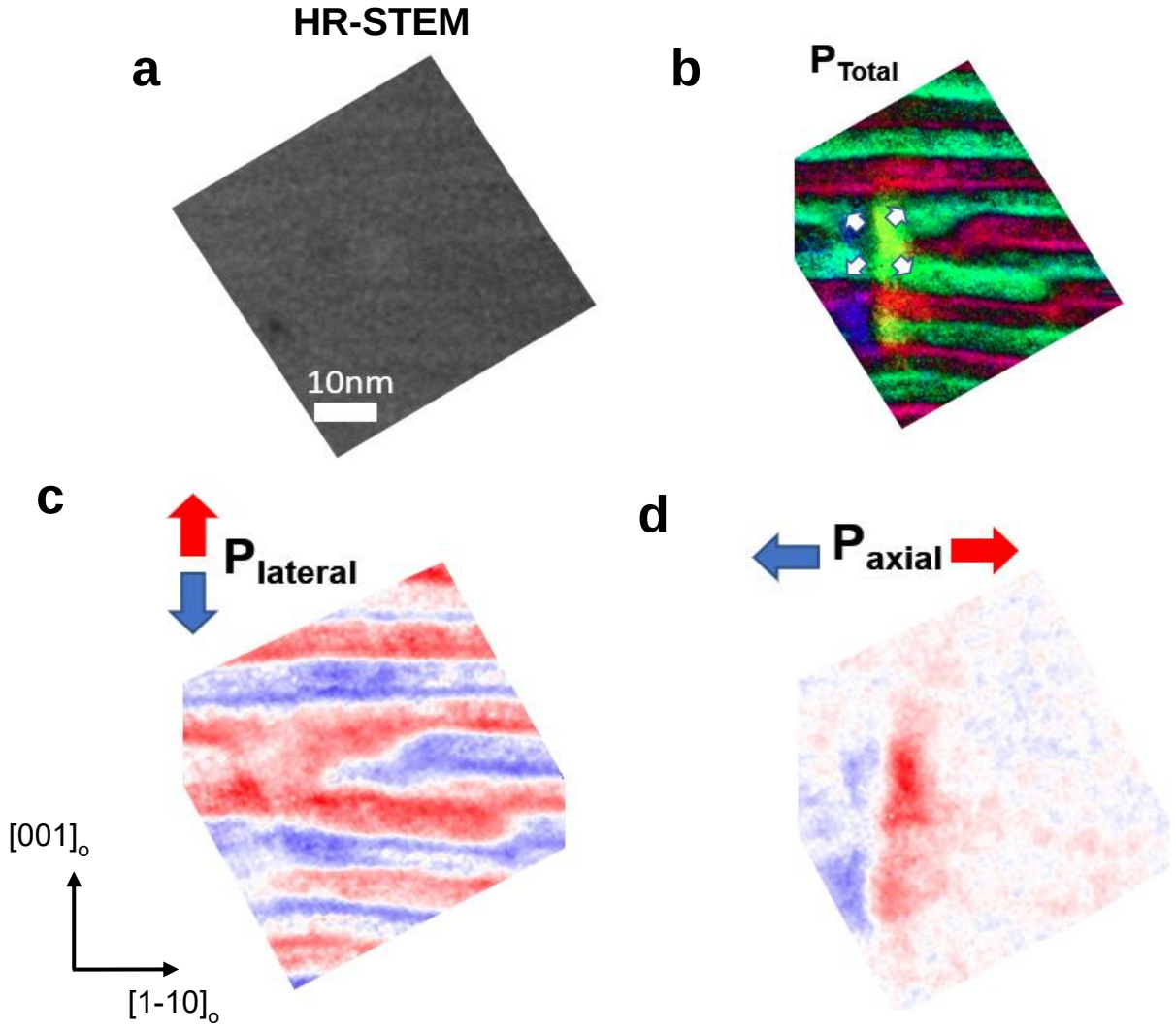

Figure 6.5 Polarization mapping on the same rotation of polar vortices, through the use of: (a) HR-STEM imaging, (b) total polarization mapping, (c) lateral polarization mapping, and (d) axial polarization mapping.

By identifying chirality through using fundamental mirror symmetries in three dimensions on this structure, as Figure 6.6 shows, I can prove that this vortex region has an achiral structure. The original object is at the middle left of Figure 6.6, with in-plane and expected out-of-plane polarizations. Through the reflection via mirror symmetry to get the enantiomers, the enantiomer from the 110_o plane at the right side shows the same type as the original object and can thus be superimposed onto the original object. This structure is identified as the achiral structure. Furthermore, when the left- and right-hand rules are used to differentiate the handedness of this structure, the left side of the boundary only follows the right-hand rule, while right side of the

boundary only follows the left-hand rule. The two different types of handedness would be cancelled out to an achiral structure corresponding to the achiral structure following left- and right-hand rule with a mirror at the boundary from first-principles calculations [13].

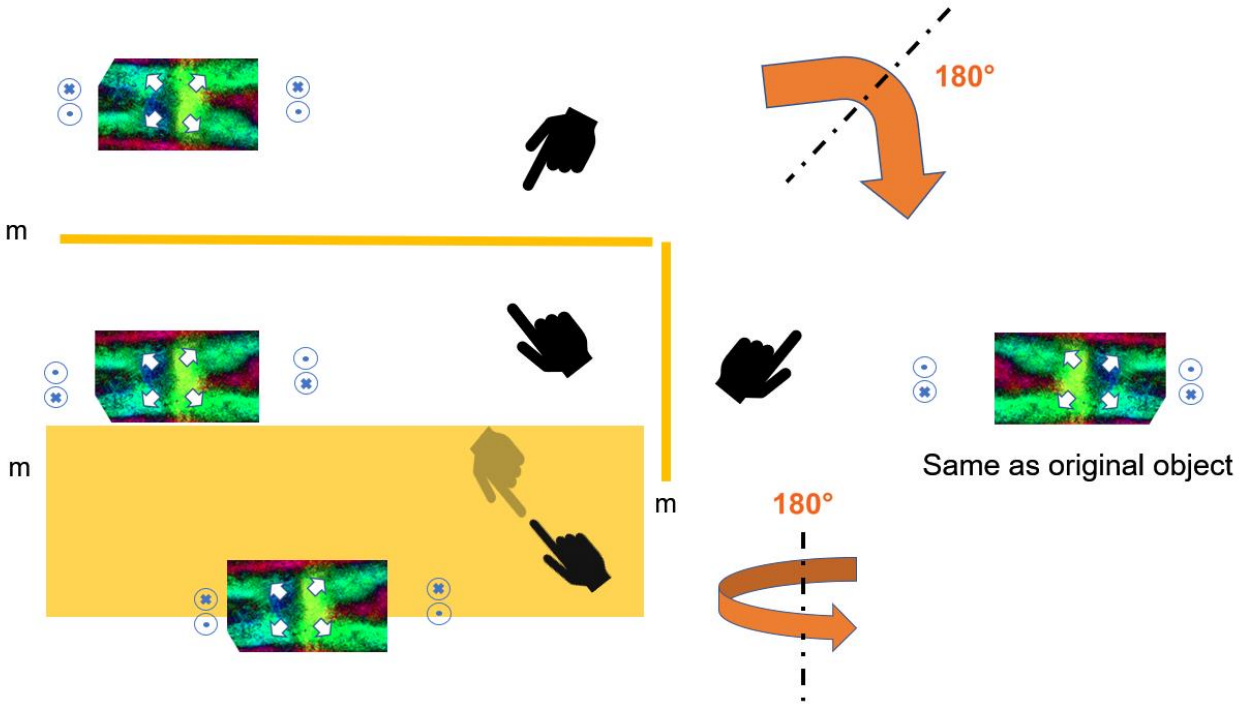

Figure 6.6 The identification of chirality on the polar vortices with the same rotations of vortices using mirror symmetries in all dimensions shows that this structure is achiral.

Next, the lateral PFM in a fast scan $[001]_o$ has reached the limit of the tip capability to probe the local polar structure ~25 nm. This direction of scan is only sensitive to the response of ± $[1\text{-}10]_o$. The amplitude signal marked by the red box shows strong signals on two polar variants that are separated by the sharp boundary, while the phase signal shows the contrast of different phases—meaning two strong polar variants pointing ± $[1\text{-}10]_o$, respectively, as Figure 6.7 (a, b) illustrates, and corresponding to the different axial polarizations across the boundary in Figure 6.5 (d). Hence, the lateral-PFM study proves the existence of the achiral structure as well as the axial polarizations correlated to the 3D chirality.

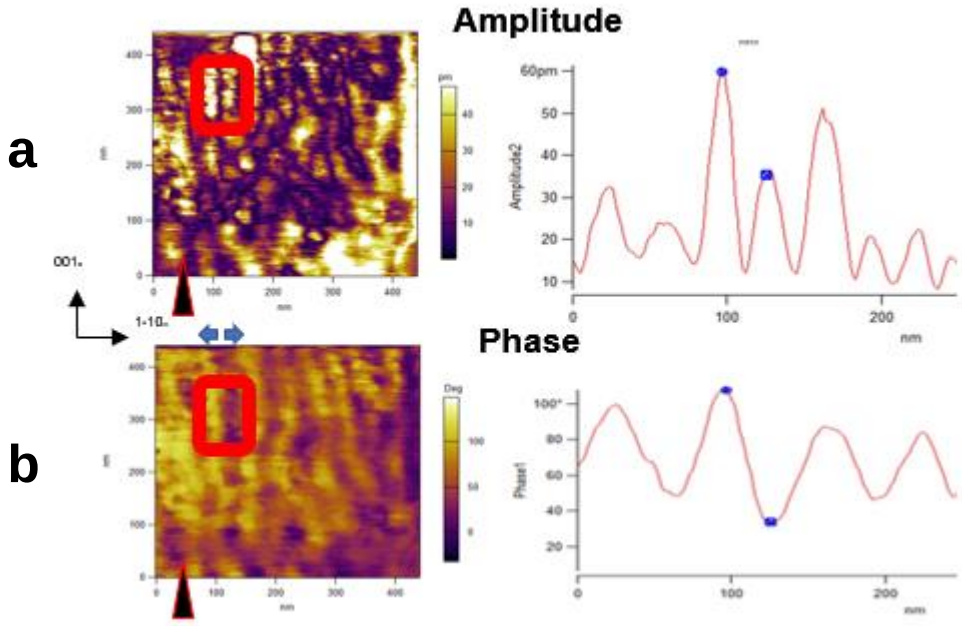

Figure 6.7 Detecting the achiral structure using lateral PFM along $[1\text{-}10]_o$. (a) The amplitude graph shows strong responses between the boundary. (b) Phase changes occur between the boundary.

6.4 Chiral vortex domains with handedness

The next outstanding problem lies in understanding the collective behavior that emerges in polar vortices—in particular, how chirality distributes based on adjacent left-handed, right-handed, and achiral regions. To investigate the macroscopic symmetry properties, the rotation symmetry property of the nonlinear susceptibility tensor is probed through the use of SHG spectroscopy with circularly polarized excitation. The left-handed (LH) and right-handed (RH) polarized SHG images, as shown in Figure 6.8 (a, b), indicate that the asymmetry of the polar vortices leads to different LH and RH SHG intensities. This asymmetry can be quantified as the circular dichroism (CD) signal as shown in Equation 6-3:

$$\frac{I_{left\ handedness} - I_{right\ handedness}}{I_{left\ handedness} + I_{right\ handedness}} \tag{6-3}$$

In this equation, the observation of localized CD values as large as ± 0.5 can be seen, while the average response of the polar vortices to LH and RH polarized light varies spatially over lengths of ~1 um due to their characteristic domain formation. This is manifestly seen in the CD intensity mapping, as Figure 6.8 (c) shows, as an intensity modulation similar to the bulky stripe pattern of lateral PFM study in Figure 4.7 (c). The different chirality correlates to the lateral polarizations.

Furthermore, a line profile (Figure 4d) along the $[1\text{-}10]_o$ axis representing the intensities along the red line (Figure 4c) highlights the periodic nature of the SHG-CD intensity variation, corresponding to different areas of left-handedness (+), right-handedness (-), and achiral structural regions. This is consistent with previous local polar structure analysis. This kind of CD signal is analogous to the SHG-CD reported in a variety of systems in nature such as bio-molecules [166], nanostructures [110,167,168], and 2D semiconductors [111]. In contrast to the chiral domains composed by vortices, traditional ferroelectric a_1-a_2 twin domains in the $(PTO)_n/(STO)_n$ trilayer heterostructure (n = 12) can be probed as the achiral structure in CD mapping, as Figure 6.9 shows. Therefore, based on the SHG-CD study, not only do local vortex regions possess chirality due to the gradient of helicity but also regions of macroscopic chirality exist throughout the trilayer heterostructures.

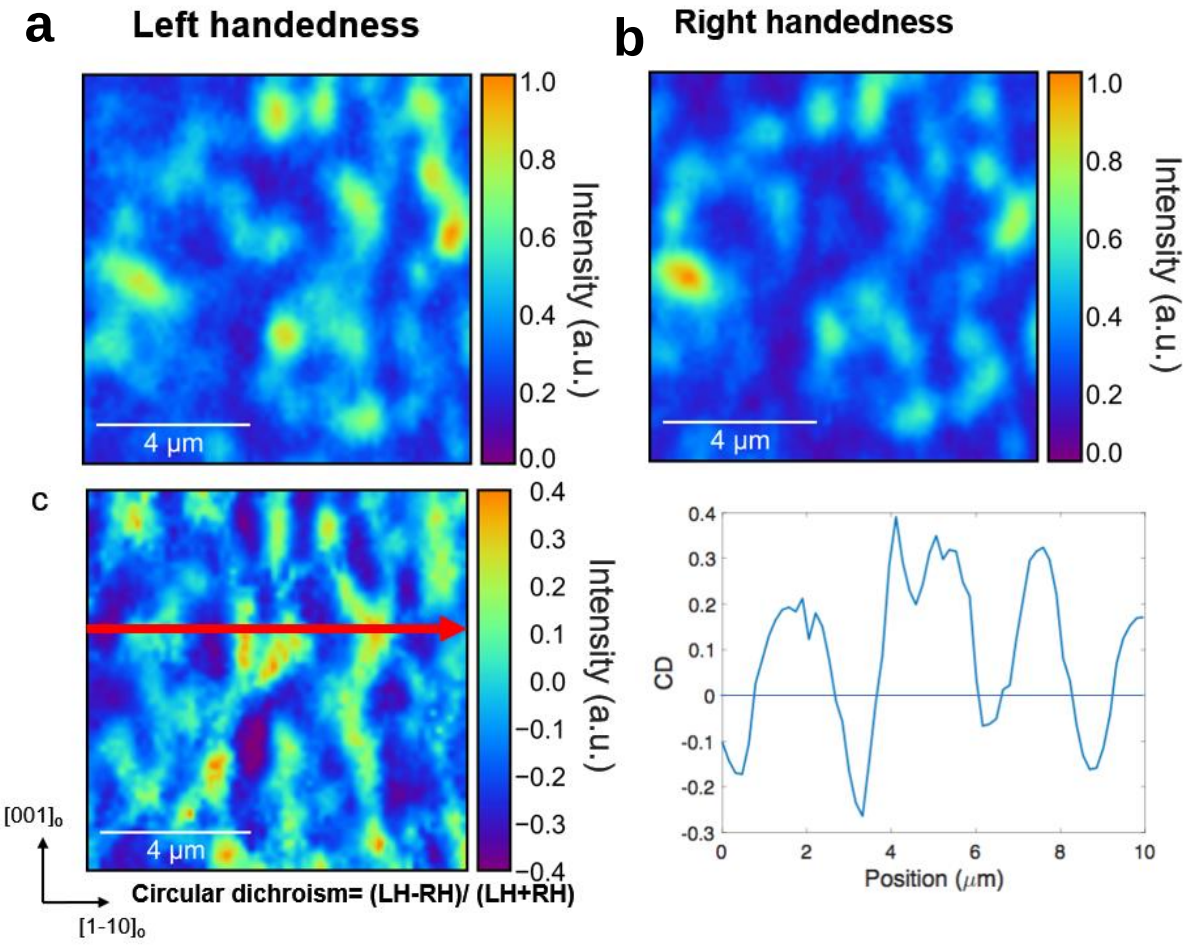

Figure 6.8 A circular dichroism from a second harmonic generation on trilayer heterostructure (n = 20). (a, b) Normalized SHG intensity image with left-handed (LH) and right-handed (RH) polarized excitation, respectively. (c) Circular dichroism (CD) image derived from the intensities in (a, b) through the use of Equation 6-3. (d) Line-cut of the intensities from (c) along the red line showing periodic behavior.

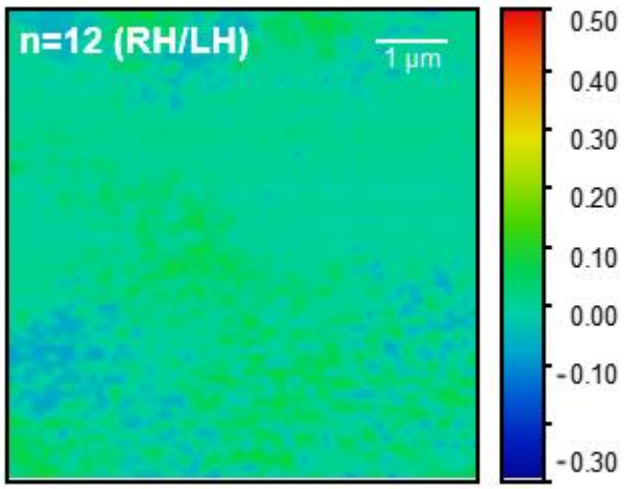

Figure 6.9 Circular dichroism from a second harmonic generation on trilayer heterostructure (n = 12), showing no CD signal due to the ferroelectric a_1-a_2 twin domains.

6.5 Summary

In conclusion, the atomic displacement mapping can be used to identify the different handedness of vortices, which can also be probed through the use of CD in SHG measurements. The single vortex state in $(PTO)_n/(STO)_n$ trilayer heterostructures demonstrates the non-trivial chiral topological structure with anti-phase boundary and shows that not only do the vortices have a toroidal phase with structural 3D chirality but also there is a diversity of left-handedness, right-handedness, and achiral regions for potential electric-field control of chiral polarization states. Furthermore, the polar vectors at the middle of the boundary in the achiral structure could have out-of-plane projection along the $\pm [110]_o$, and this type of polarization distribution could be the precursor of skyrmion-like textures. Novel topologies with chirality such as ferroelectric vortices and ferroelectric skyrmion-type textures [169] for further external functionalities could be the next candidates for smaller memory unit applications and could pave the way for opportunities for the control of chirality in ferroelectric topology information processing.

Chapter 7
Conclusions and future directions

The recent discovery of novel chiral polar vortices in $(PTO)_n/(STO)_n$ superlattice heterostructures has shown that the vortex state not only coexists with ferroelectric polarized twin *a*-domains with a response under an electric field but also possesses emergent chirality. Beyond these observations, there are still mysteries remaining. In this research, topics including the identification of vortex state in a confined PTO layer, the vortex evolution from ferroelectric *a*-domains, the search for antiparallel axial polarizations, and the chirality of the vortex state were investigated to solve the mysteries of polar vortices from previous studies on $(PTO)_n/(STO)_n$ superlattice heterostructures. The important questions included: how the vortex phase emerges from the ferroelectric phase, what the crucial factor is in the formation of the toroidal phase, if there are antiparallel axial polarizations resulting in 3D chirality, and if any differences of chirality occur in polar vortices. These questions were realized through the use of the $(PTO)_n/(STO)_n$ trilayer with advanced combinations of characterizations and simulations. Understanding the mechanical and electrical boundary conditions and the mechanism of the phase transition are crucial to this work and have been described in Chapter 1.

The first result is the emergence of the long-range ordering of vortices in the $(PTO)_n/(STO)_n$ trilayer. This provides a simple model system to study further questions because it is easier to characterize the vortex state in both cross-sectional and planar-view TEM in a single confined PTO layer. This vortex state in trilayers can be found stabilized through the contributions of Landau, elastic, electrostatic, and gradient energies, and it forms a stripe structure with a spacing of ~10 nm—this is extremely important for further study of the in-plane polarization distribution. The second result is the direct observation of vortex evolution from ferroelectric *a*-domains as a function of periodicity through the use of planar-view TEM, RSM, PFM, and phase-field modeling. This evidence indicates that the origin of vortex formation is the instability of head-to-head domains between ferroelectric phases at the beginning of the phase evolution and that the elastic energy from the long-range interactions is a crucial factor in the PTO/STO system for exciting the vortex state. In addition, the single phase of polar vortices could possess antiparallel polarizations along the vortex direction.

The third result of this research is the antiparallel axial polarization of polar vortices found in the $(PTO)_n/(STO)_n$ trilayer so as to prove 3D chirality using zone axis TEM techniques. The anti-phase boundary has the function of changing the polarization distribution along the vortex direction, which is related to the chirality. The fourth result of this research is the different handedness regions found, including left-handed, right-handed, and achiral regions composed of a vortex state in $(PTO)_n/(STO)_n$ trilayer heterostructures—and the central area of the achiral region could be the precursor to skyrmions-like textures. These results have answered the proposed questions and have provided further understandings for designing novel topologies in ferroelectrics with the potential for device applications.

For future directions, since previous studies and this work have shown that it is possible to stabilize novel topologies with peculiar properties, there are several interesting issues to pursue that would benefit both the scientific and application perspectives.

First, it is important to pursue the emergence of novel ferroelectric topologies. For example, ferroelectric skyrmion-like topologies with their chirality are one of the critical topological structures to study since they are the analogy to magnetic skyrmions and are promising for memory devices. Tuning the energy balance to stabilize the novel topologies is the critical task. This balance could be modified through using the mechanical and electrical boundary conditions in the $(PTO)_n/(STO)_n$ system or by changing the different ferroelectric or paraelectric layers. For example, changing the paraelectric layer can tune the elastic stiffness and dielectric constant, which could, in turn, tip the balance of the energy to form a novel state. While tensile strain can be introduced to stabilize the vortex state in this work, compressive strain would stabilize more *c*-domains in ferroelectrics and could possibly stabilize a skyrmion-like topology, for which the vector field is mostly toward an out-of-plane direction. It is also possible for other topological structures to emerge in ferroelectric materials, and it is essential to study their phase formation, phase transitions, and properties.

Second, for the investigation of the dynamic behaviors of ferroelectric topologies in response to external stimuli such as electric field, temperature, and stress, it is crucial to understand the underlying mechanisms and their properties. Through the use of in-situ TEM, the direct observation of the dynamic process of the phase transition of the vortex state and ferroelectric *a*-domains under applied electric field can provide information about how the vortex structure can be moved or switched. Most importantly, direct observation of the control of chirality in the full vortex state is crucial for multi-state memory applications. It is essential to probe the dynamic moving and the switching behaviors of not only the vortex state but also the novel skyrmion-like state since this should prove to be essential in advancing their potential for information technology. These are some future directions, whose exploration should undoubtedly lead to even more new directions of research for ferroelectric topological systems with their phase transition and novel properties. The realization of control over these novel topological states would benefit both our fundamental understanding as well as future device applications.

Bibliography:

[1] J. Seidel, R. K. Vasudevan, and N. Valanoor, Adv. Electron. Mater. **2**, 1500292 (2016).

[2] I. Kezsmarki, S. Bordacs, P. Milde, E. Neuber, L. M. Eng, J. S. White, H. M. Rønnow, C. D. Dewhurst, M. Mochizuki, K. Yanai, H. Nakamura, D. Ehlers, V. Tsurkan, and A. Loidl, Nat. Mater. **14**, 1116 (2015).

[3] J. Seidel, L. W. Martin, Q. He, Q. Zhan, Y. H. Chu, A. Rother, M. E. Hawkridge, P. Maksymovych, P. Yu, M. Gajek, N. Balke, S. V. Kalinin, S. Gemming, F. Wang, G. Catalan, J. F. Scott, N. A. Spaldin, J. Orenstein, and R. Ramesh, Nat. Mater. **8**, 229 (2009).

[4] P. R. Potnis, N. T. Tsou, and J. E. Huber, Materials, **4**, 417 (2010).

[5] J. J. Celine Lichtensteiger, Pavlo Zubko, Massimiliano Stengel, Pablo Aguado-Puente, Jean-Marc Triscone, Philippe Ghosez, in *Oxide Thin Film.* (2012), p. 281.

[6] D. G. Schlom, L.-Q. Chen, C.-B. Eom, K. M. Rabe, S. K. Streiffer, and J.-M. Triscone, Annu. Rev. Mater. Res. **37**, 589 (2007).

[7] I. I. Naumov, L. Bellaiche, and H. Fu, Nature **432**, 737 (2004).

[8] P. Zubko, N. Jecklin, A. Torres-Pardo, P. Aguado-Puente, A. Gloter, C. Lichtensteiger, J. Junquera, O. Stéphan, and J. M. Triscone, Nano Lett. **12**, 2846 (2012).

[9] E. Bousquet, M. Dawber, N. Stucki, C. Lichtensteiger, P. Hermet, S. Gariglio, J. M. Triscone, and P. Ghosez, Nature **452**, 732 (2008).

[10] Y. L. Tang, Y. L. Zhu, E. A. Eliseev, W. Y. Wang, Y. J. Wang, Y. B. Xu, Z. D. Zhang, and S. J. Pennycook, Science, 1259869 (2015).

[11] A. K. Yadav, C. T. Nelson, S. L. Hsu, Z. Hong, J. D. Clarkson, C. M. Schlepuëtz, A. R. Damodaran, P. Shafer, E. Arenholz, L. R. Dedon, D. Chen, A. Vishwanath, A. M. Minor, L. Q. Chen, J. F. Scott, L. W. Martin, and R. Ramesh, Nature **530**, 198 (2016).

[12] A. R. Damodaran, J. D. Clarkson, Z. Hong, H. Liu, A. K. Yadav, C. T. Nelson, S. L. Hsu, M. R. McCarter, K. D. Park, V. Kravtsov, A. Farhan, Y. Dong, Z. Cai, H. Zhou, P. Aguado-Puente, P. Garcia-Fernandez, J. Iniguez, J. Junquera, A. Scholl, M. B. Raschke, L. Q. Chen, D. D. Fong, R. Ramesh, and L. W. Martin, Nat. Mater. **16**, 1003 (2017).

[13] P. Shafer, P. García-Fernández, P. Aguado-Puente, A. R. Damodaran, A. K. Yadav, C. T. Nelson, S.-L. Hsu, J. C. Wojdeł, J. Íñiguez, L. W. Martin, E. Arenholz, J. Junquera, and R. Ramesh, Proc. Natl. Acad. Sci. **115**, 915 (2018).

[14] L. W. Martin, Y. H. Chu, and R. Ramesh, Mater. Sci. Eng. R Reports **68**, 89 (2010).

[15] C. Buzea and K. Robbie, Reports Prog. Phys. **68**, 385 (2005).

[16] S. HASEGAWA, in *Charact. Mater.* (2012), pp. 1925–1938.

[17] B. Fultz and J. Howe, in *Transm. Electron Microsc. Diffractometry Mater.* (2013), p. 70.

[18] W. Carter, in *Transm. Electron Microsc. a Textb. Mater. Sci.* (1996), p. 384.

[19] D. A. Muller, Nat. Mater. **8**, 263 (2009).

[20] P. Zubko, N. Stucki, C. Lichtensteiger, and J. M. Triscone, Phys. Rev. Lett. **104**, 187601 (2010).

[21] R. Proksch and S. Kalinin, *Piezoresponse Force Microscopy with Asylum Research AFMs* (2010).

[22] G. De Luca, M. D. Rossell, J. Schaab, N. Viart, M. Fiebig, and M. Trassin, Adv. Mater. **29**, 1605145 (2017).

[23] P. Pantazis, J. Maloney, D. Wu, and S. E. Fraser, Proc. Natl. Acad. Sci. **107**, 14535

(2010).
[24] L. Q. Chen, J. Am. Ceram. Soc. **91**, 1835 (2008).
[25] F. Xue, J. J. Wang, G. Sheng, E. Huang, Y. Cao, H. H. Huang, P. Munroe, R. Mahjoub, Y. L. Li, V. Nagarajan, and L. Q. Chen, Acta Mater. **61**, 2909 (2013).
[26] T. Kimura, Y. Otani, and J. Hamrle, Appl. Phys. Lett. **87**, 172506 (2005).
[27] X. Z. Yu, Y. Onose, N. Kanazawa, J. H. Park, J. H. Han, Y. Matsui, N. Nagaosa, and Y. Tokura, Nature **465**, 901 (2010).
[28] V. Uhlíř, M. Urbánek, L. Hladík, J. Spousta, M. Y. Im, P. Fischer, N. Eibagi, J. J. Kan, E. E. Fullerton, and T. Šikola, Nat. Nanotechnol. **8**, 341 (2013).
[29] P. Zubko, S. Gariglio, M. Gabay, P. Ghosez, and J.-M. Triscone, Annu. Rev. Condens. Matter Phys. **2**, 141 (2011).
[30] Y. Tokura and N. Nagaosa, Science, **288**, 462 (2000).
[31] M. Imada, A. Fujimori, and Y. Tokura, Rev. Mod. Phys. **70**, 1039 (1998).
[32] L. W. Martin and R. Ramesh, Acta Mater. **60**, 2449 (2012).
[33] J. Wang, J. B. Neaton, H. Zheng, V. Nagarajan, S. B. Ogale, B. Liu, D. Viehland, V. Vaithyanathan, D. G. Schlom, U. V Waghmare, N. A. Spaldin, K. M. Rabe, M. Wuttig, and R. Ramesh, Science, **299**, 1719 (2003).
[34] M. Dawber, K. M. Rabe, and J. F. Scott, Rev. Mod. Phys. **77**, 1083 (2005).
[35] S.-W. CHEONG and A. M. MOSTOVOY, **6**, 13 (2007).
[36] R. Ramesh and N. Spaldin, Mater. Sci. **6**, 21 (2007).
[37] E. Dagotto, J. Burgy, and A. Moreo, Solid State Commun. **126**, 9 (2003).
[38] R. Mathieu, D. Akahoshi, A. Asamitsu, Y. Tomioka, and Y. Tokura, Phys. Rev. Lett. **93**, 227202 (2004).
[39] E. Dagotto and M. A. R. Tech, **66**, 763 (1994).
[40] N. D. Mermin, Rev. Mod. Phys. **51**, 591 (1979).
[41] T. Skyrme, Nucl. Phys. **31**, 556 (1962).
[42] Y. S. Lin, P. J. Grundy, and E. A. Giess, Appl. Phys. Lett. **23**, 485 (1973).
[43] A. Fert, V. Cros, and J. Sampaio, Nat. Nanotechnol. **8**, 152 (2013).
[44] C. Kittel, Phys. Rev. **70**, 965 (1946).
[45] C. Kittel, Phys. Rev. **21**, 745 (1959).
[46] P. O. Jubert, J. C. Toussaint, O. Fruchart, C. Meyer, and Y. Samson, Europhys. Lett. **63**, 132 (2003).
[47] R. Hertel, O. Fruchart, S. Cherifi, P. O. Jubert, S. Heun, A. Locatelli, and J. Kirschner, Phys. Rev. B **72**, 214409 (2005).
[48] R. D. Gomez, T. V. Luu, A. O. Pak, K. J. Kirk, and J. N. Chapman, J. Appl. Phys. **85**, 6163 (1999).
[49] R. Pulwey, M. Zölfl, G. Bayreuther, and D. Weiss, J. Appl. Phys. **91**, 7995 (2002).
[50] J. M. Gregg, Ferroelectrics **433**, 74 (2012).
[51] N. D. Mermin, Rev. Mod. Phys. **51**, 591 (1979).
[52] P. Fischer, M. Y. Im, S. Kasai, K. Yamada, T. Ono, and A. Thiaville, Phys. Rev. B **83**, 212402 (2011).
[53] J. Li and C. Rau, Phys. Rev. Lett. **97**, 107201 (2006).
[54] T. Okuno, K. Mibu, and T. Shinjo, J. Appl. Phys. **95**, 3612 (2004).
[55] J. Shibata, Y. Nakatani, G. Tatara, H. Kohno, and Y. Otani, J. Magn. Magn. Mater. **310**, 2041 (2007).
[56] B. B. Peeler, W. H. Martin, M. P. Sandler, and R. E. Goldstein, Am. Surg. **63**, 37 (1997).

[57] T. Kimura, Y. Otani, H. Masaki, T. Ishida, R. Antos, and J. Shibata, Appl. Phys. Lett. **90**, 132501 (2007).
[58] E. Pinilla-Cienfuegos, S. Mañas-Valero, A. Forment-Aliaga, and E. Coronado, ACS Nano **10**, 1764 (2016).
[59] B. Van Waeyenberge, A. Puzic, H. Stoll, K. W. Chou, T. Tyliszczak, R. Hertel, M. Fähnle, H. Brückl, K. Rott, G. Reiss, I. Neudecker, D. Weiss, C. H. Back, and G. Schütz, Nature **444**, 461 (2006).
[60] K. Yamada, S. Kasai, Y. Nakatani, K. Kobayashi, H. Kohno, A. Thiaville, and T. Ono, Nat. Mater. **6**, 270 (2007).
[61] R. Hertel, S. Gliga, M. Fähnle, and C. M. Schneider, Phys. Rev. Lett. **98**, 117201 (2007).
[62] Y. Liu, S. Gliga, R. Hertel, and C. M. Schneider, Appl. Phys. Lett. **91**, 112501 (2007).
[63] S. Mühlbauer, B. Binz, F. Jonietz, and C. Pfleiderer, Science, **323**, 915 (2010).
[64] N. Nagaosa and Y. Tokura, Nat. Nanotechnol. **8**, 899 (2013).
[65] S. Rohart and A. Thiaville, Phys. Rev. B **88**, 184422 (2013).
[66] I. A. Sergienko and E. Dagotto, Phys. Rev. B **73**, 094434 (2006).
[67] X. Zhang, Y. Zhou, M. Ezawa, G. P. Zhao, and W. Zhao, Sci. Rep. **5**, 11369 (2015).
[68] J. Seidel, G. Singh-Bhalla, Q. He, S. Y. Yang, Y. H. Chu, and R. Ramesh, Phase Transitions **86**, 53 (2013).
[69] S. Farokhipoor and B. Noheda, Phys. Rev. Lett. **107**, 3 (2011).
[70] C. H. Yang, J. Seidel, S. Y. Kim, P. B. Rossen, P. Yu, M. Gajek, Y. H. Chu, L. W. Martin, M. B. Holcomb, Q. He, P. Maksymovych, N. Balke, S. V. Kalinin, A. P. Baddorf, S. R. Basu, M. L. Scullin, and R. Ramesh, Nat. Mater. **8**, 485 (2009).
[71] J. B. Goodenough, J. Phys. Chem. Solids **25**, 151 (1964).
[72] R. E. Cohen, Ferroelectrics **150**, 1 (1993).
[73] R. Schmidt, E. Langenberg, J. Ventura, and M. Varela, in *Perovskite Crystallogr. Chem. Catal. Performance-Bi Contain. Multiferroic Perovskite Oxide Thin Film.* (2014), p. Chapter 2, 4.
[74] J. H. Haeni, P. Irvin, W. Chang, R. Uecker, P. Reiche, and Y. L. Li, Nature **430**, 758 (2004).
[75] K. J. Choi, M. Biegalski, Y. L. Li, A. Sharan, J. Schubert, R. Uecker, P. Reiche, Y. B. Chen, X. Q. Pan, V. Gopalan, L.-Q. Chen, D. G. Schlom, and C. B. Eo, Science, **12**, 1005 (2004).
[76] W. J. Chen, Y. Zheng, and B. Wang, Appl. Phys. Lett. **100**, 062901 (2012).
[77] S. Prosandeev and L. Bellaiche, Phys. Rev. B **75**, 094102 (2007).
[78] P. Aguado-Puente and J. Junquera, Phys. Rev. B **85**, 184105 (2012).
[79] W. J. Chen, Y. Zheng, B. Wang, and J. Y. Liu, J. Appl. Phys. **115**, 214106 (2014).
[80] S. Prosandeev, I. Ponomareva, I. Kornev, I. Naumov, and L. Bellaiche, Phys. Rev. Lett. **96**, 237601 (2006).
[81] Y. Nahas, S. Prokhorenko, L. Louis, Z. Gui, I. Kornev, and L. Bellaiche, Nat. Commun. **6**, 8542 (2015).
[82] J. C. Jiang, X. Q. Pan, W. Tian, C. D. Theis, and D. G. Schlom, Appl. Phys. Lett. **74**, 2851 (1999).
[83] C. T. Nelson, B. Winchester, Y. Zhang, S. J. Kim, A. Melville, C. Adamo, C. M. Folkman, S. H. Baek, C. B. Eom, D. G. Schlom, L. Q. Chen, and X. Pan, Nano Lett. **11**, 828 (2011).
[84] C. L. Jia, K. W. Urban, M. Alexe, D. Hesse, and I. Vrejoiu, Science, **331**, 1420 (2011).

[85] M. Dawber, N. Stucki, C. Lichtensteiger, S. Ganglio, P. Ghosez, and J. M. Triscone, Adv. Mater. **19**, 4153 (2007).
[86] M. Dawber, C. Lichtensteiger, M. Cantoni, M. Veithen, P. Ghosez, K. Johnston, K. M. Rabe, and J. M. Triscone, Phys. Rev. Lett. **95**, 177601 (2005).
[87] R. G. P. McQuaid, A. Gruverman, J. F. Scott, and J. M. Gregg, Nano Lett. **14**, 4230 (2014).
[88] S. Matzen, O. Nesterov, G. Rispens, J. A. Heuver, M. Biegalski, H. M. Christen, and B. Noheda, Nat. Commun. **5**, 95 (2014).
[89] L. Feigl, L. J. McGilly, and N. Setter, Ferroelectrics **465**, 36 (2014).
[90] J. Iwasaki, M. Mochizuki, and N. Nagaosa, Nat. Commun. **4**, 1463 (2013).
[91] U. K. Rößler, A. N. Bogdanov, and C. Pfleiderer, Nature **442**, 797 (2006).
[92] O. Boulle, J. Vogel, H. Yang, S. Pizzini, D. De Souza Chaves, A. Locatelli, T. O. Menteş, A. Sala, L. D. Buda-Prejbeanu, O. Klein, M. Belmeguenai, Y. Roussigné, A. Stashkevich, S. Mourad Chérif, L. Aballe, M. Foerster, M. Chshiev, S. Auffret, I. M. Miron, and G. Gaudin, Nat. Nanotechnol. **11**, 449 (2016).
[93] V. Dvořák, Phys. Status Solidi **46**, 763 (1971).
[94] Toru Moriya, Phys. Rev. Lett. **4**, 228 (1960).
[95] P. Taylor, M. Street, and L. Wt, Environ. Chem. **249**, (2010).
[96] D. H. A. Blank, G. Koster, G. A. J. H. M. Rijnders, Eelco Van Setten, P. Slycke, and H. Rogalla, J. Cryst. Growth **211**, 98 (2000).
[97] R. D. Vispute, J. Narayan, H. Wu, and K. Jagannadham, J. Appl. Phys. **77**, 4724 (1995).
[98] A. Ohtomo, M. Kawasaki, T. Koida, K. Masubuchi, H. Koinuma, Y. Sakurai, Y. Yoshida, T. Yasuda, and Y. Segawa, Appl. Phys. Lett. **72**, 2466 (1998).
[99] D. Dijkkamp, T. Venkatesan, X. D. Wu, S. A. Shaheen, N. Jisrawi, Y. H. Min-Lee, W. L. McLean, and M. Croft, Appl. Phys. Lett. **51**, 619 (1987).
[100] T. Venkatesan, X. D. Wu, A. Inam, and J. B. Wachtman, Appl. Phys. Lett. **52**, 1193 (1988).
[101] Y. Kuroiwa, S. Aoyagi, A. Sawada, J. Harada, E. Nishibori, M. Takata, and M. Sakata, Phys. Rev. Lett. **87**, 217601 (2001).
[102] C. W. Jones, P. D. Battle, P. Lightfoot, and W. T. A. Harrison, Acta Crystallogr. Sect. C Cryst. Struct. Commun. **45**, 365 (1989).
[103] Z. H. Chen, A. R. Damodaran, R. Xu, S. Lee, and L. W. Martin, Appl. Phys. Lett. **104**, 182908 (2014).
[104] C. Kisielowski, B. Freitag, M. Bischoff, H. Van Lin, S. Lazar, G. Knippels, P. Tiemeijer, M. Van Der Stam, S. Von Harrach, M. Stekelenburg, M. Haider, S. Uhlemann, H. Müller, P. Hartel, B. Kabius, D. Miller, I. Petrov, E. A. Olson, T. Donchev, E. A. Kenik, A. R. Lupini, J. Bentley, S. J. Pennycook, I. M. Anderson, A. M. Minor, A. K. Schmid, T. Duden, V. Radmilovic, Q. M. Ramasse, M. Watanabe, R. Erni, E. A. Stach, P. Denes, and U. Dahmen, Microsc. Microanal. **14**, 469 (2008).
[105] C. Ophus, J. Ciston, and C. T. Nelson, Ultramicroscopy **162**, 1 (2016).
[106] A. M. Glazer and S. A. Mabud, Acta Crystallogr. Sect. B Struct. Crystallogr. Cryst. Chem. **34**, 1065 (1978).
[107] A. Gruverman, J. Vac. Sci. Technol. B Microelectron. Nanom. Struct. **13**, 1095 (1995).
[108] G. De Luca, N. Strkalj, S. Manz, C. Bouillet, M. Fiebig, and M. Trassin, Nat. Commun. **8**, 1419 (2017).
[109] S. A. Denev, T. T. A. Lummen, E. Barnes, A. Kumar, and V. Gopalan, J. Am. Ceram.

Soc. **94**, 2699 (2011).
[110] K. Konishi, T. Higuchi, J. Li, J. Larsson, S. Ishii, and M. Kuwata-Gonokami, Phys. Rev. Lett. **112**, 135502 (2014).
[111] K. L. Seyler, J. R. Schaibley, P. Gong, P. Rivera, A. M. Jones, S. Wu, J. Yan, D. G. Mandrus, W. Yao, and X. Xu, Nat. Nanotechnol. **10**, 407 (2015).
[112] Y. L. Li, S. Y. Hu, Z. K. Liu, and L. Q. Chen, Acta Mater. **50**, 395 (2002).
[113] P. Wu, X. Ma, Y. Li, V. Gopalan, and L. Q. Chen, Appl. Phys. Lett. **100**, 092905 (2012).
[114] Z. Hong, J. Britson, J. M. Hu, and L. Q. Chen, Acta Mater. **73**, 75 (2014).
[115] L. Hong, P. Wu, Y. Li, V. Gopalan, C. B. Eom, D. G. Schlom, and L. Q. Chen, Phys. Rev. B **90**, 174111 (2014).
[116] Y. L. Li, S. Y. Hu, Z. K. Liu, and L. Q. Chen, Appl. Phys. Lett. **81**, 427 (2002).
[117] J. J. Wang, X. Q. Ma, Q. Li, J. Britson, and L. Q. Chen, Acta Mater. **61**, 7591 (2013).
[118] R. Uecker, B. Velickov, D. Klimm, R. Bertram, M. Bernhagen, M. Rabe, M. Albrecht, R. Fornari, and D. G. Schlom, J. Cryst. Growth **310**, 2649 (2008).
[119] L. Q. Chen and J. Shen, Comput. Phys. Commun. **108**, 147 (1998).
[120] M. J. Haun, E. Furman, S. J. Jang, H. A. McKinstry, and L. E. Cross, J. Appl. Phys. **62**, 3331 (1987).
[121] G. Sheng, Y. L. Li, J. X. Zhang, S. Choudhury, Q. X. Jia, V. Gopalan, D. G. Schlom, Z. K. Liu, and L. Q. Chen, Appl. Phys. Lett. **96**, 10 (2010).
[122] G. Catalan, J. Seidel, R. Ramesh, and J. F. Scott, Rev. Mod. Phys. **84**, 119 (2012).
[123] A. Soumyanarayanan, N. Reyren, A. Fert, and C. Panagopoulos, Nature **539**, 509 (2016).
[124] J. Mannhart and D. G. Schlom, Science, **327**, 1607 (2010).
[125] M. Y. Im, P. Fischer, K. Yamada, T. Sato, S. Kasai, Y. Nakatani, and T. Ono, Nat. Commun. **3**, 983 (2012).
[126] A. Ruotolo, V. Cros, B. Georges, A. Dussaux, J. Grollier, C. Deranlot, R. Guillemet, K. Bouzehouane, S. Fusil, and A. Fert, Nat. Nanotechnol. **4**, 528 (2009).
[127] R. Wiesendanger, Nat. Rev. Mater. **1**, 16044 (2016).
[128] H. Béa and P. Paruch, Nat. Mater. **8**, 168 (2009).
[129] P. Schoenherr, J. Müller, L. Köhler, A. Rosch, N. Kanazawa, Y. Tokura, M. Garst, and D. Meier, Nat. Phys. **14**, 465 (2018).
[130] S. Emori, U. Bauer, S. M. Ahn, E. Martinez, and G. S. D. Beach, Nat. Mater. **12**, 611 (2013).
[131] A. Wachowiak, J. Wiebe, M. Bode, and O. Pietzsch, Science, **298**, 577 (2002).
[132] T. Shinjo, T. Okuno, R. Hassdorf, K. Shigeto, and T. Ono, Science, **289**, 930 (2000).
[133] S. M. Yang, J. G. Yoon, and T. W. Noh, Curr. Appl. Phys. **11**, 1111 (2011).
[134] Z. Hong, A. R. Damodaran, F. Xue, S. L. Hsu, J. Britson, A. K. Yadav, C. T. Nelson, J. J. Wang, J. F. Scott, L. W. Martin, R. Ramesh, and L. Q. Chen, Nano Lett. **17**, 2246 (2017).
[135] L. Normand and A. Thorel, Phase Transitions **46**, 77 (1994).
[136] R. Gevers, H. Blank, and S. Amelinckx, Phys. Status Solidi **13**, 449 (1966).
[137] M. Janovská, P. Sedlák, H. Seiner, M. Landa, P. Marton, P. Ondrejkovič, and J. Hlinka, J. Phys. Condens. Matter **24**, 385404 (2012).
[138] S. Matzen, O. Nesterov, G. Rispens, J. A. Heuver, M. Biegalski, H. M. Christen, and B. Noheda, Nat. Commun. **5**, 4415 (2014).
[139] N. Balke, B. Winchester, W. Ren, Y. H. Chu, A. N. Morozovska, E. A. Eliseev, M. Huijben, R. K. Vasudevan, P. Maksymovych, J. Britson, S. Jesse, I. Kornev, R. Ramesh, L. Bellaiche, L. Q. Chen, and S. V. Kalinin, Nat. Phys. **8**, 81 (2012).

[140] A. Fernández-Pacheco, R. Streubel, O. Fruchart, R. Hertel, P. Fischer, and R. P. Cowburn, Nat. Commun. **8**, 15756 (2017).
[141] S. Da Col, S. Jamet, N. Rougemaille, A. Locatelli, T. O. Mentes, B. S. Burgos, R. Afid, M. Darques, L. Cagnon, J. C. Toussaint, and O. Fruchart, Phys. Rev. B **89**, 180405 (2014).
[142] P. Bak and M. H. Jensen, J. Phys. C Solid State Phys. **13**, 881 (1980).
[143] F. Zheng, H. Li, S. Wang, D. Song, C. Jin, W. Wei, A. Kovács, J. Zang, M. Tian, Y. Zhang, H. Du, and R. E. Dunin-Borkowski, Phys. Rev. Lett. **119**, 197205 (2017).
[144] S.-L. Hsu, M. R. McCarter, C. Dai, Z. Hong, L.-Q. Chen, C. T. Nelson, L. W. Martin, and R. Ramesh, *Vortex State in Confined Ferroelectrics* (2018).
[145] G. Catalan, A. H. G. Viooswijk, A. Janssens, G. Rispens, S. Redfern, G. Rijnders, D. H. A. Blank, and B. Noheda, Integr. Ferroelectr. **92**, 18 (2007).
[146] N. Lemée, I. C. Infante, C. Hubault, A. Boulle, N. Blanc, N. Boudet, V. Demange, and M. G. Karkut, ACS Appl. Mater. Interfaces **7**, 19906 (2015).
[147] H. A. Dürr, E. Dudzik, S. S. Dhesi, J. B. Goedkoop, G. Van Der Laan, M. Belakhovsky, C. Mocuta, A. Marty, and Y. Samson, Science, **284**, 2166 (1999).
[148] M. Bode, M. Heide, K. Von Bergmann, P. Ferriani, S. Heinze, G. Bihlmayer, A. Kubetzka, O. Pietzsch, S. Blügel, and R. Wiesendanger, Nature **447**, 190 (2007).
[149] J. Yeom, U. S. Santos, M. Chekini, M. Cha, A. F. De Moura, and N. A. Kotov, Science, **359**, 309 (2018).
[150] X. Z. Yu, N. Kanazawa, Y. Onose, K. Kimoto, W. Z. Zhang, S. Ishiwata, Y. Matsui, and Y. Tokura, Nat. Mater. **10**, 106 (2011).
[151] S.Seki, X. Z. Yu, S. Ishiwata, and Y. Tokura, Science, **336**, 198 (2012).
[152] Y. Tokunaga, X. Z. Yu, and Y. Tokura, Nat. Commun. **6**, 7638 (2015).
[153] R. Streubel, C. H. Lambert, N. Kent, P. Ercius, A. T. N'Diaye, C. Ophus, S. Salahuddin, and P. Fischer, Adv. Mater. **30**, 1800199 (2018).
[154] G. Chen, A. T. N'Diaye, S. P. Kang, H. Y. Kwon, C. Won, Y. Wu, Z. Q. Qiu, and A. K. Schmid, Nat. Commun. **6**, 6598 (2015).
[155] G. Chen, T. Ma, A. T. N'Diaye, H. Kwon, C. Won, Y. Wu, and A. K. Schmid, Nat. Commun. **4**, 2671 (2013).
[156] G. Chen and A. K. Schmid, Adv. Mater. **27**, 5738 (2015).
[157] V. Stepkova, P. Marton, and J. Hlinka, J. Phys. Condens. Matter **24**, 21 (2012).
[158] S. Cherifi-Hertel, H. Bulou, R. Hertel, G. Taupier, K. D. H. Dorkenoo, C. Andreas, J. Guyonnet, I. Gaponenko, K. Gallo, and P. Paruch, Nat. Commun. **8**, 15768 (2017).
[159] Y.-J. Wang, Y.-L. Zhu, and X.-L. Ma, J. Appl. Phys. **122**, 134104 (2017).
[160] M. Jaafar, R. Yanes, D. Perez De Lara, O. Chubykalo-Fesenko, A. Asenjo, E. M. Gonzalez, J. V. Anguita, M. Vazquez, and J. L. Vicent, Phys. Rev. B **81**, 054439 (2010).
[161] L. Van Lich, T. Shimada, J. Wang, V. H. Dinh, T. Q. Bui, and T. Kitamura, Phys. Rev. B **96**, 134119 (2017).
[162] S. Zhang, J. Zhou, Y. S. Park, J. Rho, R. Singh, S. Nam, A. K. Azad, H. T. Chen, X. Yin, A. J. Taylor, and X. Zhang, Nat. Commun. **3**, 942 (2012).
[163] R. P. Beardsley, S. Bowe, D. E. Parkes, C. Reardon, K. W. Edmonds, B. L. Gallagher, S. A. Cavill, and A. W. Rushforth, Sci. Rep. **7**, 7613 (2017).
[164] C. Heo, N. S. Kiselev, A. K. Nandy, S. Blugel, and T. Rasing, Sci. Rep. **6**, 27146 (2016).
[165] S. Das, Y. L. Tang, Z. Hong, M. A. P. Gonçalves, and M. R. Mccarter, *Observation of Room-Temperature Polar Skyrmions* (2018).
[166] K. R. Campbell and P. J. Campagnola, J. Phys. Chem. B **121**, 1749 (2017).

[167] J. Lin, J. P. B. Mueller, Q. Wang, G. Yuan, N. Antoniou, X.-C. Yuan, and F. Capasso, Science, **340**, 331 (2013).
[168] G. Li, S. Chen, N. Pholchai, B. Reineke, P. W. H. Wong, E. Y. B. Pun, K. W. Cheah, T. Zentgraf, and S. Zhang, Nat. Mater. **14**, 607 (2015).
[169] M. A. P. Gonçalves, C. Escorihuela-Sayalero, P. García-Fernández, J. Junquera, and J. Íñiguez, ArXiv:1806.01617 (2018).